UCSF
UC San Francisco Electronic Theses and Dissertations

Title
Biomimetic, Polymer-Based Microcantilever Infrared Sensors

Permalink
https://escholarship.org/uc/item/8889m6qc

Author
Mueller, Michael T

Publication Date
2007-12-20

Peer reviewed|Thesis/dissertation

eScholarship.org Powered by the California Digital Library
University of California

Biomimetic, Polymer-Based Microcantilever Infrared Sensors

by

Michael Thomas Mueller

DISSERTATION

Submitted in partial satisfaction of the requirements for the degree of

DOCTOR OF PHILOSOPHY

in

Bioengineering

in the

GRADUATE DIVISION

of the

UNIVERSITY OF CALIFORNIA, SAN FRANCISCO

AND

UNIVERSITY OF CALIFORNIA, BERKELEY

UMI Number: 3289319

Copyright 2007 by
Mueller, Michael Thomas

All rights reserved.

UMI

UMI Microform 3289319
Copyright 2008 by ProQuest Information and Learning Company.
All rights reserved. This microform edition is protected against
unauthorized copying under Title 17, United States Code.

ProQuest Information and Learning Company
300 North Zeeb Road
P.O. Box 1346
Ann Arbor, MI 48106-1346

Biomimetic, Polymer-Based Microcantilever Infrared Sensors

Copyright © 2007

by

Michael Thomas Mueller

Dedication

To my wife, Jenny.

Acknowledgments

I am indebted to numerous people who contributed to the success of this work. I would like to thank the members of my dissertation committee, my advisor Prof. Albert Pisano, Prof. Dorian Liepmann, and Prof. Ming Wu at UC Berkeley, and Prof. Christoph Schreiner and Prof. Julie Schnapf at UC San Francisco.

This research project has benefited enormously from sustained industry involvement. In particular, I would like to thank Emel Bulat of Textron Systems, Dr. Kelvin Fu of HR Textron, and Dr. Dennis Pease, Charles Ryno, and Frank Swanson of IST for taking a risk on this project and supporting me along the way. They provided research funding, access to test equipment, technical expertise, and a reminder of the realities of the infrared market. Without their input this project would not be a success. I would also like to thank Dr. William Wiesmann of the BioSTAR Group and Dr. Shenda Baker of BioSTAR West for providing me with samples of ultrapure chitosan.

I would also like to acknowledge those agencies which provided research funding throughout my graduate school career, including DARPA / Defense Sciences Office, the National Institute of General Medical Sciences, and the State of California through the UC Discovery Grant program.

Dr. Michael Martin of Lawrence Berkeley National Laboratory provided access to and training on the FTIR equipment used in this work. Dr. Álvaro San Paulo

provided access to an atomic force microscope and conducted surface roughness measurements using it. Prof. Knut Aasmundtveit of the University of Vestfold, Norway helped me understand the thermomechanical properties of chitosan and chitin and introduced me to x-ray diffraction. Prof. Helmut Schmitz at the University of Bonn, Germany provided helpful discussions on the sensory structures of *Melanophila acuminata*. Dr. Anand Jog developed the capacitive readout test board. Dr. David Walther, Dr. Robert Azevedo, Dr. Debbie Jones, David Myers, and Dr. Matthew Hopcroft provided me with many helpful discussions along the way. For all the days that my experiments didn't go according to plan, my parents and my wife were a tremendous source of encouragement and support.

Abstract

Biomimetic, Polymer-Based Microcantilever Infrared Sensors

Michael Thomas Mueller

This dissertation describes the initial development of a polymer-based, microcantilever infrared sensor. The development of the sensor is bio-inspired and based upon the long-range infrared sensor found in the pyrophilous jewel beetle *Melanophila acuminata*, which is able to seek out forest fires from more than 50 km away. Based on several proposed models of the infrared detector found in *Melanophila acuminata*, as well as published *in vivo* experiments, the feasibility of polymer-based infrared thermal sensors was explored and developed. Polymer materials were chosen due to their high absorptivity in the infrared range due to vibrational resonance modes characteristic of their organic bonds.

Polymeric materials investigated in the course of this work include the polysaccharide and biomaterial chitin, its deacetylated derivative, chitosan, and the workhorse polymer of the semiconductor industry, novolak-resin-based photoresist. Chitin and chitosan are particularly noteworthy polymers for exploration in infrared detection due to their natural absorbance of infrared radiation near the 3 μm and 10 μm bands, which are important for the detection of the temperatures of warm engines and human body temperature, respectively.

Because only limited work (primarily focused on electrodeposition) has been focused on the microscale patterning of chitosan, a photolithography process for chitosan and chitin was developed to allow the integration of the material into a variety of microelectromechanical systems processes. In addition to optical / infrared sensing, this process has a variety of potential applications in tissue engineering, protein engineering, and lab-on-a-chip devices. To demonstrate these areas of use, surface functionalization was demonstrated using bioconjugation to attach a protein to a patterned chitosan surface. Thin films of chitosan and chitin were characterized using laser profilometry to identify the effect of temperature on the film stress, and contact angle to determine the degree of hydrophobicity or hydrophilicity at the chitosan or chitin surface.

Chitin in the infrared sensor of *Melanophila acuminata* functions as a thermo-mechanical material that has a high coefficient of thermal expansion and strong optical absorption in the infrared due to its chemical composition and organic bonds (absorption which matches its forest fire target). Based on this infrared detection mechanism, the potential exists to develop a broad, novel class of polymer-based, biomimetic infrared sensors having high CTE and spectral absorption tuned to a target of interest.

Towards this objective, a photoresist-polysilicon cantilever bimorph prototype was designed, fabricated, and tested. Two types of this device were formed with

different readouts; one required an optical readout while the other used a capacitive readout. Devices were characterized using optical and thermal methods. Prototypes were found to suffer from the presence of residual stress which caused significant out-of-plane deflections upon release. Such strain gradients should be minimized (by modifying the thermal processing steps or by annealing) to maximize the capacitive output signal. The optically-interrogated cantilever was observed to bend due to both stimulation with heat and with infrared radiation. The presence of a human finger in the vicinity of the silicon die was sufficient to cause cantilever deflection that was readily observable using optical techniques. The interdigitated cantilever array using capacitive readout was found to be highly sensitive, with a dynamic range $> 500:1$, a peak spectral sensitivity from 600 nm to 1.2 μm, and a threshold sensitivity of 2 μW/cm^2.

Chair, Dissertation Committee

Contents

List of Tables **xiii**

List of Figures **xiv**

1 Introduction **1**

1.1 Overview 1
1.2 History of Infrared Detection 2
1.3 Governing Equations 3
1.3.1 Stefan-Boltzmann Law 4
1.3.2 Planck's Law 4
1.3.3 Wien's Displacement Law 5
1.3.4 Detectivity (D*) 5
1.3.5 Noise Equivalent Temperature Difference (NETD) 6
1.4 Active vs. Passive Infrared Detection 6
1.5 Thermal Detectors 7
1.6 Photon Detectors 9
1.7 Nature's Infrared Detectors 11
1.7.1 Crotaline and Boid snakes 12
1.7.2 *Melanophila acuminata* 13
1.7.3 *Merimna atrata* 18
1.7.4 Ecological Partitioning of Bandwidth 19
1.8 Polymers as Infrared Materials 20
1.8.1 Polymethyl methacrylate (PMMA) 20
1.8.2 Photoresist 21
1.8.3 Chitin/Chitosan 22

2 Chitin Microfabrication **26**
2.1 Background . . . 27
2.2 Properties of chitin . . . 29
2.3 Disadvantages of chitin . . . 30
2.4 Properties of chitosan . . . 30
2.5 Shelf Life . . . 31
2.6 NaOH Treatment . . . 31
2.7 Reacetylation . . . 32
2.8 Prior art . . . 32
2.8.1 Chitosan Electrodeposition . . . 33
2.8.2 Chitosan Spin-coating . . . 34
2.8.3 Chitosan Nanoimprinting . . . 36
2.9 Solution Preparation . . . 37
2.9.1 Relationship between viscosity and molecular weight . . . 38
2.10 Chitosan Photolithography . . . 38
2.10.1 Surface roughness . . . 43
2.11 Etching . . . 44
2.11.1 Wet Etching . . . 45
2.11.2 Dry Etching . . . 46
2.11.3 Resist Strip . . . 51
2.12 Chitin Photolithography . . . 53
2.13 Lift-off method for patterning chitosan . . . 56
2.14 Surface functionalization . . . 61
2.14.1 Fluorescent tagging and protein attachment . . . 62
2.14.2 Alternating microfabrication and nanoengineering steps in process . . . 63
2.15 Chitin Microfabrication Uses Beyond Infrared Detection . . . 63

3 Properties of Chitosan and Chitin and Thin Film Characterization **66**
3.1 Overview . . . 66
3.2 Glass transition temperature . . . 68
3.3 Degree of acetylation . . . 69
3.4 Stress-Temperature Profile . . . 71
3.5 Hysteresis . . . 74
3.6 Thermal Annealing of Chitosan Films . . . 76
3.7 Conversion of chitosan to chitin by heating . . . 78
3.8 Differences in stress-temperature profile . . . 78
3.9 Thermal effect on bonding and crystallinity . . . 84

3.10 Coefficient of thermal expansion . . . 85
3.11 Contact angle . . . 88
3.11.1 Chitosan contact angle . . . 89
3.11.2 Chitin contact angle . . . 90
3.12 Summary . . . 92

4 Infrared Sensitive Cantilever Bimorph Design 94
4.1 Background . . . 94
4.2 Basic Device Concept . . . 96
4.3 Design Considerations . . . 97
4.3.1 Choice of Materials . . . 98
4.3.2 Infrared Absorption . . . 99
4.3.3 Thermal mismatch . . . 102
4.3.4 Thermal losses . . . 102
4.3.5 Geometry . . . 103
4.4 Thermomechanical analytical solutions . . . 106
4.5 Finite Element Model - 2D . . . 108
4.6 Finite Element Model - 3D . . . 109
4.7 Validity of Models . . . 110
4.8 Optimal Design . . . 112
4.9 Responsivity . . . 114
4.10 Noise . . . 116
4.11 Resonant frequency . . . 117
4.12 Packaging . . . 119
4.13 Methods of Increasing Performance . . . 120
4.13.1 Metal reflectors . . . 120
4.13.2 Vacuum packaging . . . 120
4.14 Device Fabrication . . . 121
4.14.1 Optical Readout Prototype . . . 121
4.14.2 Capacitive Readout Prototype . . . 125
4.14.3 Wafer Dicing Process . . . 126
4.14.4 Residual Stress . . . 132

5 Testing and Evaluation 139
5.1 Overview . . . 139
5.2 Temperature testing . . . 140
5.3 White light interferometry . . . 146
5.4 Electronic Readout . . . 149
5.4.1 Irvine Sensors MS3110 . . . 150
5.4.2 Capacitive test board . . . 150

5.4.3 Capacitive test subboard 151
5.4.4 Capacitive testing setup 155
5.4.5 Capacitive test results 155
5.4.6 Noise 164
5.4.7 Time response 165
5.4.8 Capacitive threshold effect 165
5.4.9 Determination of spectral sensitivity 167
5.4.10 Determination of threshold sensitivity 168

6 Conclusion 174

Appendix A: Nomenclature 182

Bibliography 184

List of Tables

1.1 Price points of commercial thermal detectors 8

4.1 Comparison of analytical and finite element models. 111
4.2 Effect of structural layer 114

List of Figures

1.1 Infrared sensors in nature 12
1.2 Infrared image of snake eating mouse 13
1.3 SEM of infrared receptor and wax gland of *Melanophila acuminata* 15
1.4 Infrared receptor of *Melanophila acuminata* (cross section) 16
1.5 SEM of infrared receptor of *Melanophila acuminata* 17
1.6 FTIR spectrograph of PMMA. 21
1.7 FTIR spectrograph of PMMA. 22
1.8 FTIR spectrograph of photoresist 23
1.9 Chemical structure of chitosan and chitin 24
1.10 FTIR spectrograph of chitosan 25

2.1 Schematic diagram of chitosan photolithography process. 39
2.2 SEM cross section of spin-coated chitosan. 40
2.3 Chitosan photolithography process 42
2.4 Surface roughness of chitosan thin film 44
2.5 Localized surface topography measured with AFM 45
2.6 Wet etching of chitosan using acetic acid. 47
2.7 Dry etching of chitosan using oxygen plasma. 48
2.8 Oxygen plasma etch rate. 49
2.9 Surface profile of chitosan step height. 50
2.10 Fluorescently labeled chitin shows improved adhesion after O_2 plasma treatment. 54
2.11 Hydrophobic chitin surface causes poor adhesion with photoresist. 55
2.12 Surface roughening by O_2 plasma treatment. 56
2.13 Schematic of lift-off process for patterning chitosan. 57
2.14 Patterned photoresist prior to chitosan deposition 59
2.15 Chitosan spin-coated over patterned photoresist 60
2.16 Chitosan following lift-off of patterned photoresist using PRS-3000 60

2.17 Attachment of fluorescein-conjugated chitin binding probe to patterned chitosan surface. 65

3.1 FTIR spectrograph of chitin thin film 71
3.2 FTIR spectrograph of chitin thin film 72
3.3 Stress-temperature profile of chitosan (salt form) 73
3.4 Effect of thermal cycling on chitosan film (salt form) 75
3.5 Effect of 150°C anneal on stress vs. temperature hysteresis 77
3.6 Stress-temperature profile of chitin 79
3.7 Effect of thermal cycling on chitosan film (neutralized form). . . . 80
3.8 Incomplete drying not responsible for cycle 1 stress-temperature hysteresis. 81
3.9 Chitin shows moisture absorption after equilibration. 83
3.10 Stress-temperature profile of OCG 825 photoresist. 87
3.11 No hysteresis in OCG 825 photoresist. 88
3.12 Contact angle measurement for chitosan thin film (salt form). . . 90
3.13 Effect of NaOH neutralization on contact angle 91
3.14 Contact angle measurement for chitin thin film. 92

4.1 Cantilever basic concept. 96
4.2 3D finite element model. 110
4.3 Optimal thickness dimensions for bimorph. 113
4.4 Cantilever metal reflector. 121
4.5 Optical prototype fabrication process flow. 122
4.6 Micrographs of optical prototypes. 124
4.7 Capacitive-readout Fabrication Sequence. 127
4.8 Differential measurement beam concept 128
4.9 Cantilever following patterning of second photoresist layer. 129
4.10 Cantilever following etching of polysilicon and prior to oxide release. 129
4.11 Feature after wafer dicing and removal of protective resist. 130
4.12 Released cantilever following removal of oxide with HF vapor. . . 131
4.13 Capacitive readout bimorph fabrication 132
4.14 Released cantilever showing residual stress (focus on anchor). . . . 134
4.15 Released cantilever(300 μm long) showing residual stress (focus on tip). 135
4.16 Effect of polymer processing temperature on residual stress. . . . 137

5.1 Temperature testing apparatus 142
5.2 Cantilever bending downward due to heating. 143
5.3 Cantilever bending upward due to cooling. 144

5.4 Thermoelectric testing with green laser speckle. 147
5.5 2D and 3D white light interferograms. 148
5.6 Irvine Sensors MS3110 Block Diagram. 151
5.7 Photograph of capacitive test board. 152
5.8 Capacitive test subboard assembly. 153
5.9 Die attach and wire bonding to subboard 154
5.10 Optical bench setup for capacitive testing. 156
5.11 Die seen in lens of IR camera. 157
5.12 Test PCB mounted on aluminum fixture. 158
5.13 Graph of detector tracking chopper wheel signal. 160
5.14 Graph showing loss of signal due to obstruction in light path. . . 161
5.15 Graph of detector tracking frequency of chopper wheel. 162
5.16 Voltage drift in the absence of a stimulus. 164
5.17 Time response following chopper signal transition. 166
5.18 Filters used to determine spectral sensitivity. 169
5.19 Feit halogen bulb intensity versus Variac voltage. 170
5.20 Effect of neutral density filters. 172

Chapter 1

Introduction

1.1 Overview

In this chapter, a context is set for the development of a biomimetic, polymer-based infrared sensor. A brief history of the development of infrared sensing is presented. The fundamental equations governing the physics of infrared transduction are identified. The current status of state-of-the-art thermal and photon detectors is examined, and their limitations are identified. Next, there is a focus on infrared sensors that have been found in nature, in particular, the long-range thermal sensor of *Melanophila acuminata*, which serves as the biomimetic inspiration for this thesis. The biomimetic approach, of using the organic bonds of polymers as infrared radios, is defined, and the infrared absorption spectra of photoresist, PMMA, and chitosan (the deacetylated form of chitin, which makes up the infrared sensor in *Melanophila acuminata*), are presented. Design of infrared-

sensitive microelectromechanical systems using these materials is the subject of this work.

1.2 History of Infrared Detection

Infrared detectors have played an important role in military and civilian technology since work began on their development following the discovery by Hershel of the existence of electromagnetic energy beyond the red in 1800. Infrared detection technology came of age in World War II. Initial sensor development focused on thermal detectors, while more recently, photon detectors have received a great deal of investment. Thermal detectors transduce infrared radiation to heat, while photon detectors transduce infrared radiation to an electrical signal without an appreciable change in temperature. In photon detectors, infrared radiation with energy exceeding the bandgap of a semiconductor material causes electrons to move from the valence band to the conduction band. Although photon detectors generally offer superior performance to thermal detectors in terms of detectivity (the primary figure of merit used to evaluate infrared sensors), there are several associated disadvantages that restrict their application. First, photon detectors need to be cooled to reduce noise caused by dark currents. This is usually accomplished by attaching a liquid-nitrogen filled dewar to the detector or camera core.

However, this need for cooling increases the weight, size, and cost of the total sensor package, and therefore restricts its application. In addition, the coolant has a limited shelf-life, which may be of significant consequence in military operations where refilling the dewar is simply not possible. Today, there is a resurgence of interest in high performance, uncooled thermal detectors, driven by applications that require light weight, low cost, and low power [1].

1.3 Governing Equations

The physics of infrared detection is well developed. Infrared detectors are designed to respond to wavelengths in the infrared portion of the electromagnetic spectrum that correspond to the heat signature of a target object. All objects with finite temperature emit electromagnetic radiation, primarily in the infrared region of the spectrum. This non-contact method of measuring heat in the environment allows for remote sensing of objects, even in the absence of visible light (because infrared is primarily emitted rather than reflectted), or the presence of fog or smoke (due to its transparency in the IR). In this section, the principles and equations governing the emission and detection of infrared energy are presented.

1.3.1 Stefan-Boltzmann Law

The Stefan-Boltzmann law defines the irradiance, or power density, of a blackbody due to its temperature, according to the equation:

$$\frac{P}{A} = \epsilon \sigma T^4 \tag{1.1}$$

where P is power, A is area, ϵ is the emissivity, σ is the Stefan-Boltzmann constant and T is the temperature in Kelvin. A blackbody is an object that absorbs all wavelengths of electromagnetic radiation.

1.3.2 Planck's Law

Planck's law describes the intensity, I, of a blackbody as a function of its temperature and wavelength:

$$I(\lambda, T) = \frac{2hc^2}{\lambda^5} \frac{1}{e^{\frac{hc}{\lambda k T}} - 1} \tag{1.2}$$

1.3.3 Wien's Displacement Law

Wien's displacement law describes the wavelength of peak intensity emitted by a blackbody of temperature, T. Wien's displacement law is a special case of Planck's law, and may be obtained through differentiation:

$$\lambda = \frac{2898\mu m \cdot K}{T} \tag{1.3}$$

1.3.4 Detectivity (D*)

Detectivity is a figure of merit for infrared detectors. The unit is $cm\sqrt{Hz}/W$ which is also known as Jones.

$$D^* = \frac{(A\Delta f)^{1/2}}{\Phi}(SNR) \tag{1.4}$$

where A is the area of the detector, Δf is the frequency bandwidth, Φ is the radiant flux due to the signal, and SNR is the signal-to-noise ratio.

1.3.5 Noise Equivalent Temperature Difference (NETD)

The noise equivalent temperature difference is an indication of temperature resolution and is an important performance metric for thermal sensors.

$$NETD = \frac{4}{\pi} \frac{f_{\#}^2 \sqrt{\Delta f}}{\tau_{op} \sqrt{A} D^* \frac{\Delta L}{\Delta T}} \tag{1.5}$$

where $f_{\#}$ is the f-number of the optics, Δf is the frequency bandwidth, τ_{op} is the transmission of the optics, A is the area of the detector, D^* is the detectivity, ΔL is the change is radiance, and ΔT is the change in temperature. The NETD is the change in temperature that will produce a change in voltage equal to the average noise seen by the detector, and is typically measured in units of mK.

1.4 Active vs. Passive Infrared Detection

Night vision, though sharing similar applications to the passive infrared detectors, differ in that the “active” night vision systems amplify low light levels. In contrast, no visible light is needed when using passive infrared detectors, as the passive detectors are detecting the infrared light emitted due to a body’s heat. In the absence of all illumination, active night vision will fail while passive infrared detectors will still operate as they are sensitive to electromagnetic energy emitted due to the heat of a warm body rather than the presence of visible light.

1.5 Thermal Detectors

Thermal detectors received a great deal of initial attention, as they provide uncooled detection. They generally have broadband responses, whereas photon detectors may be sensitive to very narrow frequency ranges. Examples of thermal detectors are the bolometer, the pyroelectric, and the Golay cell [2].

Bolometers convert a temperature change to a resistance change, pyroelectrics to a change in charge (and hence a change in capacitance), and Golay cells to a change in pressure. For a review of bolometer technology, the reader is directed to Richards [3]. A thorough review of the current status and trends of the infrared marketplace are presented by Rogalski in [4].

Recently, there has been a resurgence of interest in uncooled thermal detector technology due to its low cost, which opens up the infrared market to commercial applications [4]. One example of the commercial market for low-cost infrared sensors is night vision applied to pedestrian avoidance systems for the automotive market [5]. These exist in both near-infrared ("'active"' night vision) and far infrared (passive IR detection) formats with far infrared offering a better range [5]. A comparison of costs of various commercially-available thermal detectors is shown in Table 1.1.

Status	
Feature	Cost ($)
Commercial marketing of military thermal imagers	
Overspecified for commercial applications	
320 × 240 pixel, 50 × 50 µm bolometer arrays for thermal imagers	15 000–20 000
320 × 240 pixel, 50 × 50 µm bolometer arrays for imaging radiometers	20 000–50 000
120 × 1 pixel, 50 × 50 µm thermoelectric arrays for imaging radiometers	15 000
320 × 240 pixel, 50 × 50 µm hybrid ferroelectric bolometer array imagers for drivers' vision enhancement	2 000–4 000
Trends	
Developed of new, low-cost thermal imagers and imaging radiometers	
Designed for specific commercial applications and meeting commercial requirements	
160 × 120 pixel, 50 × 50 µm bolometer arrays for thermal imagers	<3 000
160 × 120 pixel, 50 × 50 µm bolometer arrays for imaging radiometers	<5 000
160 × 120 pixel, 50 × 50 µm bolometer arrays for driver's vision enhancement systems	<2 000
160 × 120 pixel, 50 × 50 µm bolometer arrays for driver's vision enhancement systems in extremely large volumes	1 000

Table 1.1: Price points of commercially available thermal detectors. From Rogalski [4].

Research has focused on two areas: microbolometers and microcantilever-based detectors. The microbolometer is formed of a high temperature coefficient of resistance (TCR) material such as VO_x. VO_x is the current material of choice for uncooled thermal sensors because it has a high negative TCR (4%) at room temperature [6]. The VO_x microbolometer is commercially available from Honeywell and is the current state of the art thermal detector. Recently, microcantilever-based infrared sensors using MEMS fabrication processes have been an area of active research. Li [7] proposed a double-cantilever infrared sensor formed of

bimorphs of aluminum and low stress SiN_x. A polymer-based microcantilever which enhances the coefficient of thermal expansion (CTE) mismatch compared with traditional metal-semiconductor designs is the subject of Chapters 4 and 5 of this dissertation.

1.6 Photon Detectors

Photon (or quantum) detectors are another distinct class of infrared detectors and are primarily composed of either III-V and II-VI semiconductors. In a photon detector, the absorbed photon interacts directly with electrons in the material, and an electronic output signal is read out [6]. Unlike thermal detectors, photon detectors experience no appreciable change in temperature during the transduction process. Rather, when incident infrared radiation strikes the detector with energy exceeding the bandgap, infrared photons stimulate the creation of electron-hole pairs, which generates a change in conductance (photoconductive) or change in voltage (photovoltaic). Because their operating spectral range is determined by the bandgap of the material, photon detectors are generally narrow band. Ex-

amples of photon detector materials include HgCdTe and the lead salts, PbS and PbSe.

$$h\nu \geq E_g \tag{1.6}$$

Because the incident energy must exceed the bandgap of the material, the spectral sensitivity of photon detectors is limited. For example, silicon-based detectors are limited to detecting wavelengths of up to approximately 1 μm, PbS and InGaAs are limited to 3 μm, and InSb, PbSe and PtSi are limited to 6 μm [6]. HgCdTe is limited to either 6 μm or 15 μm depending on which atmospheric window it is optimized for [6].

Although photon detectors generally offer superior detectivity D* (on the order of 10^{10}) and faster response time (μs) than thermal detectors (where detectivity is on the order of 10^8 and response time is in ms), their primary disadvantage is that at ambient temperature, the detectors suffer from significant dark currents and therefore require cryogenic cooling to increase the signal to noise ratio. Cooling is generally accomplished by attaching a liquid nitrogen (LN) filled dewar to the camera core, which cools the detector to 77 K. Cryogenically cooled thermal imagers can cost as much as $50,000 [6]. Alternatively, closed-cycle refrigeration can be used in place of a cryogenic liquid [2]. Although the use of closed-loop

refrigeration systems eliminates the need for liquid cooling, detectors using this method still have limited shelf life due to increased power consumption which will ultimately drain the battery. Additional disadvantages of closed-loop refrigeration systems include cool down times that can range from 3 - 30 minutes, cooling system weight of 10-30 lb, and the introduction of vibrational noise into the infrared system [2]. In both cases, cooling significantly increases the system size, weight, and cost, while also reducing the maintenance-free operating time of the camera. As a result, photon detectors are well-suited for space-based applications but have found limited application in ground-based IR detection.

1.7 Nature's Infrared Detectors

For more than 50 years, infrared detection has been observed in nature, primarily in the insect world. Grant first suggested that insect antennal sensory pits may function to detect heat radiation [8]. Grant [8] suggested the mechanism of these sensory pits to be based on dielectric wave guides and resonance, with the geometry and cross-sectional dimensions of the cavity determining the wavelengths of infrared light which are detected. Infrared detectors have since been found in various forms in several types of insects and snakes.

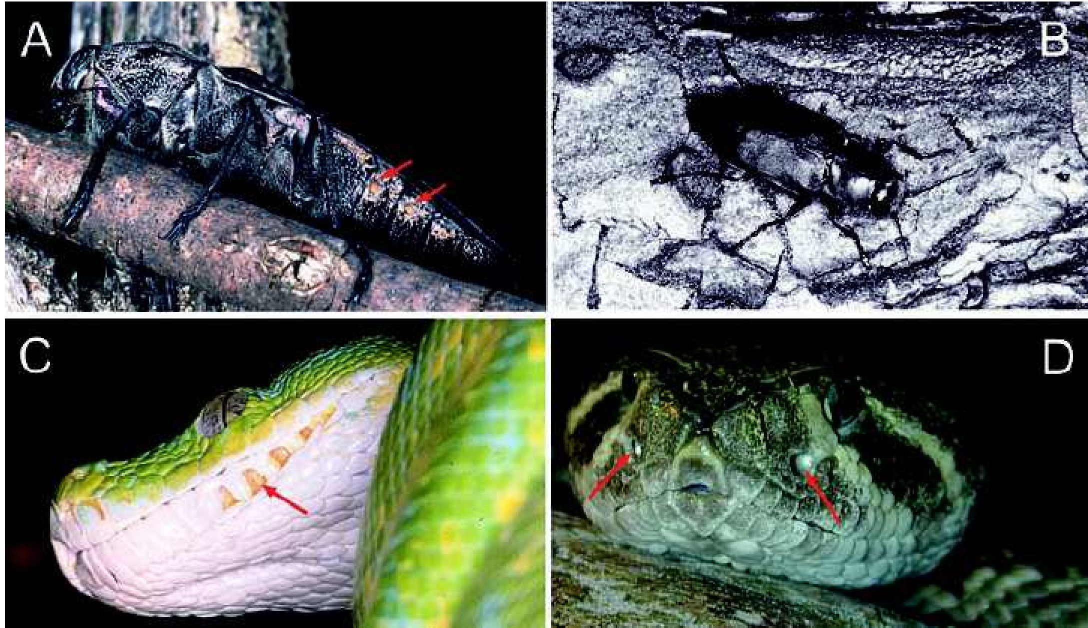

Figure 1.1: Infrared sensors in nature a) *Merimna atrata* b) *Melanophila acuminata* c) Boid snake d) Crotaline snake [9].

1.7.1 Crotaline and Boid snakes

Crotaline and Boid snakes contain a thermoreceptor pit organ used to detect warm-blooded prey and warn of predators. Snakes detect infrared energy and longer wavelengths (lower energies), generally in the 8-12 μm band [10]. The detector operates at short distances, typically less than 1 meter. These sensors are able to detector small variations in temperature. For example, the rattlesnake can detect a change of 0.003 K while the Boid snake can detect a change as small as 0.026 K [11]. The infrared sensory structures in snakes have a high concentration of adenosine triphosphate, succinic dehydrogenase and lactic acid dehydrogenase,

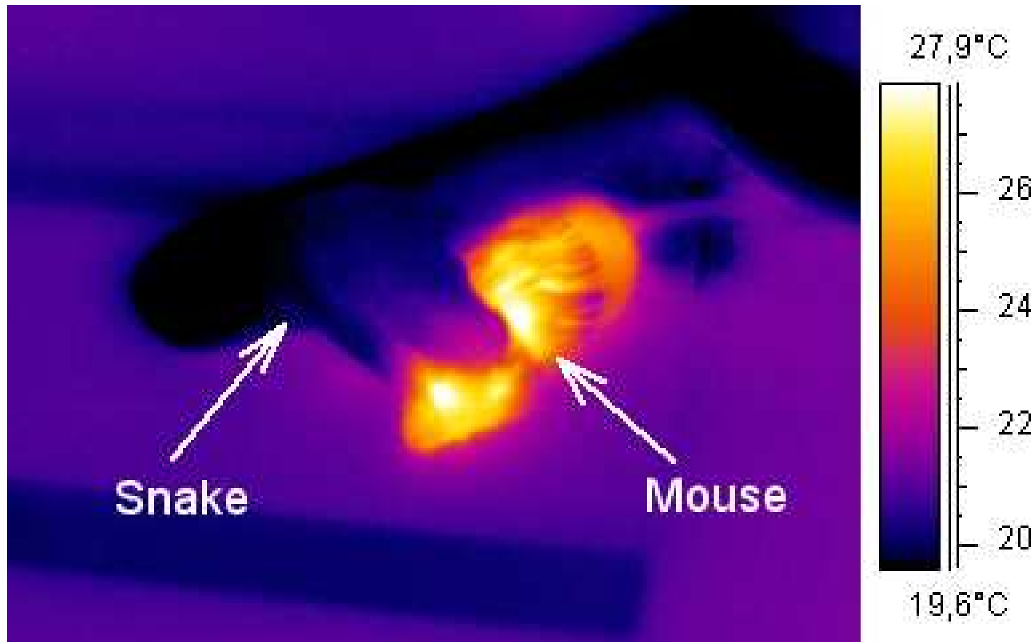

Figure 1.2: Infrared image of snake eating mouse. Image obtained under GPL.

as well as a high concentration of mitochondria [11]. The mitochondria has been observed to change its configuration due to IR irradiation [11], and therefore may be classified as a photomechanical molecule.

1.7.2 *Melanophila acuminata*

The jewel beetle, *Melanophila acuminata*, is of particular interest for study as the basis for a biomimetic infrared sensor because of its ability to detect forest fires from a distance of 60-100 miles [11]. The beetle seeks out forest fires in order to lay its eggs in freshly burnt wood free of predators. Initially, it was believed that the insect was attracted to smoke and used olfactory sensing to locate the

fire [12]. However, Evans [12] disproved this hypothesis and instead found that the sensors detect infrared radiation. The insect contains two sense organs, one on each side of its coxal cavity about 450 μm by 200 μm and each organ contains an array of approximately 70-100 individual sensilla. Each sensillum has a diameter of approximately 15 μm [13]. The division of the organ into an array of sensilla may function to thermally isolate the individual sensilla while also allowing for the determination of spatial information [14]. In addition, each sensilla contains an adjacent wax gland, as shown in Figure 1.3. The wax secreted by the wax gland may serve as nature's technique for packaging the microstructure. The wax may prevent dirt from collecting in the beetle's pit organ [15]. With time, the wax is sloughed off and removes any attached dirt particles. Once removed, the wax is replaced within 64-96 hours [13]. The wax is transparent to IR except for a very narrow absorption peak at 3.4 μm [16]. Therefore, the wax may also function as a bandstop filter though it is unclear what is achieved by filtering out the 3.4 μm wavelength. Furthermore, the wax may function as a barrier to moisture [15, 16]

A number of *in vivo* experiments have been conducted on the jewel beetle to determine how its infrared sensor functions and to quantitatively determine its performance. For example, Hammer et al. [10] used a He-Ne laser operating at 3.39 μm to conduct electrophysiological experiments in order to determine the threshold sensitivity of the jewel beetle. They found sensitivity at the receptor

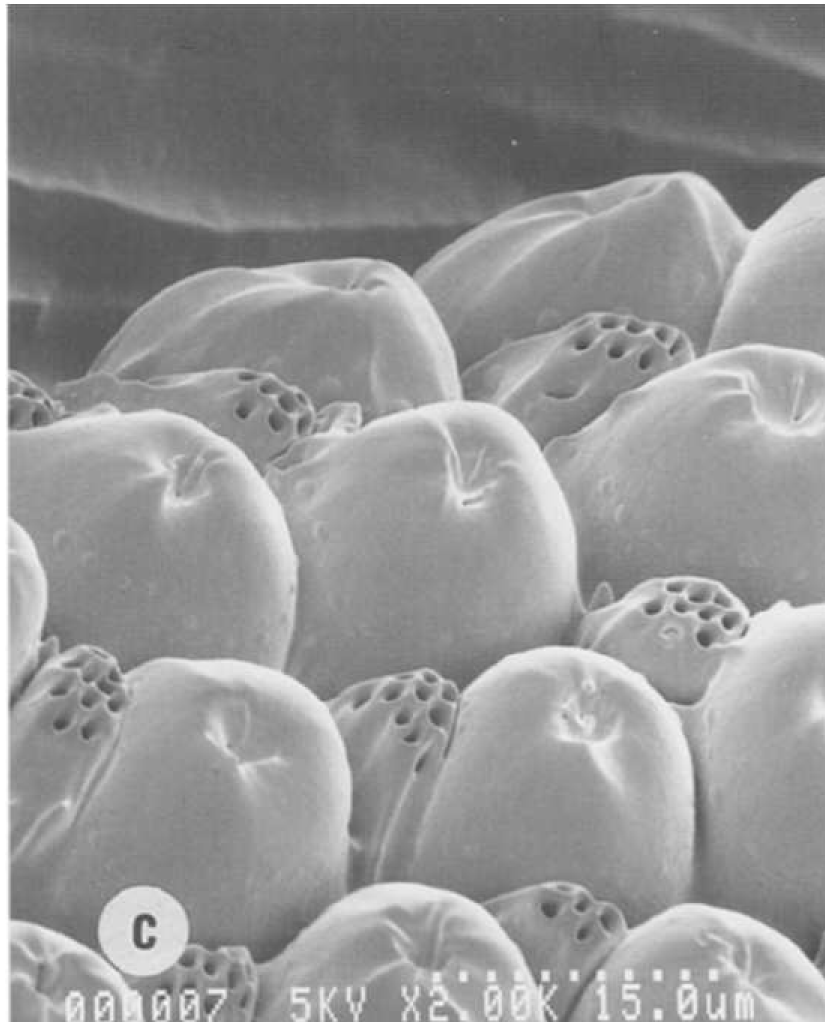

Figure 1.3: SEM of infrared receptor and wax gland of *Melanophila acuminata* [17].

(sensilla) at this wavelength to be 17.3 mW/cm^2. Absorbed infrared radiation causes expansion of the sensory structure by approximately 1 nm, which is sufficient to be detected by insect mechanoreceptors [15].

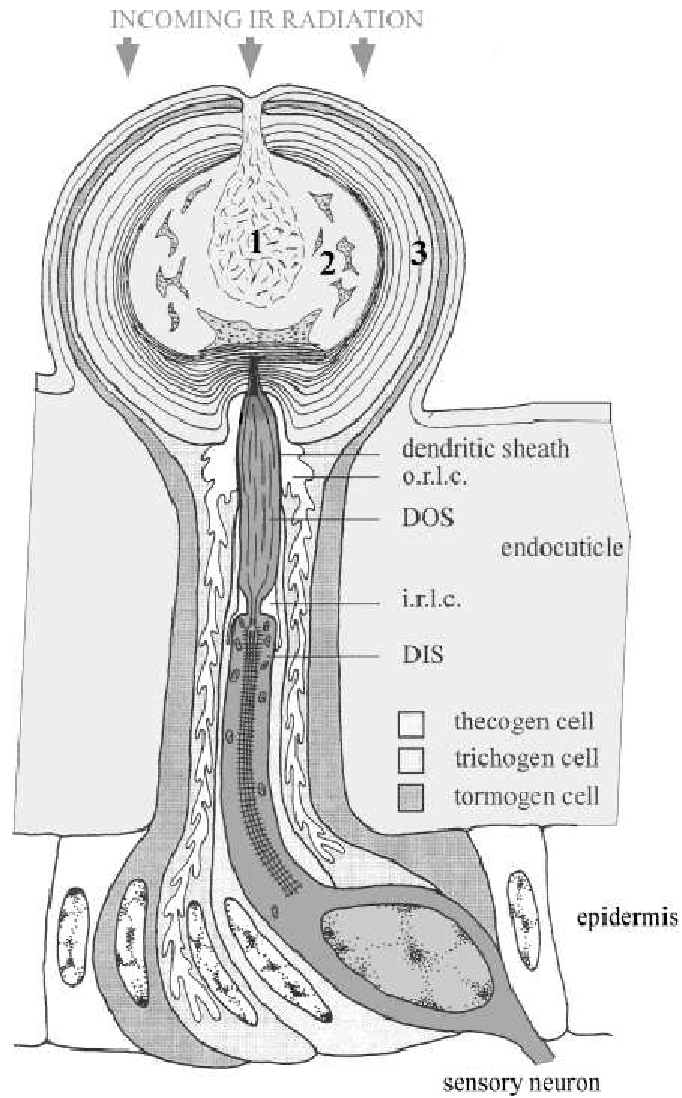

Figure 1.4: Schematic diagram of cross section of infrared receptor in *Melanophila acuminata* [18].

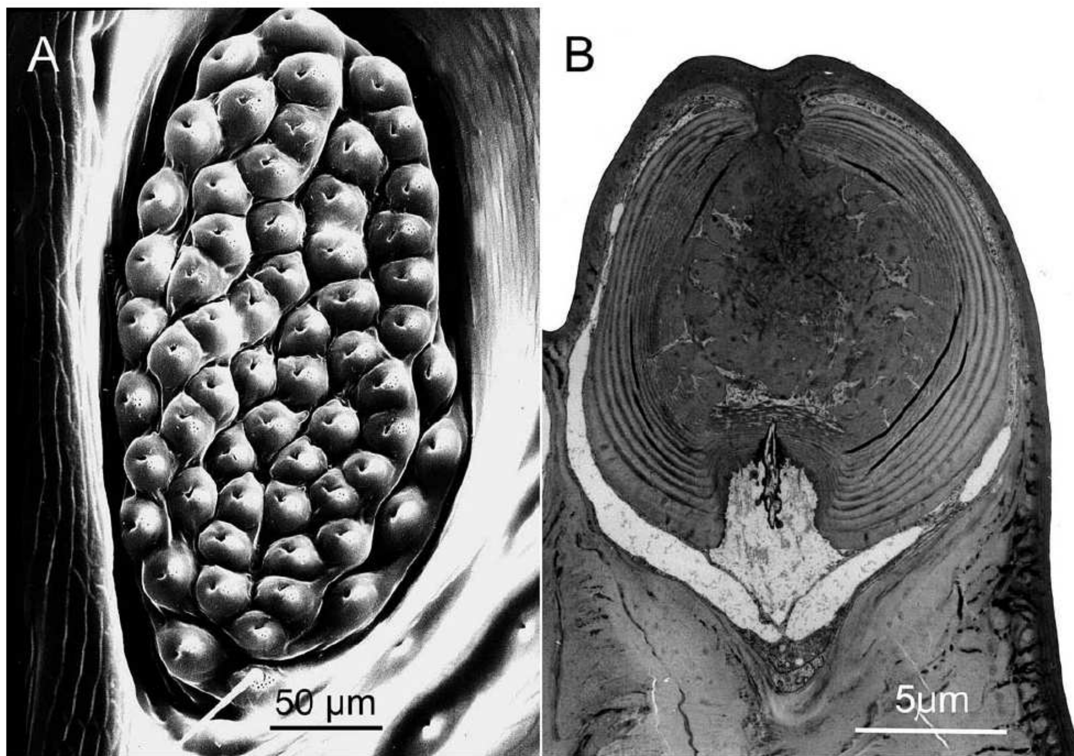

Figure 1.5: SEM of infrared receptor of *Melanophila acuminata* [9].

Evans [16] recently offered an alternative to the photo-thermal-mechanical hypothesis of Hammer *et al.* [19] by describing a thermopneumatic model (similar to a Golay cell) for the IR receptor in *Melanophila acuminata*. Evans describes the IR organ as an air tight, enclosed area with thick walls with a thin chitinous lining. In this model, the insect's wings serve as a chopper wheel to produce a pulsated IR signal. Air is radiantly heated, which causes it to expand, and by increasing the pressure, triggers deformation of the tubular body which ultimately results in an action potential. In this model, the IR radiation is absorbed by the thin, inner chitinous lamella which in turn heats the cavity air by conduction and convection.

1.7.3 *Merimna atrata*

Another fire-seeking beetle found in nature is the Australian fire beetle *Merimna atrata*. The IR organ in *Merimna atrata* differs from that in *Melanophila acuminata*; its infrared absorbing area is nearly round with a diameter from 300-400 μm and is found at the second and third abdominal sternite [20]. Each sensor is innervated with a single multipolar neuron. There is a large number of mitochondria in the terminal dendrites [20]. The frequency of neural recordings was found to be highly sensitive to changes in temperature while being unaffected by sound, air movement, or gentle touch [20]. Temperature increases regardless of

source (broadband IR radiation, warm air, 660 nm He-Ne laser) were found to increase spike frequency [20]. Responses were found to occur with temperature changes as small as 700 mK [20]. Responses are similar to those of Crotaline and Boid snakes [20]. The sensor found in *Merimna atrata* as well as Crotaline and Boid snakes is most similar to a bolometer [20].

1.7.4 Ecological Partitioning of Bandwidth

Natural selection has played an important role in the development of the infrared sensory system in insects and snakes, and it is interesting to note the similarities our own electronic communication systems have developed (perhaps without our conscious realization) to those that have existed in nature for millions of years. Natural selection has driven the development of infrared sensory systems to adopt to the atmospheric windows at 3-5 μm and 8-12 μm, and to also adopt to the wavelength of the target, whether it be a forest fire or a predator. In addition, the infrared sensory system may be seen as nature's way of allocating the electromagnetic spectrum to minimize crosstalk, much like the partitioning of bandwidth by the FCC. From an ecological point of view, this is analogous to each species forming its own electromagnetic niche. One additional advantage that ectotherms have due to their ability to match their body temperature to the environment is to evade detection by infrared means.

1.8 Polymers as Infrared Materials

Polymers are interesting materials for infrared sensing applications because of their high infrared absorption due to vibrational resonance modes of their organic bonds and their high coefficient of thermal expansion compared to metals and semiconductors. Additional energy transduction may occur by morphological changes in the molecules themselves: changes in conformational structure, rearrangements in crystal structure, and alterations in inter-molecular and intra-molecular bonding. The high infrared absorption seen in the tissue of the jewel beetle *Melanophila acuminata* from 2.8 to 3.5 μm has been correlated to the vibrational stretch resonances of the O-H and C-H bonds [14].

1.8.1 Polymethyl methacrylate (PMMA)

PMMA is a commonly used material in microfabrication. It has been used as an e-beam resist. It is highly homogeneous material with largely repeated structure. Its structure shows strong absorption at specific wavelengths, corresponding to the few, highly repetitive bonds found in the chemical compound.

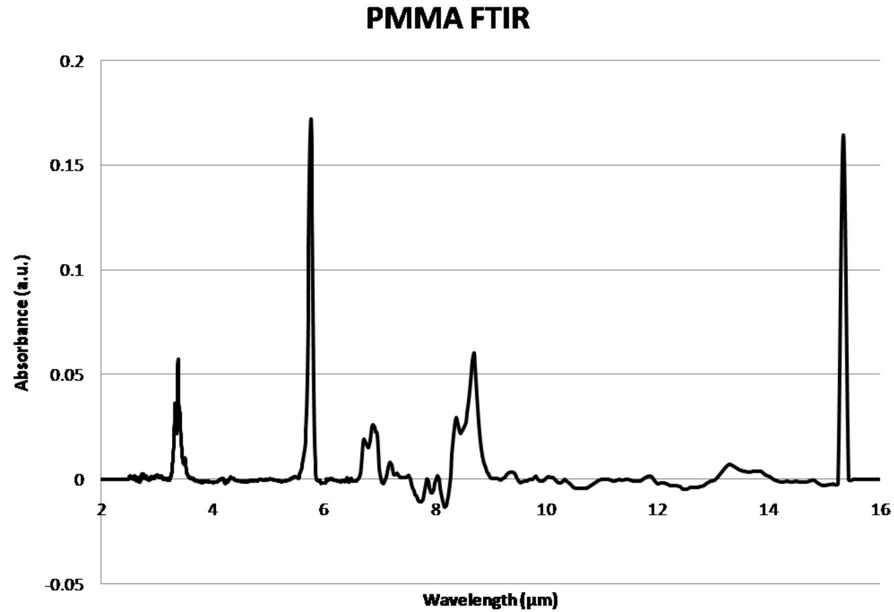

Figure 1.6: FTIR spectrograph of PMMA.

1.8.2 Photoresist

Photoresist is by far the most commonly employed polymer in the semiconductor manufacturing industry. It is a composed of several materials, including novolak resin, a photoinitiator, and a casting solvent [21]. When hard baked, it becomes fully cross-linked. Due to its many chemical constituents, which results on a variety of different bonds between atoms and molecules, its infrared sensitivity is fairly broadband, as shown in Figure 1.8.

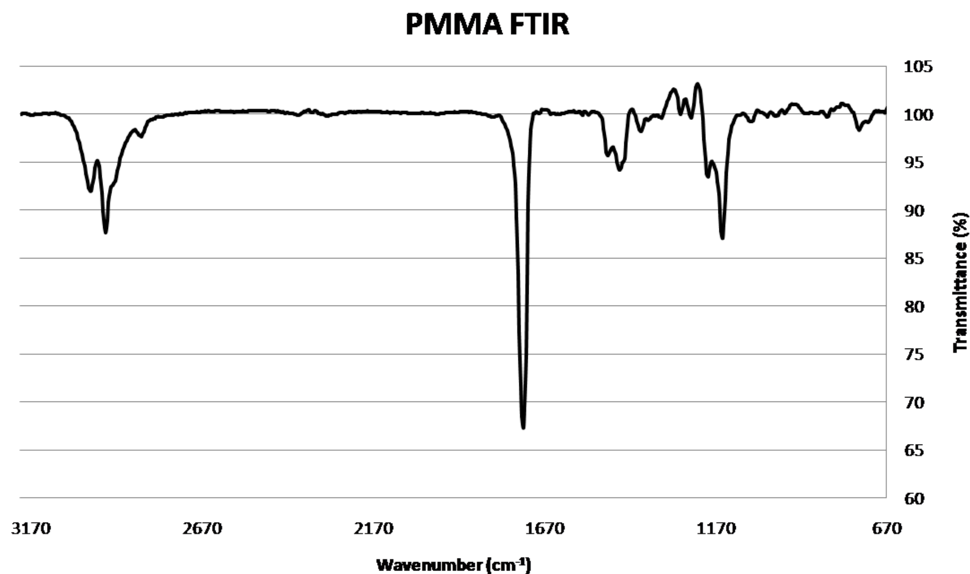

Figure 1.7: FTIR spectrograph of PMMA.

1.8.3 Chitin/Chitosan

Chitin, a β-1,4-linked polysaccharide, is a primary component of the infrared sensilla in *Melanophila acuminata* and also has peak absorption at 3 μm, matching the peak wavelengths emitted by forest fires. Furthermore, since all known photopigments have peak absorption below 700 nm [19], there are no known infrared-sensitive proteins analogous to rhodopsin (which operates in the visible portion of the spectrum). IR energy with a wavelength greater than 1 μm does not have sufficient energy to trigger molecular switches such as visual pigments [17], which essentially rules out operation as a photodetector. The correlation of the beetle's infrared wavelength sensitivity to the optical absorption properties of the mate-

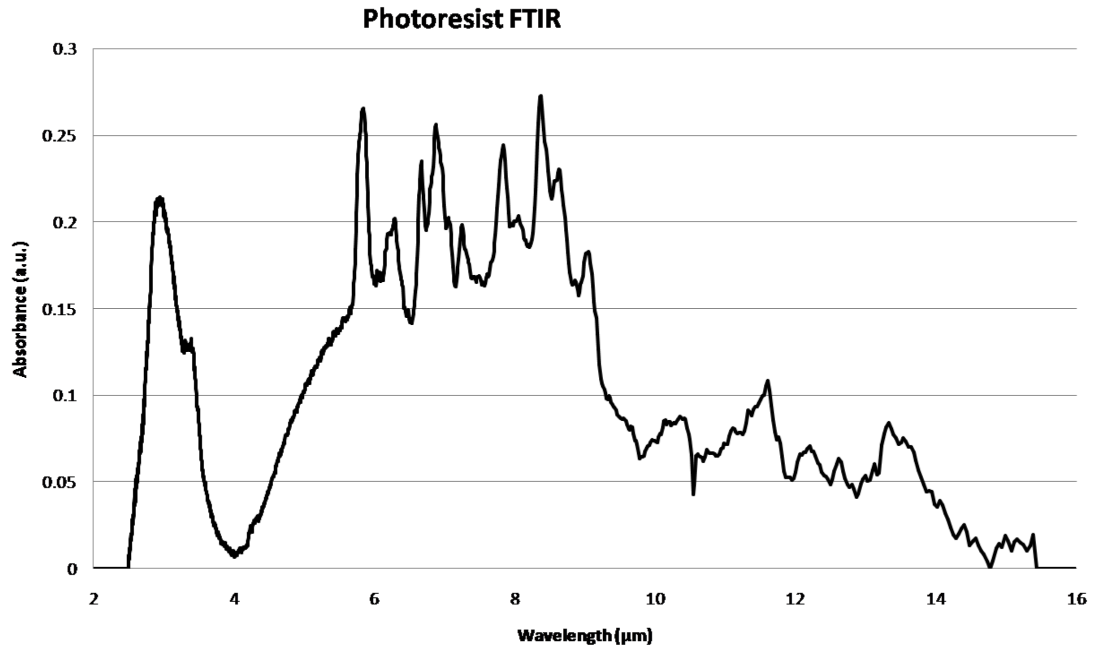

Figure 1.8: FTIR spectrograph of photoresist

rials found within the insect sensillum suggests that chitin is intimately involved in the functioning of the infrared sense organ of *Melanophila acuminata*. Further investigation of the material properties of chitin, and its deacetylated derivative chitosan, which will be discussed in Chapters 2 and 3, provides additional insight into the role of chitin in nature's infrared detection.

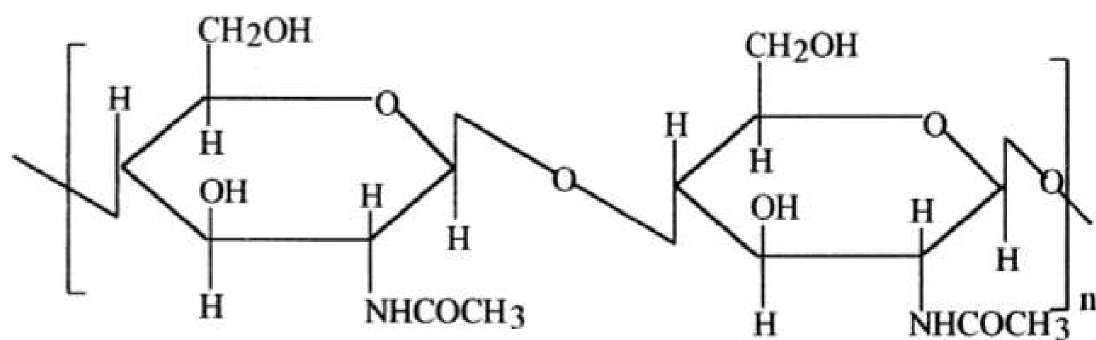

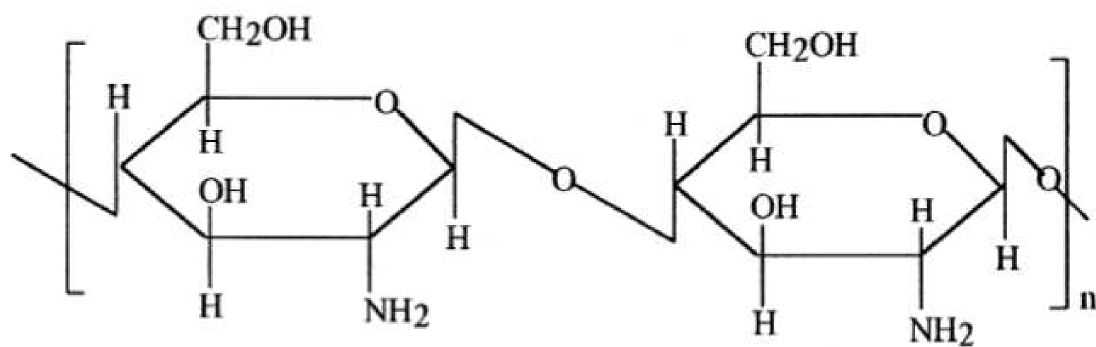

Figure 1.9: Chemical structure of chitosan and chitin [22].

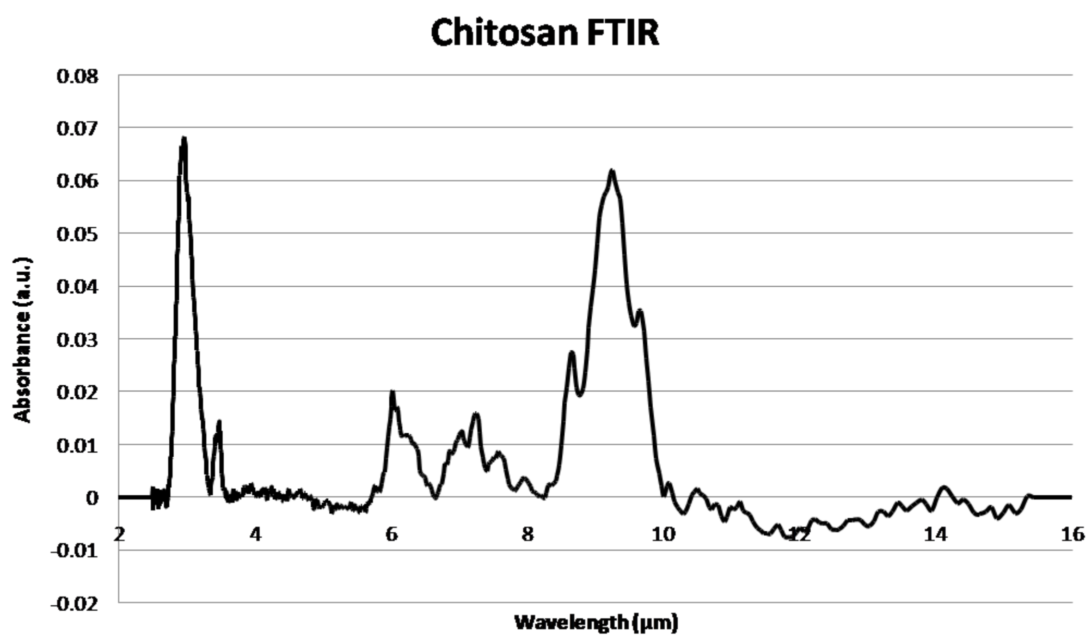

Figure 1.10: FTIR spectrograph of chitosan

Chapter 2

Chitin Microfabrication

In this chapter, a photolithography process is presented for microscale patterning of chitosan and chitin thin films for incorporation in microelectronics and microelectromechanical systems (MEMS) fabrication processes. Chitin is a structural material found throughout nature. Chitosan, the deacetylated derivative of chitin, has biological properties that make it favorable for tissue engineering, protein engineering, and sensor applications.

In this work, a chitosan thin film is formed on a silicon wafer by spin-casting a solution of chitosan in acetic acid. The thin film is covered with photoresist, which is exposed to UV light through a photomask. Chitosan may be selectively removed using oxygen plasma for dry etching or acetic acid for wet etching. The process allowed the resolution of features as small as 10 μm. Films were observed using optical, fluorescence, and scanning electron microscopy and characterized using FTIR, ellipsometry, and surface profilometry. A fluorescently labeled recom-

binant protein was used to demonstrate that the functional groups of chitosan are preserved and available for biomolecule attachment after spin-casting, photoresist development, and photoresist stripping, making the process of particular interest for patterning proteins and as a micro-nano interface. This process enables the use of chitosan and chitin thin films as layers in microelectromechanical systems.

In this chapter, the properties of chitin and chitosan are described, methods and results for photolithographic patterning of both chitosan and chitin are developed, issues such as adhesion are addressed, and advantages and disadvantages of each technique are analyzed.

2.1 Background

To explore chitin as a biomimetic material with potential application to infrared sensing required a method of depositing and patterning the material as a thin film. While recent efforts have investigated electrodeposition, spin-casting and nano-imprinting, none of these methods were developed enough to allow integration of the material into a processing sequence for the development of microelectromechanical devices. In fact, photolithography, by far the most commonly employed technique for patterning thin films for both the development of

integrated circuits and microelectromechanical systems, had not been previously explored for chitosan or chitin.

Here, the first photolithographic patterning of the polysaccharide chitosan on a silicon wafer is presented. Photolithographic patterning of chitosan films allows the formation of spatially-selective microscale features while preserving the functional groups that provide chitosan its interesting material properties. Integrity of chitosan films was verified throughout the photolithography process by attaching a protein coupled with a fluorescent dye following spin-casting, photoresist development, and photoresist stripping. Furthermore, chitosan photolithography provides another means to achieve the micro-nano interconnect described by Payne and Raghavan [23]. Chitosan photolithography is advantageous because of its batch-fabricated, high-resolution production of features that may be integrated into MEMS processes without the requirement of a conducting surface. The chitosan lithography process developed and described in this thesis enables novel applications in chemical and biological sensing, and optical/infrared detection. The ability to deposit and pattern biomolecules on microscale chitosan scaffolds enables many applications in tissue, protein, polymer, and nanoengineering.

2.2 Properties of chitin

Chitin, a β-1,4-linked polysaccharide, serves as a structural material throughout nature, and is second in abundance only to cellulose. Chitin is a major constituent of the exoskeletons of insects and crustaceans, and is also found in the infrared sense organs of the jewel beetle *Melanophila acuminata* [24]. It is the most abundant nitrogenous polysaccharide [22]. Commercially extracted chitin (and chitosan) is obtained as a byproduct of shellfish processing, making the material readily available and low cost. Chitin is white, hard, inelastic; it serves as a chelating agent due to its high percentage of nitrogen [22]. Chitin is also highly hydrophobic [22].

Chitin has many favorable properties for sensing applications, including chemical resistance, biocompatibility, biodegradability, a high coefficient of thermal expansion, the ability to serve as a scaffold for DNA and other biomolecules, and its ability to function as a chelating agent. These properties have made chitin suitable for use in a variety of commercial applications such as sutures, controlled drug release, prosthetic and implant coatings, anti-cancer and weight loss drugs, and wastewater treatment [22]. The ability to functionalize the surface using a variety of chemical reactions extends its potential [25]. Although the chemical,

mechanical, optical, and biological properties make chitin of interest for a variety of applications, its ability to be processed is severely limited.

2.3 Disadvantages of chitin

One of the primary challenges in the direct processing of chitin is its insolubility and low chemical reactivity [22]. It is highly crystalline and has limited solvents available for processing [22]. Chitin is insoluble in common acids and bases, and does not dissolve in water. The high chemical resistance of chitin further limits its processability. However, chitosan, a deacetylated derivative of chitin, is soluble in dilute acids, and this enables processing that requires a solution phase. Reacetylation allows chitosan to be converted back to chitin.

2.4 Properties of chitosan

Chitosan has a high degree of intra- and intermolecular bonds which adds mechanical strength but prevents processing techniques commonly used with traditional thermoplastics [26]. In addition, the presence of amine and carboxylic acid groups facilitates protein immobilization and the absorption of metal ions [27]. Both chitosan and chitin are highly basic polysaccharides [22]. Because of the

presence of primary amino groups, chitosan undergoes chemical reactions typical of amines [22]. Chitosan is soluble in dilute acids such as acetic acid [22].

2.5 Shelf Life

One important consideration in the preparation of materials for chitosan and chitin photolithographic processes is the shelf life of the materials. Shelf life is particularly important in a research environment where relatively low volumes of reagents are consumed and are used less frequently and kept for longer periods of time that would be typical of a production environment. Sorlier *et al.* observed a slight increase in viscosity, the pH is relatively stable following an initial drop [28]. Kam *et al.* investigated the effect of storage (time) on thin films of chitosan [29]. They found that the conformation gradually changed toward an anhydrous form as acetic acid molecules and water were removed during storage [29]. This anhydrous polymorph was also obtained by annealing [29].

2.6 NaOH Treatment

Chitosan cast as a thin film using a solvent such as acetic acid may form a chitosan salt (variously described as chitosan acetate or chitosonium acetate) on the substrate surface. This salt form of chitosan results from electrostatic

interactions between the chitosan and the acid. To remove any residual acid and eliminate the salt form of chitosan on the cast surface, the wafer may be neutralized with a 0.1 M NaOH treatment for 5 minutes.

2.7 Reacetylation

Reacetylation (or N-acetylation) is a process used to convert chitosan to chitin. The process may use acid anhydrides or acyl halides to attach amido groups at the nitrogen on chitosan [22]. In addition, the reacetylation process confers significant changes in the chemical and mechanical properties of the film, which reflects the importance of the degree of acetylation and the differences between chitosan and chitin. In this thesis, acetic anhydride was used in the reacetylation process to restore the acetyl groups onto the chitosan amine groups and convert the chitosan to chitin. A wafer may be placed in a solution of 5% v/v acetic anhydride in methanol at room temperature overnight. The wafer is then washed in DI water and allowed to dry.

2.8 Prior art

While the use of chitosan and chitin as a material in microelectromechanical systems (MEMS) is a relatively new area of research, recent work has explored

several techniques commonly employed in microfabrication processes, including electrodeposition, spin-coating, and nanoimprinting.

2.8.1 Chitosan Electrodeposition

Due to the presence of the chitosan amino group, which has a net positive charge that forms cations in solution, chitosan may be electrodeposited onto a biased surface. Thickness may be adjusted based on the deposition time, the electrode bias, and the chitosan concentration in solution [30]. Chitosan is deposited onto the negative electrode due to its net positive charge in acidic conditions. The amino groups in chitosan have a pKa of approximately 6.3 [30]. In 2002, Wu *et al.* demonstrated the use of an applied voltage to deposit chitosan onto a negatively biased (200 nm gold on 9 nm chromium) electrode. Although it is claimed that no deposition occurs for the positive electrode, this is unlikely due to the possible deposition technique of dip-coating, which is essentially what takes place when a neutral electrode is placed in the acidic chitosan solution. This work was followed in 2003 by the successful demonstration of the electrodeposition of chitosan onto an electrode pattern photolithographically defined on a silicon wafer [31].

There are several disadvantages to using electrodeposition for integrating chitosan films into MEMS devices. First, the need for a patterned electrode for chitosan deposition restricts placement to conducting surfaces, and formation of

multiple chitosan layers is cumbersome. Second, the electrodeposition of chitosan forms an electrical insulator over the electrode, forming a self-limiting deposition. Furthermore, electrodeposition traditionally uses a patterned, interconnected metal trace across the entire wafer to achieve batch fabrication; this can be disadvantageous for applications that require isolated metal structures or metal traces carrying different potentials across the chip. Research done for this thesis shows that when using acetic acid as the solvent, the acid attacked the Cr adhesion layer, lifting off the Au electrode after several minutes.

2.8.2 Chitosan Spin-coating

Spin-coating offers an alternative to electrodeposition as a method for depositing chitosan on a surface. Spin-coating is an integral part of all photolithography processes and is also used in nanoimprinting.

Ligler *et al.* was the first to demonstrate a spin-coating process for chitosan with high uniformity [32]. Their motivation was to control the thickness and index of refraction to mimic the layering of material found in butterfly wings and crab shells for diffraction grating applications. Their chitosan was crosslinked and used a placticizer in order to stabilize the film against changes in humidity and temperature. Ligler *et al.* achieved reproducible thicknesses with uniformity of 3-5% across the silicon wafer.

Ligler *et al.* identified an adhesion issue between chitosan and silicon; however, this problem with not observed by Jiang [33] or during this work. Ligler *et al.* used polyvinyl butyric resin (Butvar-98) as an adhesion promoter between the silicon and the chitosan. In addition, they tried using aminosilane monolayers and polyelectrolytes but found neither to function as an adhesion promoter. The chitosan used by Ligler *et al.* was modified by acid cleavage to shorten the chain length, and further deacetylated using a strong base. They also investigated using plasticizers to prevent cracking or peeling caused by environmental changes. Tetraethylene glycol was found to offer superior performance in this regard.

A 2.5% chitosan / 2.5% Resimene / 0.25% plasticizer solution in 2.5% acetic acid was used for spin-coating in their work. Chitosan solution was dispensed onto the wafer within 10 minutes of solution preparation. This was likely necessitated by the presence of a cross-linking agent. Films were spun at 1,000 rpm for 30 seconds. All films spun immediately after dispensing the solution on the wafer were found to have thicknesses of approximately 20 nm. To increase the film thickness, a preincubation step was used on the dispensed solution (1 hour at 25°C) to facilitate polymerization. The polymerizaton process likely increased the viscosity of the solution, which causes the spin-coated film to have increased thickness. Following spin-coating, chips were baked at 80°C for 1 hour. All film thicknesses achieved in this process were less than 250 nm.

2.8.3 Chitosan Nanoimprinting

Tan *et al.* demonstrated the successful patterning of chitosan by plasticizer-assisted nanoimprint lithography. [27]. They added a plasticizer (glycerol) to the chitosan solution to facilitate its use at low pressure (10 kPa) and temperature (25°C), which allowed patterning of nonthermoplastic chitosan by conventional nanoimprinting. Conventional nanoimprinting requires the use of temperatures 50 to 100 degrees above the glass transition temperature and pressure of approximately 5 MPa in order to pattern thermoplastic polymers [27]. Nonthermoplastic materials such as chitosan are difficult to pattern using conventional nanoimprint lithography because the mechanical properties vary little over a broad temperature range.

The chitosan used in their work was 1% w/v in 1 M acetic acid with glycerol loading from 1:1 to 6:1. The plasticizer was added to improve the flowability of the chitosan by lowering its viscosity. Using a 1:1 glycerol:chitosan loading ratio, they achieved a 50 nm thick chitosan film by spin-coating at 3,000 rpm for 30 seconds. With a 2:1 glcyerol to chitosan loading ratio, film thickness was found to be 170 nm. A PDMS mold with lines and spaces of 700 nm (350 nm deep) was placed onto the spin-coated wafer and allowed to deform the film at 25°C, then was heated to 80°C for 5 minutes to form the grating pattern in the chitosan. After removal of the mold, an additional baking step at 80°C for 5 minutes was

used to drive out the plasticizer. Using this process, linewidths of 280 nm with step heights of 12 nm were achieved [27]. For the 2:1 loading ratio, step heights of 110 nm were achieved following nanoimprint lithography.

Features produced using this technique are significantly shallower than the features on the mold, and is attributed to the thickness of the films being insufficient to fill the mold trenches completely. Achieved aspect ratios are significantly smaller than those produced with the mold.

2.9 Solution Preparation

Chitosan from crab shells (Sigma-Aldrich, St. Louis, MO) of low and medium molecular weights was used for this research. Chitosan used in this work had a degree of acetylation of less than 15%. A degree of acetylation of less than 50% is characteristic of chitosan while a degree of acetylation greater than 50% is characteristic of chitin. Low molecular weight chitosan has a molecular weight of 50-190 kDa while medium molecular weight chitosan has a molecular weight of 190-310 kDa. Chitosan solutions were prepared by dissolving chitosan in glacial acetic acid (Fischer Scientific) which was diluted with DI water to between 5 and 30%. Chitosan concentrations ranged from 0.66% w/v to 4% w/v. The solution was mixed and vacuum filtered to remove any remaining particles such as crab

shell. Dissolution was found to occur more quickly while heating at 40°C during mixing.

2.9.1 Relationship between viscosity and molecular weight

Molecular weight has been related to the viscosity of solution according to the Mark-Houwink equation. The coefficients for chitosan have been experimentally determined and defined as [22]:

$$\eta = KM^{\alpha} = 1.81 \times 10^{-3} M^{0.93} \tag{2.1}$$

where η is the viscosity, K is a constant, M is the molecular weight, and α is a scalar related to polymer stiffness.

The viscosity (and thus the molecular weight) has implications for spin-coating as the viscosity directly affects the thickness of the deposited film. It is important to note that processing conditions can have a significant impact on the molecular weight [22].

2.10 Chitosan Photolithography

Photolithography was investigated as a means to produce high resolution microscale chitosan features in a batch fabrication process. As a biocompatible

material that can be deposited onto a silicon substrate, chitosan allows the creation of microdevices with built-in biological interfaces suitable for a variety of sensing applications. The optical lithography process allows the introduction of the biopolymer chitosan into microfabrication process sequences and may serve as a seed layer for protein engineering.

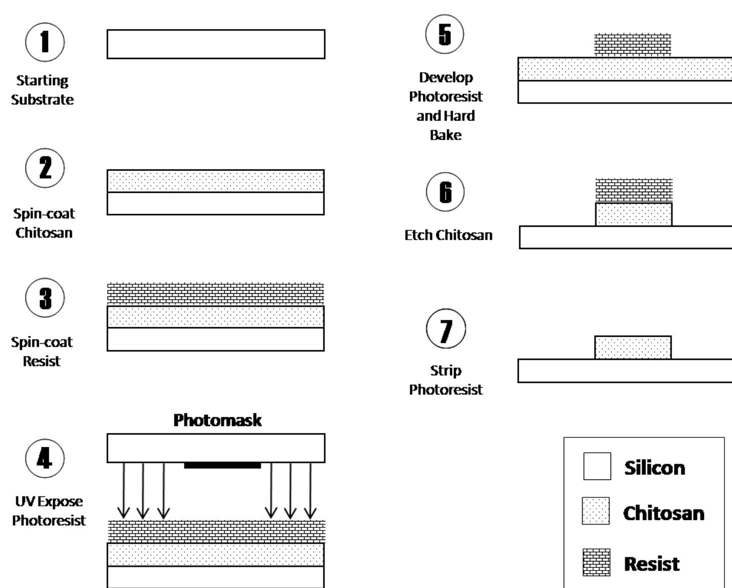

Figure 2.1: Schematic diagram of chitosan photolithography process.

Spin-casting was used to deposit chitosan thin films on a silicon substrate. 4 to 6 mL of chitosan solution (chitosan in acetic acid) was dispensed on a Si wafer and spun at 1,000 - 4,500 rpm for 30 seconds to 3 minutes. After spin-coating the solution, the solvent was air dried or evaporated at 80C to 120C at atmospheric pressure, leaving behind a thin-film of chitosan on the silicon

substrate. Film thicknesses ranging from 150 nm to over 1 m were achieved using this process. Figure 2.2 shows an SEM cross section of an approximately 1.5 m thick chitosan thin film on a silicon substrate. Film color was observed to vary with film thickness [34]. Fourier transform infrared spectroscopy and fluorescent microscopy were used to verify the film was chitosan.

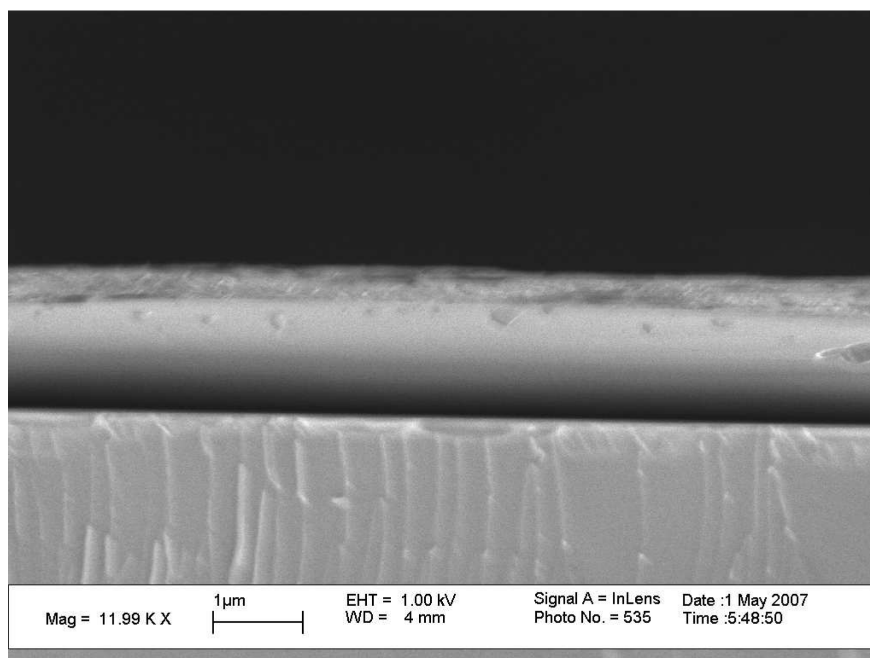

Figure 2.2: SEM showing chitosan layer deposited onto silicon substrate by spin-casting.

Standard photoresist exposure and development techniques were used to transfer a mask pattern to the wafer. OCG 825 G-line and OiR 10i I-line positive photoresists were used for chitosan photolithographic patterning. A soft bake at 90°C for 60 seconds was performed following resist deposition. Exposure was performed

using a Karl Suss MA6 Mask Aligner contact printer with exposure intensity of 18 - 20 mW/cm^2. The MA6 is capable of transferring features down to 2 μm. Exposure times were varied based on the lamp intensity, thickness of chitosan and photoresist, type of mask (chrome/emulsion on glass or photoplot) and were generally between 2 and 12 seconds. OCG 825 photoresist was developed with 2:1 OCG 934 photoresist developer, and OiR 10i photoresist was developed with OPD 4262 photoresist developer. After development, wafers were hard baked at 120°C for 30 minutes to stabilize the resist prior to etching. To improve selectivity of the resist, an M150PC Fusion Photostabilizer System may be used in place of the hard bake step. Following the hard bake, a descum may be performed in 50 W oxygen plasma for 1 minute. Although the descum will slightly etch the chitosan, the etch time is short and therefore removal of chitosan is minimal.

Overexposure of the photoresist resulted in chitosan coming into contact with the resist developer, which was observed to lead to cracking of the exposed film. The developer was also observed to cause cracking of chitosan beneath the remaining photoresist, implying that the developer was absorbed into the chitosan layer. To overcome this problem, a layer of HMDS was applied to the chitosan thin-film prior to deposition of photoresist. Assis *et al.* found that HMDS created a hydrophobic surface that prevented water permeability without causing a substantial change in O_2 or CO_2 permeability [35]. Lei *et al.* encountered a

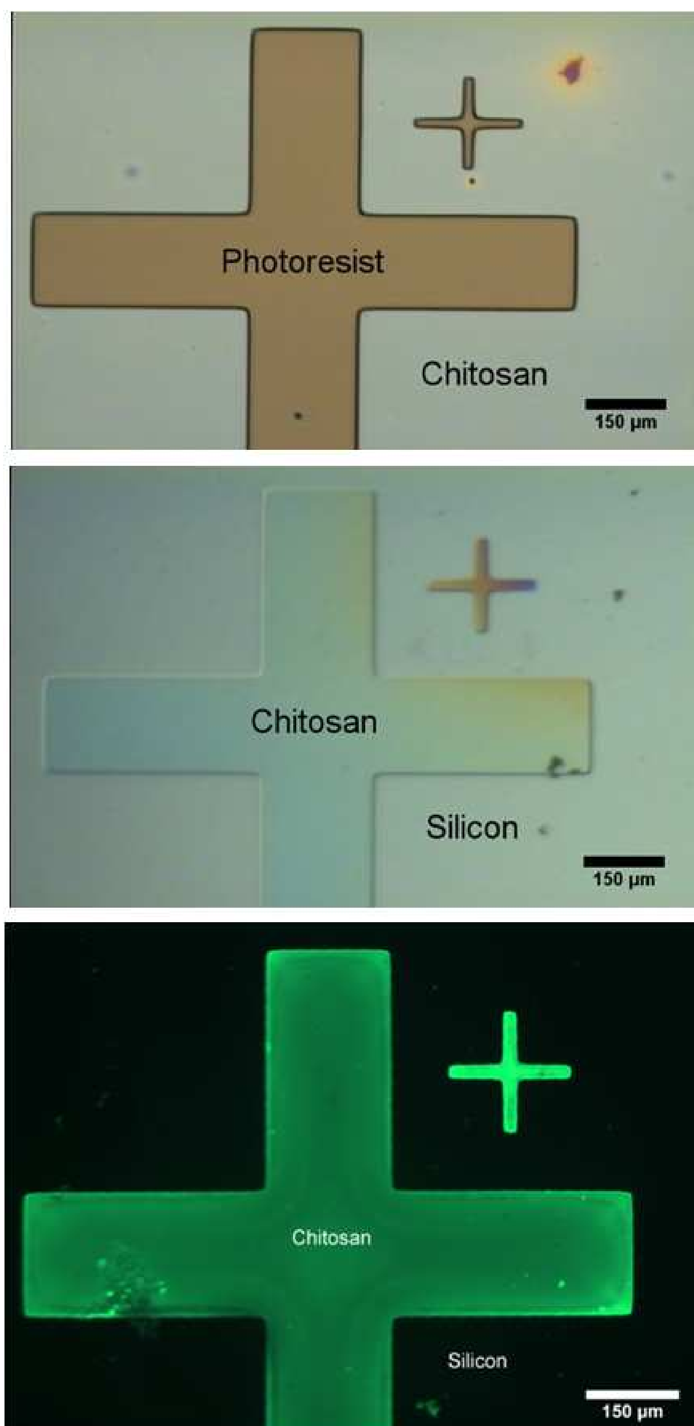

Figure 2.3: Chitosan photolithography process a) following photoresist development b) following resist strip c) following conjugation with fluorescein-conjugated chitin binding probe (protein attachment).

similar problem in photolithographic patterning of hydrogels; their solution was to slightly underexpose the photoresist to prevent contact with the water-based developer [36].

Sionkowska *et al.* investigated the effect of UV irradiation on the chitosan film surface [37]. They examined the effect of both a KrF excimer laser and the mercury UV lamp (λ=254 nm). The mercury UV lamp is similar to that used in this work for exposure of the resist during photolithography. The intensity of the mercury arc lamp used in their setup was 0.263 J/cm^{2}min [37], or equivalently, 4.383 W/cm^2. UV irradiation was found to decrease the contact angle when using diiodomethane, formamide, and glycerol, perhaps through a photooxidative mechanism [37]. Neither degree of acetylation nor surface morphology was observed to change following UV irradiation [37].

2.10.1 Surface roughness

The surface roughness of chitosan films deposited by spin-casting was investigated using atomic force microscopy. Square sections of sizes ranging from 0.2 to 10 μm on a side were scanned with the AFM probe tip, and the RMS roughness and z-axis range were computed.

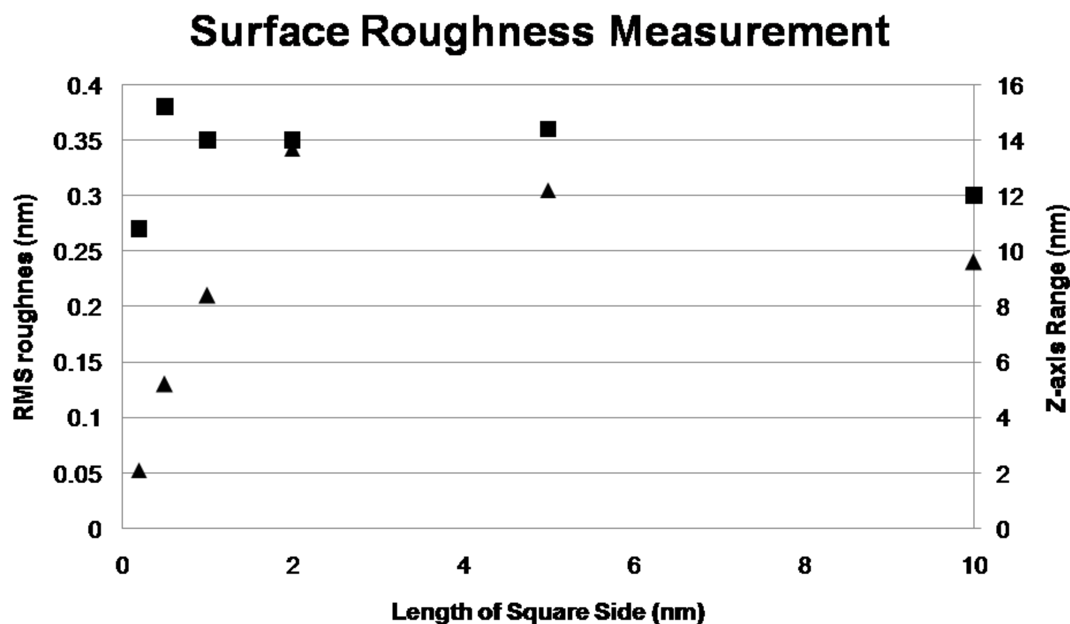

Figure 2.4: Surface roughness results obtained using atomic force microscopy. RMS roughness (square feature) and Z-axis range (triangle feature) is plotted as a function of length of one side of the square region.

2.11 Etching

We have explored both wet (using acetic acid) and dry (using O_2 plasma) etching of chitosan. Dry etching offers several advantages over wet etching, including high directionality, fewer toxic byproducts, and improved critical dimension control [18]. However, wet etching offers improved selectivity compared to dry etching.

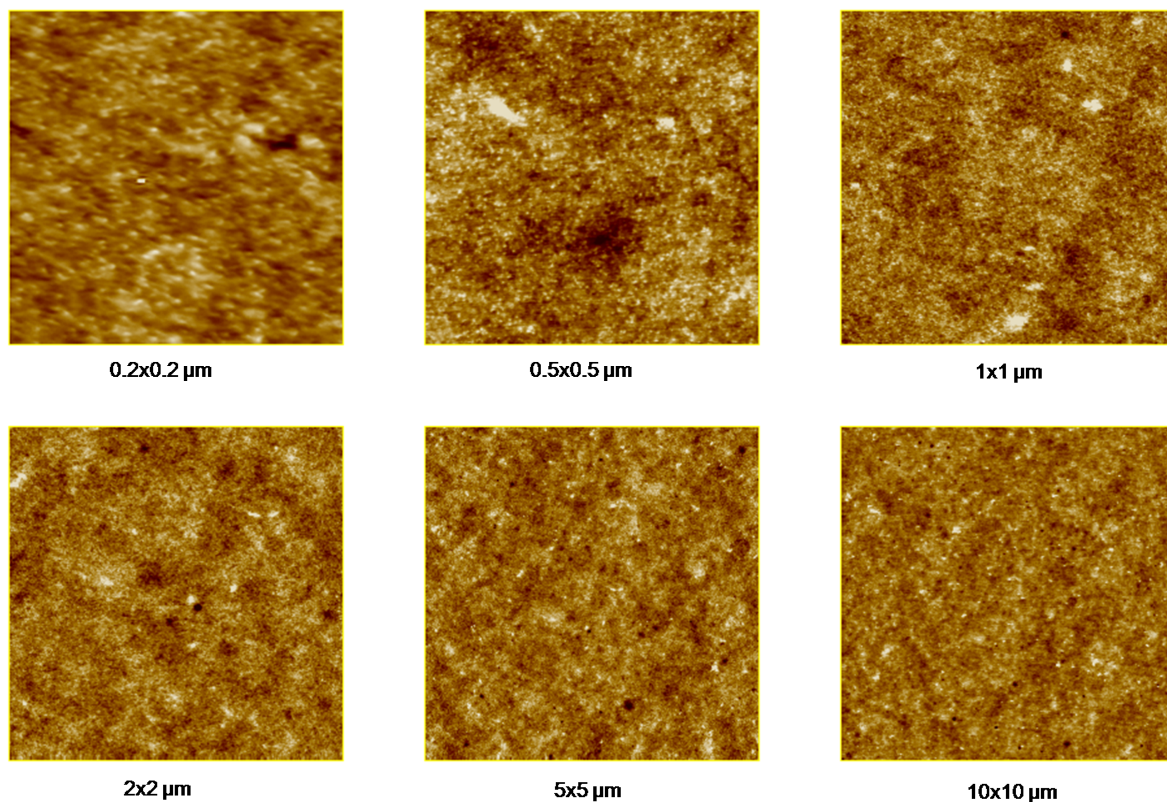

Figure 2.5: Surface topography of spin-coated chitosan film measured using atomic force microscopy. a) 0.2 x 0.2 μm square b) 0.5 x 0.5 μm square c) 1 x 1 μm square d) 5 x 5 μm square e) 10 x 10 μm square. AFM measurements performed by Dr. Álvaro San Paulo.

2.11.1 Wet Etching

Acetic acid was investigated as a wet etchant to remove exposed chitosan regions. Previously, Fernandes *et al.* observed that the pH responsive solubility of chitosan allows structures to be disassembled with a mild acid treatment [38]. Solution pH of ∼5.5 is sufficient to remove chitosan by dissolution. Because dissolution is pH dependent, there likely exist additional solvents such as lactic or citric

acid that may function as chitosan wet etchants. Photoresists such as OCG 825 dissolve in alkaline solutions, and were observed not not be etched by acetic acid. However, high concentrations of acid were found to destroy patterned photoresist features, which we attribute to a lift-off mechanism. The use of acetic acid for wet etching differs from its use in the spin-casting procedure in that the spin-cast solution contains a relatively large amount of chitosan whereas the wet etch initially contains no chitosan and only accumulates chitosan as the etch proceeds. Etch baths should have sufficient volume so as to maintain a low concentration of chitosan in the etch bath and to prevent the casting of chitosan upon removal from the etch. Concentrations of 2 - 2.5% v/v acetic acid may be used to wash away exposed chitosan regions. Low concentrations of acid are sufficient (so long as the pH is maintained at ~5.5) to remove chitosan from the wafer surface. Removal of exposed chitosan using acetic acid is shown in Figure 2.6.

Following wet etching, the wafer is removed from the etch bath, rinsed with DI water, and allowed to air dry or dried with a N_2 gun. Wet etching times should be restricted to less than 30 minutes to prevent damage to the patterned photoresist.

2.11.2 Dry Etching

Oxygen plasma, which is commonly used in microelectronics processing to etch organics such as photoresist, was found to be a suitable dry etchant of chitosan.

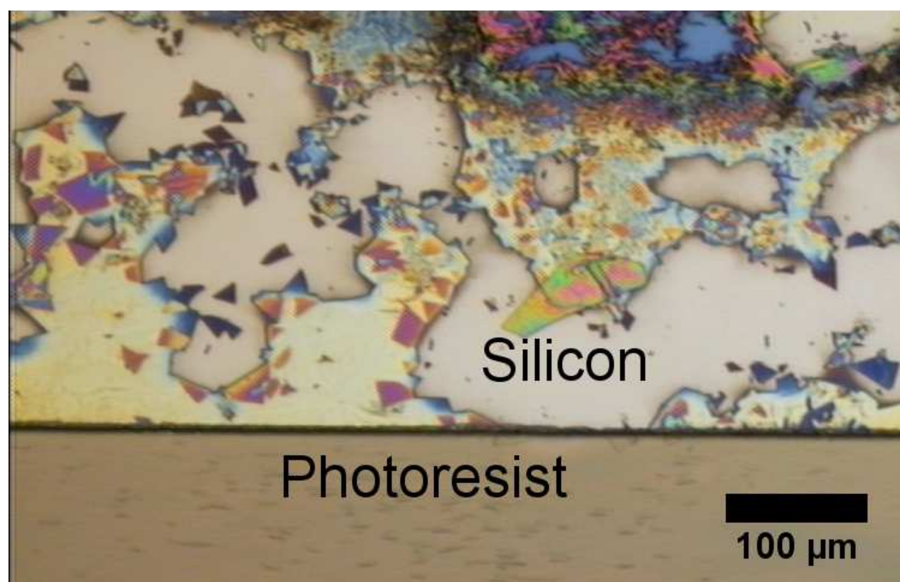

Figure 2.6: Wet etching of chitosan using acetic acid.

Etching was performed in 1 minute increments. Figure 2.7 shows micrographs of cantilever features (of varying widths and lengths) after 7 and 8 minutes of O_2 plasma etching. The exposed chitosan is completely cleared after 8 minutes of etching.

Chitosan etch rate was determined using ellipsometry and surface profilometry. Figure 2.9 shows chitosan and photoresist film thicknesses as a function of etch time. Data were obtained with an ellipsometer from an unpatterned chitosan thin film with initial thickness of approximately 810 nm. Using the ellipsometer, the chitosan etch was found to be linear with time (r^2 = 0.996) with a rate of approximately 244 nm/min for an etch selectivity (chitosan to photoresist) of

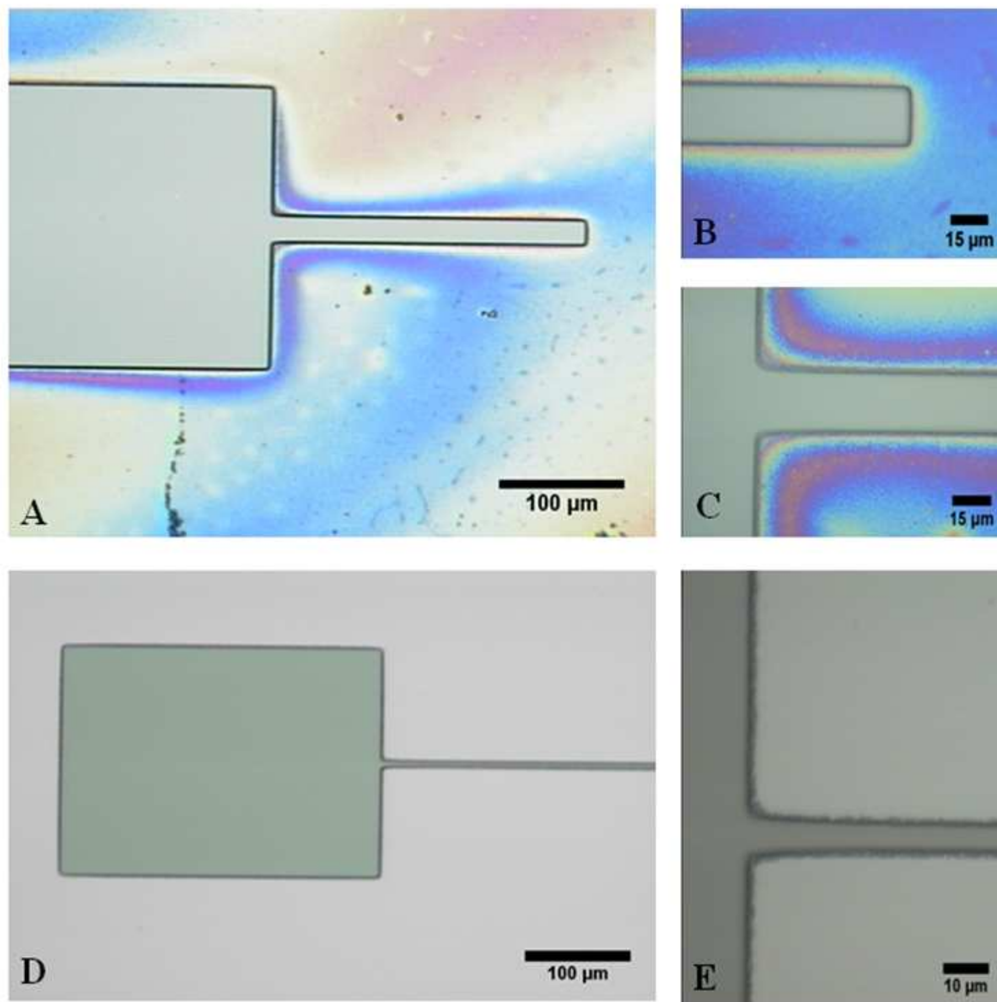

Figure 2.7: Dry etching of chitosan using oxygen plasma. Subfigures a-c show the chitosan film still partially present (blue area) after 7 minutes of etching, while subfigures d-e show the chitosan fully removed after 8 minutes of etching.

2.21:1. The etch rate is sufficiently fast to allow processing in reasonable times while still allowing control over final layer thicknesses.

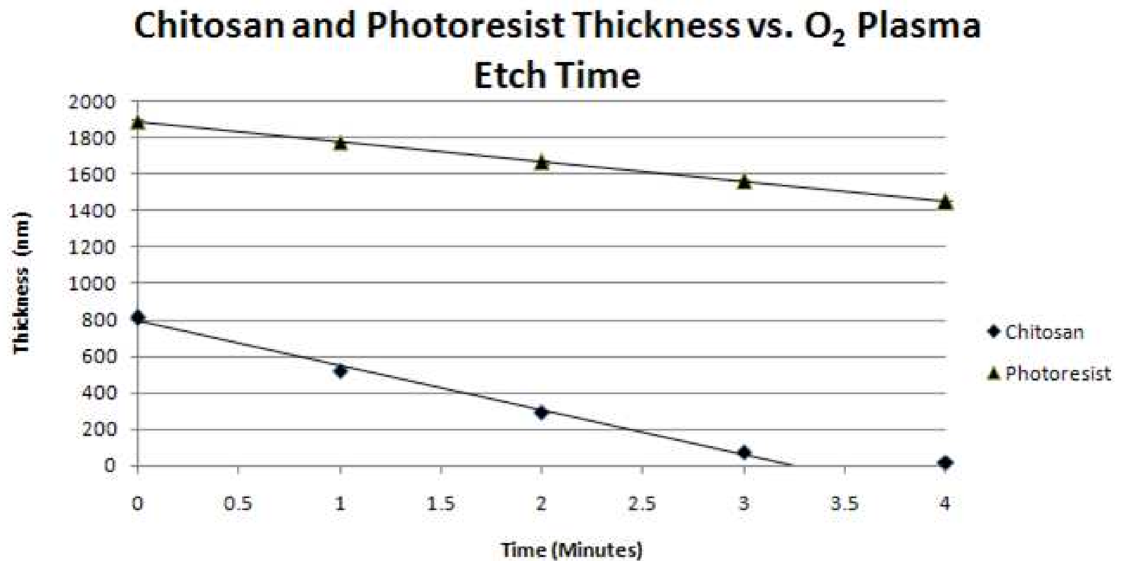

Figure 2.8: Oxygen plasma etch rate.

Surface profilometry using the photoresist-chitosan step height was also used to determine the etch rate for samples with patterned photoresist; the chitosan etch rate was found to be approximately 210 nm/minute for an etch selectivity of 1.37:1. Step height measurements were obtained using a KLA-Tencor Alpha-Step IQ surface profiler. Measuring step height profiles as a function of etch time allows the determination of etch rate. The step height of patterned G-line photoresist on silicon was measured as a function of time after O_2 plasma etching to determine the photoresist etch rate. Measuring the step height of a chitosan-photoresist

layer over time and subtracting out the amount of photoresist etched allows the etch rate of chitosan to be determined. The chitosan etch rate $\dot{E}_{chitosan}$ may be obtained using the equation:

$$\dot{E}_{chitosan} = \frac{y_f - (y_i - \dot{E}_{photoresist}\Delta t)}{\Delta t} \tag{2.2}$$

where y_f is the step height after etching a time Δt, y_i is the step height prior to etching, and $\dot{E}_{photoresist}$ is the photoresist etch rate obtained from the slope of a step height versus time graph. Results obtained using ellipsometry and surface profilometry agree well with one another.

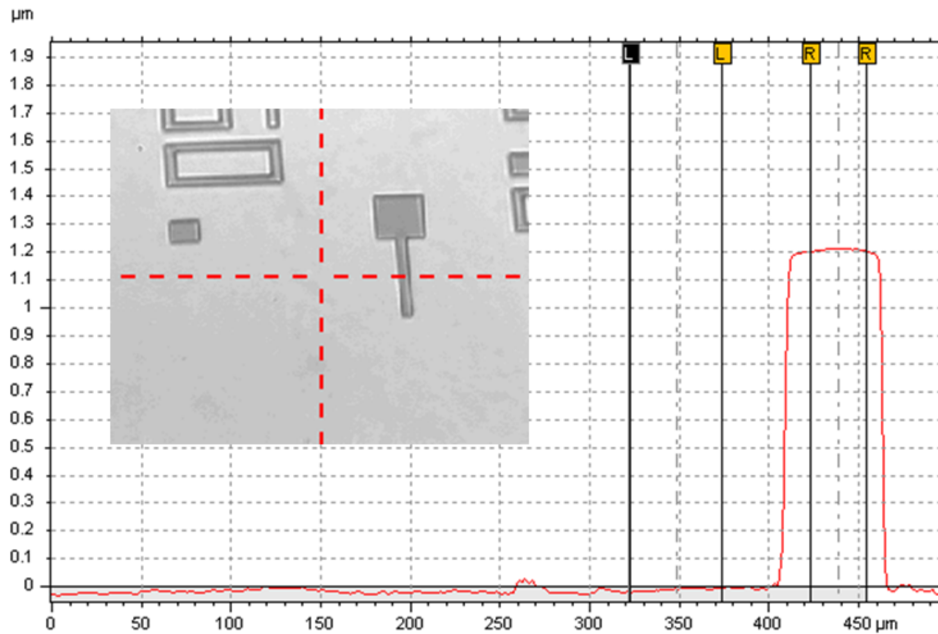

Figure 2.9: Step height defined in chitosan after 8 minutes of etching in oxygen plasma. Oxygen plasma etching produces sharp sidewall profiles.

Due to the low selectivity between chitosan and photoresist during dry oxygen plasma etching, it is important to ensure that the thickness of the deposited photoresist layer is sufficiently thick to withstand all chitosan etching steps. The photoresist thickness should be at least as thick as the chitosan layer in order to ensure preservation of the mask during dry etching. Chitosan film thicknesses were measured with an ellipsometer prior to photoresist spinning and after photoresist development; the film thicknesses were observed to be unchanged.

2.12 Resist Strip

The final step in the pattern transfer process is stripping the photoresist. Traditionally, photoresist stripping uses acetone or an alkaline solution such as PRS-3000 (J.T. Baker) heated to 75°C. In traditional semiconductor photolithography processes, PRS-3000 removes any remaining positive photoresist (with moderate baking) within 10-20 minutes depending on the thickness of photoresist used. We attempted to strip the patterned resist on a chitosan-coated wafer that was not etched by exposing the wafer to PRS-3000 for 5 minutes, 20 minutes, and 24 hours. We found that PRS-3000 does not strip photoresist when layered directly over a chitosan thin film. Similar results were found for patterned wafers that were etched with acetic acid. It is not clear why there is difficulty stripping pho-

toresist from unetched chitosan or from wafers where chitosan was etched with acetic acid. The failure of the resist to strip may be caused by fouling of the resist surface with a chitosan byproduct formed during the resist development process. However, we are unaware at present of any byproduct formed during resist development. Interestingly, we were able to strip the photoresist after 20 minutes in PRS-3000 when the wafer was first O_2 plasma etched prior to placement in the resist strip bath. The effect that the O_2 plasma has to facilitate photoresist stripping is unclear at present; however the O_2 plasma does remove the outermost surface of the photoresist. The O_2 plasma treatment was not long enough to remove the photoresist by itself. Figure 2.3a shows an alignment mark patterned in photoresist over a chitosan thin film prior to chitosan etching and Figure 2.3b shows the alignment mark patterned in chitosan on silicon following stripping of the photoresist with PRS-3000. Figure 2.3c demonstrates successful binding of protein to chitosan following the complete photolithography process. In addition, the post-lithography fluorescence micrograph provides evidence that photoresist does not foul the chitosan surface and that chitosan functional groups remain intact. Chitosan film thickness was measured following spin-coating and again following the resist strip using an ellipsometer. Film thickness was found to be consistent before and after the process, indicating that chitosan was not removed by the PRS-3000.

As an alternative to removal of photoresist with liquid stripper, we investigated resist ashing with O_2 plasma. A low RF power of 50 W was used in favor of a higher power such as 300 W because of the low etch selectivity of chitosan to photoresist. Although resist ashing is advantageous in that it may be performed simultaneously with the chitosan O_2 plasma etch, its drawback is that it requires careful timing (due to the low chitosan:photoresist selectivity) to prevent etching into the underlying chitosan layer. Lower RF power may be used to slow the etch rate. Because of the difficulty found in using a wet photoresist stripper such as PRS-3000 to remove photoresist from a chitosan thin film without first applying an O_2 plasma, it is recommended that one perform an exposure test using a bare Si wafer to minimize the risk of significantly underexposing or overexposing the resist.

2.13 Chitin Photolithography

In this processing approach, chitosan (deposited onto a wafer by spin-coating) is converted to chitin by reacetylation prior to the deposition of photoresist. The chitin lithography process is a modification of the chitosan photolithography process shown in Figure 2.3 where the spin-coated chitosan is soaked in a bath of 5% v/v acetic anhydride in methanol. OCG-825, positive, G-line photoresist pat-

terned over a chitin thin film which was then tagged with a fluorescently-labeled chitin binding probe is shown in Figure 2.10. A fluorescent label (rhodamine) was used to enhance contrast in the image.

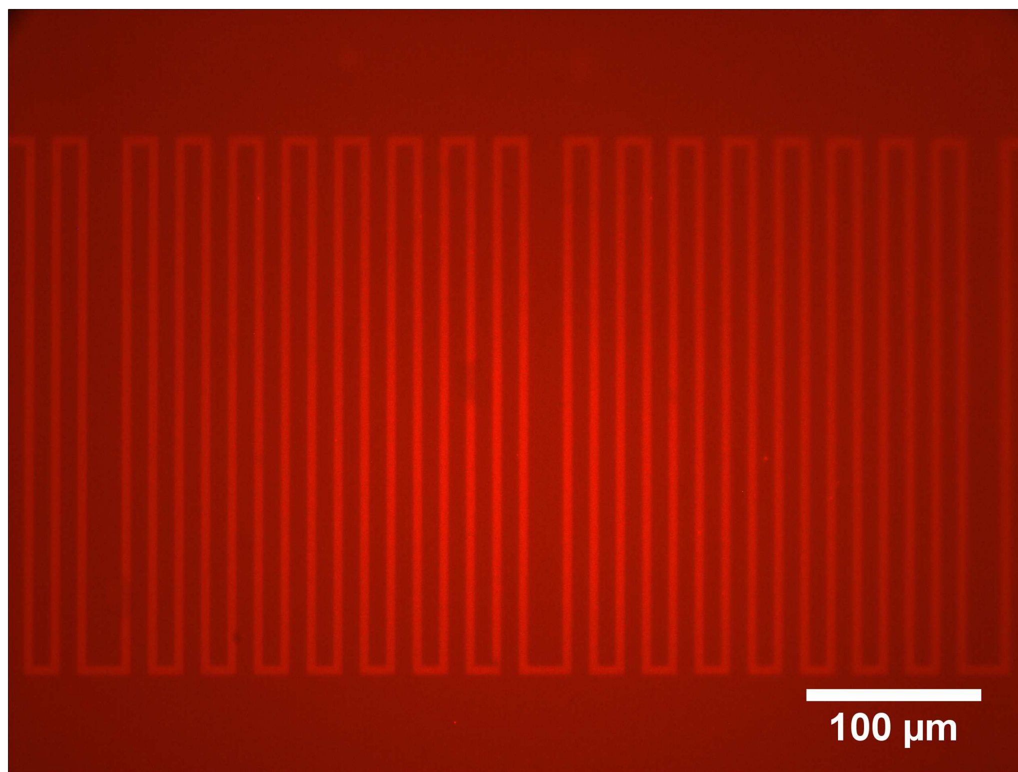

Figure 2.10: Chitin labeled with rhodamine-conjugated chitin binding probe (fluorescently-labeled protein) enhances contrast and demonstrates improved adhesion between resist and chitin with O_2 plasma surface roughening.

Patterning of chitin has several advantages over chitosan, particularly due to its increased chemical resistance and stability, due to the higher degree of acetylation of the polymer. The photoresist developer is not found to interact with chitin, as it does with chitosan. However, insufficient adhesion was found

between the chitin and photoresist layers. Adhesion between the photoresist and the hydrophobic chitin is a significant issue which requires the identification of an appropriate adhesion promoter.

Without an appropriate adhesion promoter, small photoresist features were found to detach and move during photoresist development. Hexamethyldisilazane (HMDS) was not found to improve the adhesion between the photoresist and the chitin, as seen in Figure 2.11. Therefore, it is important to identify an appropriate coupling agent between chitin and commonly used photoresists.

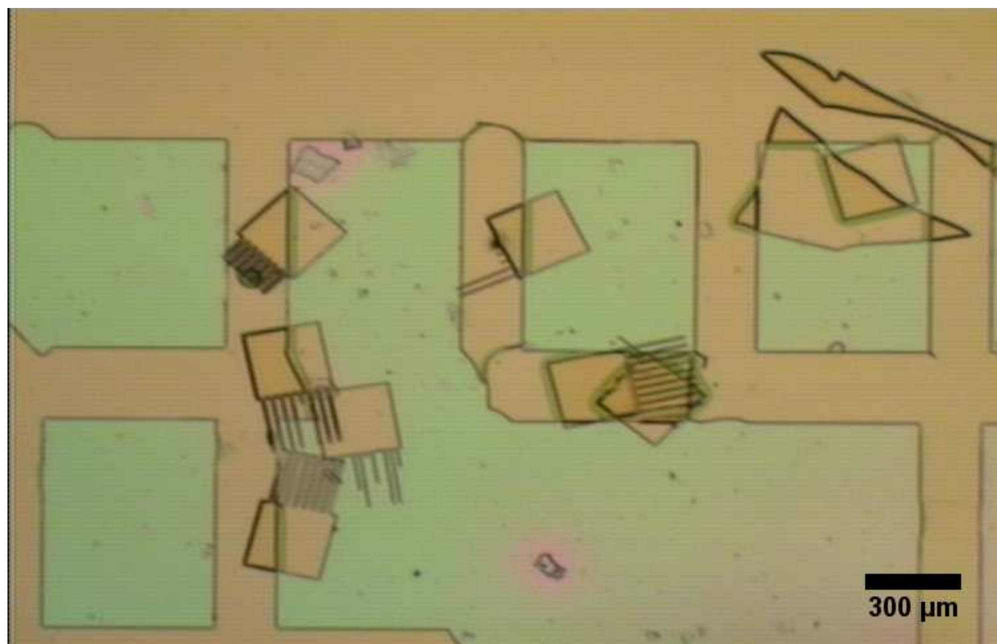

Figure 2.11: Hydrophobic chitin surface causes poor adhesion with photoresist.

However, rather than chemically modifying the surface properties with the deposition of a monolayer, physical modification of the surface may be used to

improve adhesion. A brief oxygen plasma etch of the chitin surface was performed with 50 W of 13.56 MHz RF power for several seconds prior to the deposition of photoresist. The use of oxygen plasma to roughen the surface was found to greatly improve the adhesion between the chitin and photoresist surface, as shown in Figure 2.12.

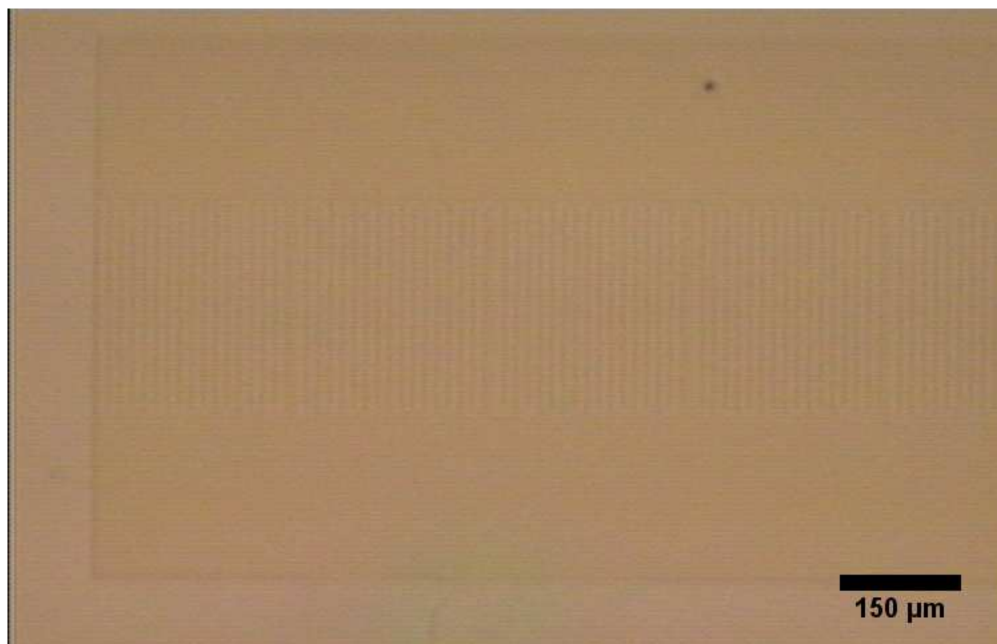

Figure 2.12: Brief oxygen plasma etch roughens the surface and improves adhesion.

2.14 Lift-off method for patterning chitosan

Traditionally, lift-off has been used in areas where direct patterning is not straightforward, for example, in patterning metals, such as platinum. The pat-

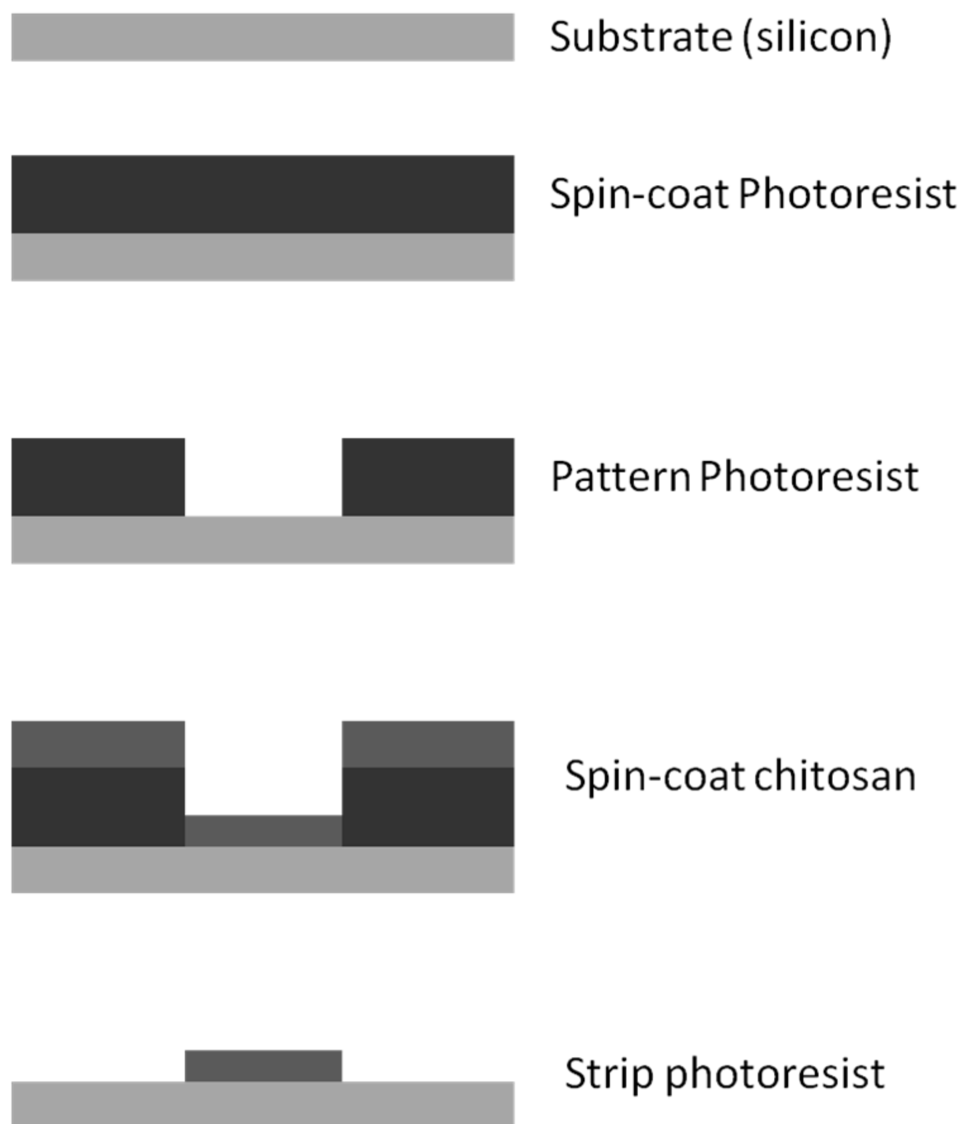

Figure 2.13: Schematic of lift-off process for patterning chitosan.

terned layer is typically much thinner than the lift-off layer. Polymer lift-off has previously been investigated for patterning lipids; however, that method required the use of optical lithography to first pattern a parylene layer and then

use mechanical peeling of the parylene film for the lift-off [39]. The fabrication process described here uses conventional photolithography and spin-coating of the polysaccharide to form defined regions of chitosan on a wafer with spatial control.

A schematic view of the lift-off process is shown in Figure 2.13. A 2 μm film of OCG-825 positive, G-line resist is spin-coated onto a silicon wafer (using hexamethyldisilazane as an adhesion promoter), exposed, and developed. The time of the hardbake may be substantially reduced or omitted. A descum is performed using 50 W O_2 plasma for 1 minute to remove any residual photoresist. A solution of chitosan dissolved in 10% acetic acid is then spin-coated over the patterned resist at 2,000 rpm for 1 minute and allowed to air dry. Lastly, the photoresist is removed using a photoresist stripper such as PRS-3000. It is important to not remove the wafer from the photoresist stripper prematurely as film particulates that dry on the wafer are difficult to remove. Because the chitosan is chemically resistant, it does not interact with the photoresist stripper. However, some diffusion of the photoresist / photoresist stripper byproduct is observed into the chitosan. This may be minimized by spin-coating the chitosan layer such that the thickness is much less than that of the photoresist layer. The thinner layer is believed to improve the lift-off by increasing the discontinuity of the layer around the patterned photoresist feature.

A pattern defined in photoresist prior to the deposition of chitosan is shown in Figure 2.14.

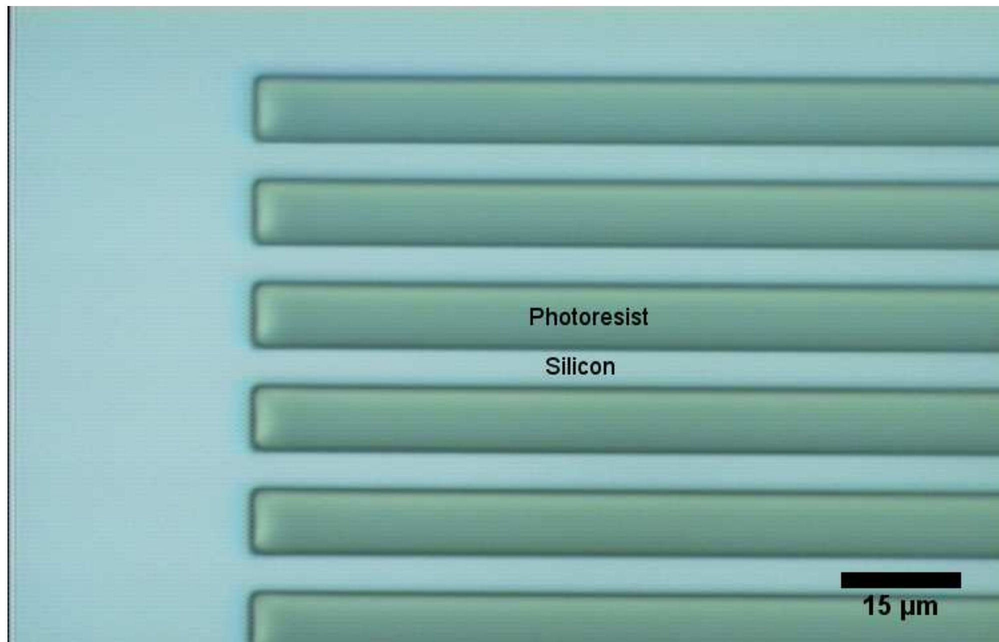

Figure 2.14: Patterned photoresist prior to chitosan deposition

Chitosan is then spin-coated over the photoresist pattern, as seen in Figure 2.15. To produce the chitosan pattern, the photoresist and the chitosan over it are removed using a photoresist stripper, leaving behind the chitosan that was coated directly over the exposed silicon. The final result is shown in Figure 2.16, and effectively produces the inverse of the pattern defined in the resist. This method has been used to produce chitosan line widths of less than 5 μm.

This technique offers a simple and facile method for integrating a chitosan thin film into a MEMS process. The process extends the lift-off technique beyond

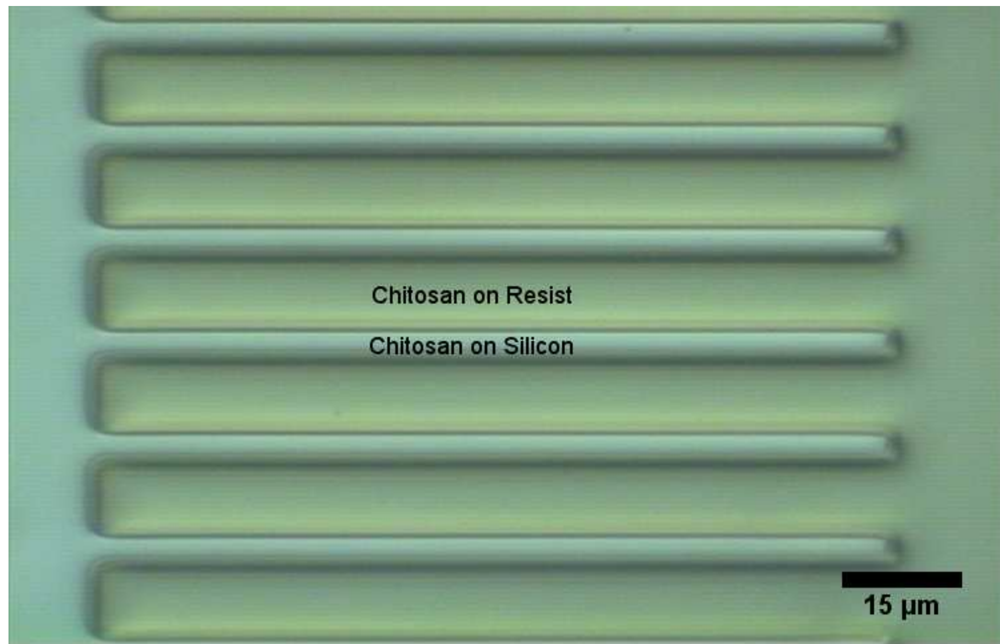

Figure 2.15: Chitosan spin-coated over patterned photoresist

Figure 2.16: Chitosan following lift-off of patterned photoresist using PRS-3000

metals and demonstrates the feasibility of lift-off for patterning polymers. Furthermore, the process removes the effect of the chitosan layer on the photoresist exposure time that would be present in conventional optical lithography. This method may be readily adapted as a means for patterning proteins using chitosan as a scaffold for bioconjugation, or as a template for cell-based systems in microfluidic devices.

2.15 Surface functionalization

One of the significant benefits of using chitosan as a microfabrication material or as a film in microelectromechanical systems is its ability to be functionalized using a variety of reaction chemistries. Although conventional semiconductor materials such as polysilicon, SiO_2 or Si_3N_4 may be etched, these materials have limited potential for chemical or surface modification or for use as a biologically active material. The surface wetting of chitosan may be modified through chemical reaction and allows the relative degree of hydrophilicity or hydrophobicity to be controlled. For example, chitosan may be converted between the salt and neutralized form. Chitosan films may serve as a site for bioconjugation with proteins and allow the formation of protein arrays on chip. Patterning need not be the end result but rather the initial template or site for chemical reaction or

protein detection on chip, potentially in highly arrayed formats that would allow high-throughput screening.

2.15.1 Fluorescent tagging and protein attachment

A fluorescently-labeled protein was bioconjugated to patterned chitosan/chitin features in order to demonstrate surface functionalization. Two different products from New England Biolabs (Ipswich, MA) were used to demonstrate the integrity and ability to functionalize the patterned chitosan/chitin surfaces. Fluorescein-conjugated chitin binding probe was used to functionalize patterned chitosan surfaces. Fluorescein-conjugated chitin binding probe is a recombinant fusion protein with a 5 kDa chitin-binding domain from *Bacillus circulans* WL-12 fused to maltose-binding protein from *E. coli* and labeled with fluorescein isothiocyanate (FITC). Rhodamine-conjugated chitin-binding probe was used to functionalize patterned chitin surfaces. Rhodamine-conjugated chitin binding probe uses the same recombinant fusion protein as the fluorescein-conjugated chitin binding probe but is labeled with tetramethylrhodamine isothiocyanate (TRITC). Both probes have a molecular weight of 48 kDa according to the manufacturer's specification.

2.15.2 Alternating microfabrication and nanoengineering steps in process

In the vast majority of microfabrication processes, materials are deposited using a method such as chemical vapor deposition, the material is patterned using a process such as photolithography, and the unwanted material is removed using a technique such as etching. This is inherently a top-down process and generally this sequence of steps is repeated a number of times to produce an integrated circuit or MEMS device of interest.

The processes described in this chapter for depositing, patterning, and functionalizing chitosan and chitin demonstrate a paradigm shift whereby top-down semiconductor manufacturing processes are merged with bottom-up processes to achieve novel results. Chitosan serves as a microscale scaffold with a nanoscale molecular binding site that may be functionalized.

2.16 Chitin Microfabrication Uses Beyond Infrared Detection

Numerous applications, especially in biology, exist for the use of patterned chitosan and chitin surfaces. The presence of the primary amino group in chi-

tosan allows for functionalization and enables a wide range of surface chemistries. Such abilities are particularly useful in protein-engineering and biosensing, where proteins may be bioconjugated or immobilized in the chitosan scaffold and their incredible specificity may be used in a variety of ways as a diagnostic tool or for detection. Bioconjugation of a fluorescently-labeled recombinant protein specific to chitosan is shown in Figure 2.17. Patterns could be made compatible with the 96 and 384-well microtiter plates commonly used in high-throughput screening applications. Coupling substrates with patterned chitosan structures with liquid handling systems or ink-jet print setups would allow the creation of protein chips suitable for high-throughput screening.

The photolithography process described in this chapter enables the creation of chitosan scaffolds on the same order as the diameter of the cell. As a result, the chitosan photolithography process could enable uses in tissue engineering and cell-based assays. Chitosan scaffolds could be arranged in patterns to guide and direct cell growth. Tissue engineering applications could involve the use of stem cells, or be used with neural cells to guide the growth of axons to direct the wiring of networks.

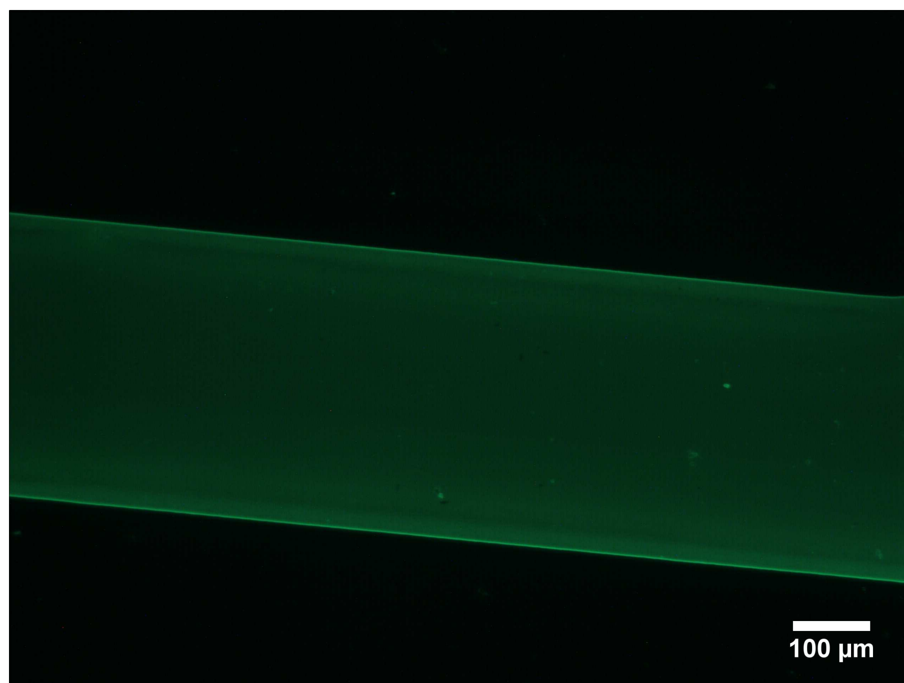

(a) Chitosan patterened as a single straight line.

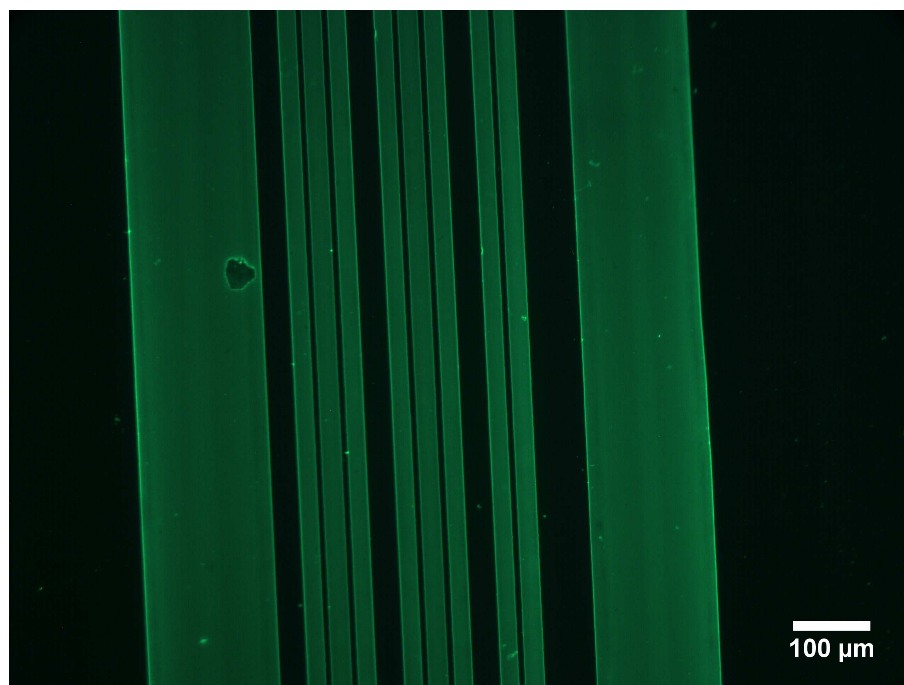

(b) Chitosan patterned as a series of parallel straight lines of varying widths.

Figure 2.17: Attachment of fluorescein-conjugated chitin binding probe to patterned chitosan surface.

Chapter 3

Properties of Chitosan and Chitin and Thin Film Characterization

3.1 Overview

In this chapter, characterization is performed on thin films of chitosan (salt form), chitosan (neutralized form), and chitin. All films were deposited by spin-casting and coated on a 4" silicon substrate. The salt form of chitosan is defined as a thin film of chitosan deposited by spin-casting that used evaporation or heating to remove the acetic acid solvent. The neutralized form of chitosan is defined as a thin film of chitosan deposited by spin-casting and treated with mild NaOH to remove any residual acid, and then dried by evaporation or heating. FTIR spectroscopy was used to determine the degree of acetylation of the films, laser profilometry was used to investigate the stress-temperature profile, and contact

angle measurements were used to investigate the relative hydrophilicity or hydrophobicity of the surface.

We have investigated the effect of temperature over a range from 20°C to 150°C on thin films of chitosan (salt form), chitosan (neutralized form), and chitin. Stress-temperature studies reveal a complex thermal response in chitosan films due to effects of moisture content and intermolecular bonding. Thermal annealing was found to modify the stress response and reduce the sensitivity of chitosan films (of the salt form) to environmental effects. Although chitin should have increased stability with respect to changes in relative humidity [26], the results described here show that chitin films obtained by reacetylation of chitosan still maintain a sensitivity to moisture. Chitosan films reacetylated to chitin were found to lack this moisture sensitivity during repeated thermal cycling. However, hysteresis in the measured stress-temperature profile is clearly evident in the first cycle and was also observed in subsequent testing after the film reached equilibrium. Chitosan films of the salt form that were neutralized with 0.1 M NaOH were also found to eliminate this moisture sensitivity during repeated cycling.

Therefore, the results of the experiments described in this chapter indicate that while both chitosan and chitin possess moisture sensitivities that may be modified by thermal means, the films will revert back to their native state when in the presence of moisture. Although heat may be used to reduce or eliminate

the effect of moisture or water absorption in chitosan and chitin thin films, these results demonstrate the importance of isolating the films from moisture for controlled film properties in packaged devices. The effect of moisture is particularly important for infrared sensing applications where the removal of moisture from the film opposes thermal expansion, a primary driving force in microcantilever-based infrared sensors. Vacuum packaging or hermetically sealing the device in an argon or nitrogen environment should eliminate the moisture effect in chitosan and chitin films. In Chapter 4, additional advantages of vacuum packaging for the performance of microcantilever-based infrared sensors will be described. Applications of chitosan and chitin in protein engineering, tissue engineering, and bio-sensing may be less sensitive to this moisture property of chitosan and actually may find the effect favorable by reducing the effect of thermal expansion in the system.

3.2 Glass transition temperature

The glass transition temperature is an important material property to consider in polymer systems because it represents the maximum processing temperature that may be utilized with the material still behaving as solid. Although Tan *et al.* [27] claims that chitosan does not have a glass transition temperature (im-

plying that the glass transition temperature is above the thermal degradation temperature), Dong *et al.* [40] was able to distinguish the glass transition temperature as well as other higher temperature relaxations using dynamic mechanical thermal analysis, differential scanning calorimetry, thermally simulated current spectroscopy and dilatometry. Using these techniques, Dong *et al.* found the glass transition temperature to be between 140-150°C [40]. The thermal degradation temperature of chitosan is approximately 220°C. The degree of acetylation was found to have no influence on the glass transition temperature [40].

Toffey *et al.* noted that chitosan films show an increase in T_g (glass transition temperature) with thermal treatment and also during thermal cycling, which is attributed to a removal of residual moisture, but that this rise in T_g was not due to removal of residual moisture for films of chitosonium acetate [41].

3.3 Degree of acetylation

The degree of acetylation is the characteristic which distinguishes chitosan from chitin. It is defined as the percentage of glucosamine units in the polymer binding an acetyl group at the primary amine. Chitosan has a low degree of acetylation (<50%) whereas chitin has a high degree of acetylation (>50%). The

degree of acetylation (or deacetylation) is rarely complete; typical values are 15-20% acetylation for chitosan and 80-85% acetylation for chitin.

The degree of acetylation (DA) has traditionally been extracted from the chitin/chitosan FTIR spectrograph by taking the ratio of two specific peaks. A review of the various methods used for determining the degree of acetylation from the FTIR spectrum can be found in Shiegmasa *et al.* [42]. For example, Murray *et al.* [26] used the ratio of the absorption of the acetyl group to the hydroxyl group with the equation:

$$DA = \frac{A_{1655}}{A_{3450}} \frac{100\%}{1.33} \tag{3.1}$$

where DA is the degree of acetylation, A_{1655} is the absorption at 1655 wavenumbers, and A_{3450} is the absorption at 3450 wavenumbers.

For example, using this method, the chitosan thin film seen in the FTIR of Figure 1.10 was found to have a degree of acetylation of 22.86%. The low degree of acetylation (<50%) confirms that the film is chitosan rather than chitin.

This method was also used to measure the degree of acetylation of a chitin film formed by reacetylating a chitosan film of the salt form, using the FTIR spectrograph of Figure 3.2. Using the ratio A_{1655}/A_{3450} produced a degree of acetylation of 159%. Although such a degree of acetylation is not physically

meaningful (degree of acetylation cannot exceed 100%), the high value reflects the high concentration of acetyl groups and may reflect the error in the model for high degrees of acetylation [42].

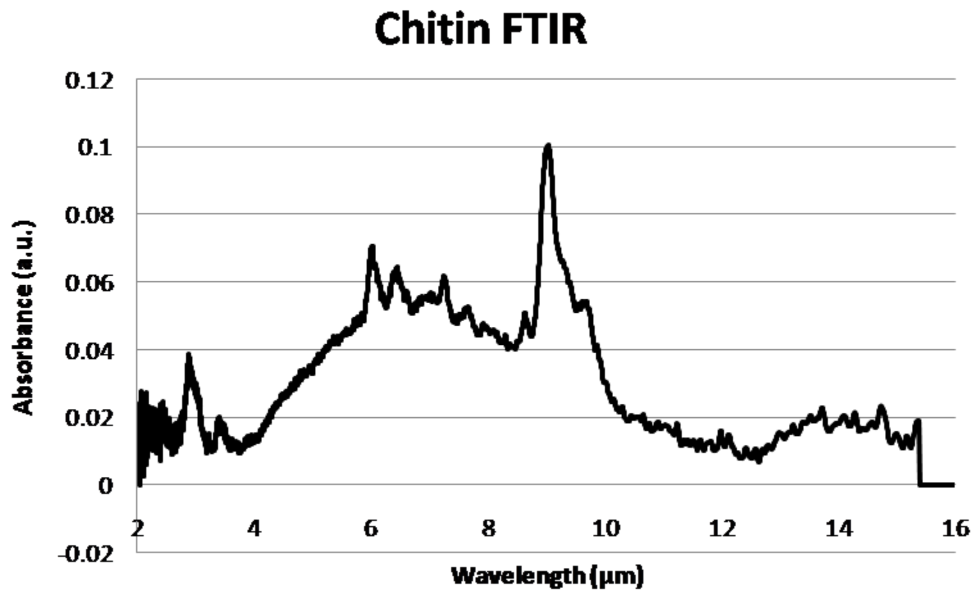

Figure 3.1: FTIR spectrograph of chitin thin film formed by reacetylation of chitosan to chitin (in microns).

3.4 Stress-Temperature Profile

Laser profilometry was used to measure the stress in the film as a function of temperature. Understanding the stress-temperature profile is important for the development of uncooled microcantilever-based infrared sensors because absorbed infrared radiation is converted to heat in the absorbing layer, and the resulting

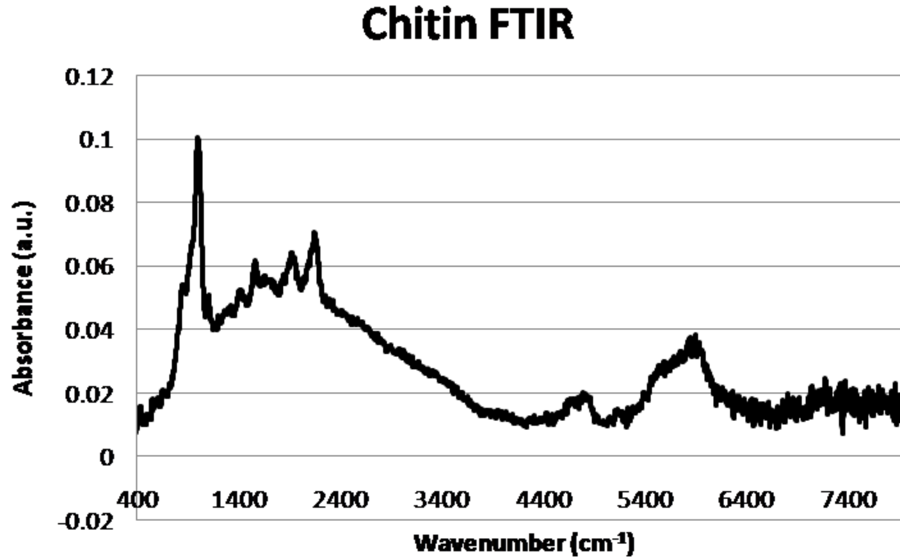

Figure 3.2: FTIR spectrograph of chitin thin film formed by reacetylation of chitosan to chitin (in wavenumbers).

change in temperature produces a mechanical change by altering the stress. Therefore, the stress-temperature profile is at the center of the transduction process in microcantilever-based infrared sensors. The laser profilometer (Tencor FLX-2320) measures the curvature of the wafer, which changes with the stress in the film. The Stoney equation relates the stress in the film to the radius of curvature of the wafer:

$$\sigma = \frac{E}{1-\nu}\frac{h^2}{6Rt} \tag{3.2}$$

where h is the thickness of the substrate, t is the thickness of the film, and R is the radius of curvature of the wafer. Varying the temperature of the wafer will alter its stress, which in turn affects the wafer radius of curvature. Thermal expansion will cause a linear change in stress with temperature over a subset of the temperature range, and the profile should be similar regardless of whether the wafer is heated or cooled. Other changes which could affect the stress in the film include changes in bonding, changes in crystallinity, cross-linking of the polymer, or a phase change.

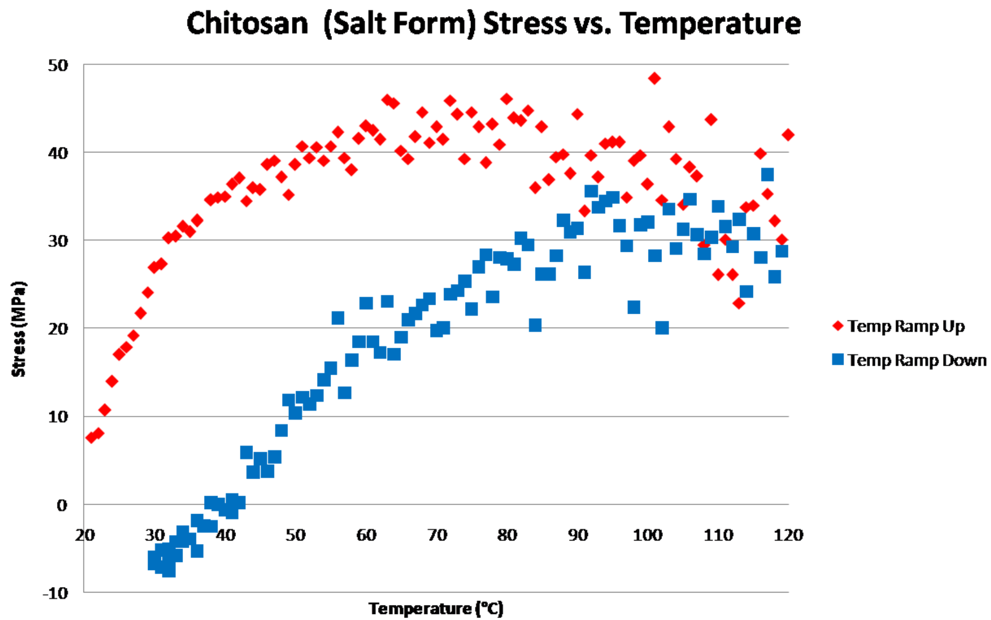

Figure 3.3: Stress as a function of temperature for a chitosan thin film (salt form)

3.5 Hysteresis

Hysteresis is observed in the stress versus temperature plot of a chitosan thin film on a silicon wafer. This may be the result of chitosan's affinity for binding water, which is related to its ability to function as a hydrogel. One method for verifying this proposed causality would be to replace the air in the laser profilometer chamber with nitrogen or argon and observe whether the hysteresis remains. Ramping the temperature up is believed to remove moisture from the film. This loss of moisture could explain the hysteresis observed in the stress vs. temperature curve. Another possible explanation is incomplete drying of the chitosan film following the deposition process (spin-coating from aqueous solution). This explanation is subsequently disproved in the course of this research.

The separation in the stress versus temperature plots that occurs between heating and cooling measurements may be attributed to the loss of water from the films and a corresponding thickness change. To investigate this hypothesis, the film thickness across multiple points on a chitosan acetate-coated wafer was measured immediately before and immediately after temperature cycling. Prior to thermal cycling, the film thickness was measured as 180 ± 11 nm and after we measured the film thickness to be 167 ± 12 nm, for an average loss in thickness of 7.1%.

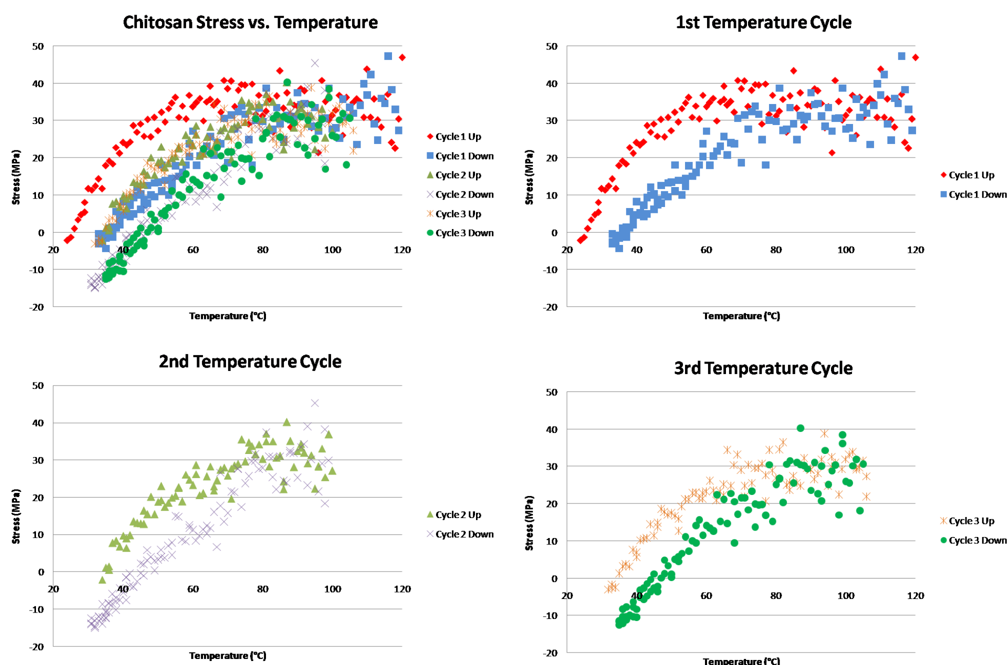

Figure 3.4: Effect of thermal cycling on chitosan film (salt form). Repeated cycling reduces the stress hysteresis observed in the film.

The film stress is inversely proportional to the thickness, and thus we expect a 7.6% increase in stress for a 7.1% reduction in film thickness. However, we observe a change in stress far greater than the 7.1% change that can be explained by a change in film thickness. The biaxial modulus is another component that is assumed constant in the Stoney equation, which may in fact have a temperature dependence.

3.6 Thermal Annealing of Chitosan Films

The effect of thermal annealing on the mechanical properties of chitosan and chitin thin films was investigated using laser profilometry. Thermal annealing at 150°C was found to eliminate the stress versus temperature hysteresis after prolonged heating, as shown in Figure 3.5. The 150°C anneal temperature is also near the chitosan glass transition temperature. Figure 3.5 shows the stress temperature profile after 1 hour, 24 hour, and 36 hours of annealing at 150°C. Although the measurement itself ramps from room temperature to 120°C and to some extent also serves as an anneal, the effect is probably negligible because of the lower temperatures (max 120°C) involved in the laser profilometry measurement. Though hysteresis is still observed after a 24 hour anneal, after 36 hours of annealing, the hysteresis is essentially eliminated. This observation is consistent with the conversion of chitosan to a "chitin-like" material as described by Murray and Dutcher [26].

In addition, the stress at room temperature was found to change directions from tensile to compressive as the length of the anneal increased.

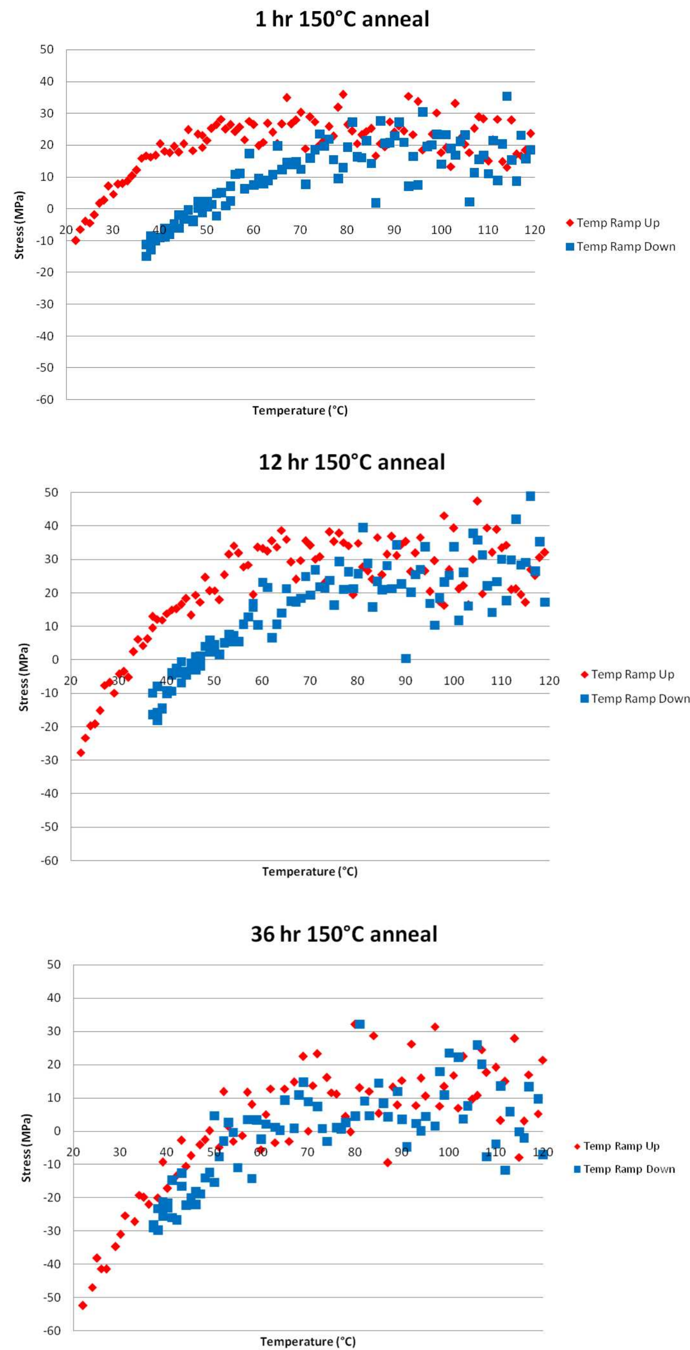

Figure 3.5: Effect of 150°C anneal on stress vs. temperature hysteresis

3.7 Conversion of chitosan to chitin by heating

One explanation for the change in stress versus temperature data for extended periods of heating is that heating may produce a change in chitosan to a "chitin-like" material. This explanation is supported by recent work by Murray and Dutcher [26] which found that heating to elevated temperature (between 150°C and 200°C) caused an irreversible decrease in film thickness, a minor increase in index of refraction, a reduction in water absorption, and an increase in acetylation as measured before and after heating using Fourier transform infrared spectroscopy [26]. In their work, chitosan films were spin-coated while controlling both the spin speed and the relative humidity.

3.8 Differences in stress-temperature profile

Interestingly, the temperature at which both the chitosan (salt form and neutralized form) film crosses from tensile to compressive (zero stress point) occurs at roughly 37-40°C, which incidentally is near human body temperature. The chitin film reaches the zero stress point at a temperature below the measured data range. Extrapolating from the stress-temperature profile of chitin, this point is approximately 20°C. The temperature at which this zero stress point occurs may be another method in addition to the measurement of degree of acetylation

to distinguish chitosan from chitin. The zero stress point near body temperature may be useful for applications such a controlled drug release, an area in which chitosan is already used commercially.

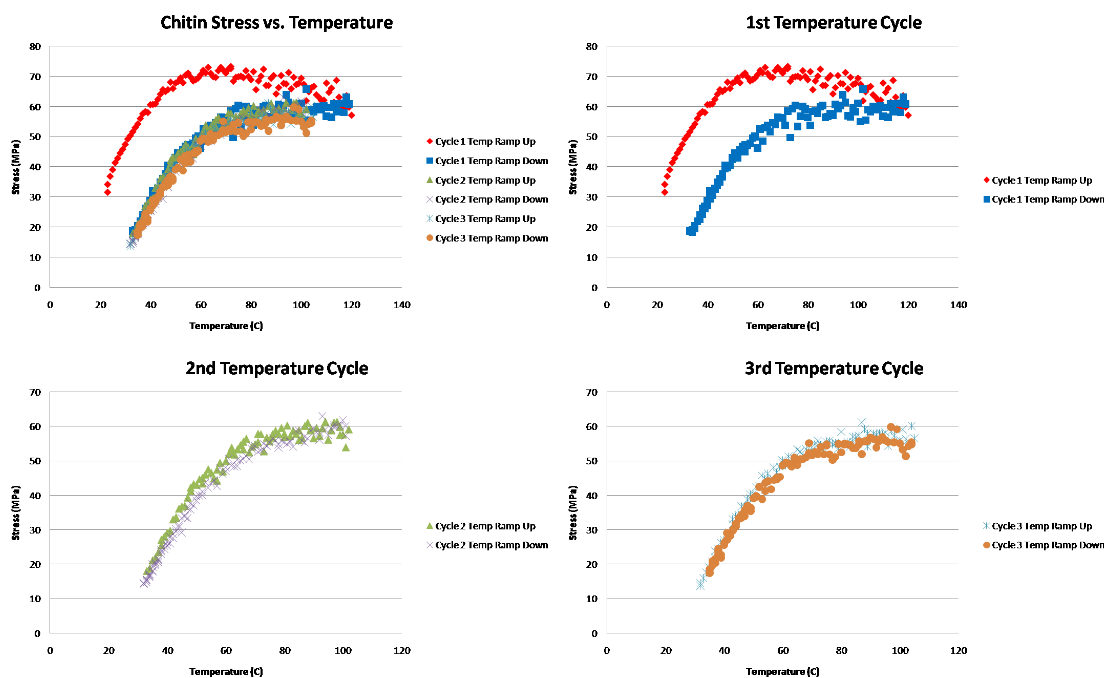

Figure 3.6: Effect of thermal cycling on chitin film. Chitin film was obtained using reacetylation process with chitosan (salt form) film.

It is important to determine whether the large gap in the stress-temperature profile that is observed in the first cycle of the chitosan (salt form), chitosan (neutralized) and chitin thin film stress-temperature profiles is due to incomplete drying of the film or the absorption of moisture from the environment. To eliminate incomplete drying as an explanation for the observed hysteresis in the stress-temperature profile, the following experiment was conducted. A chitosan

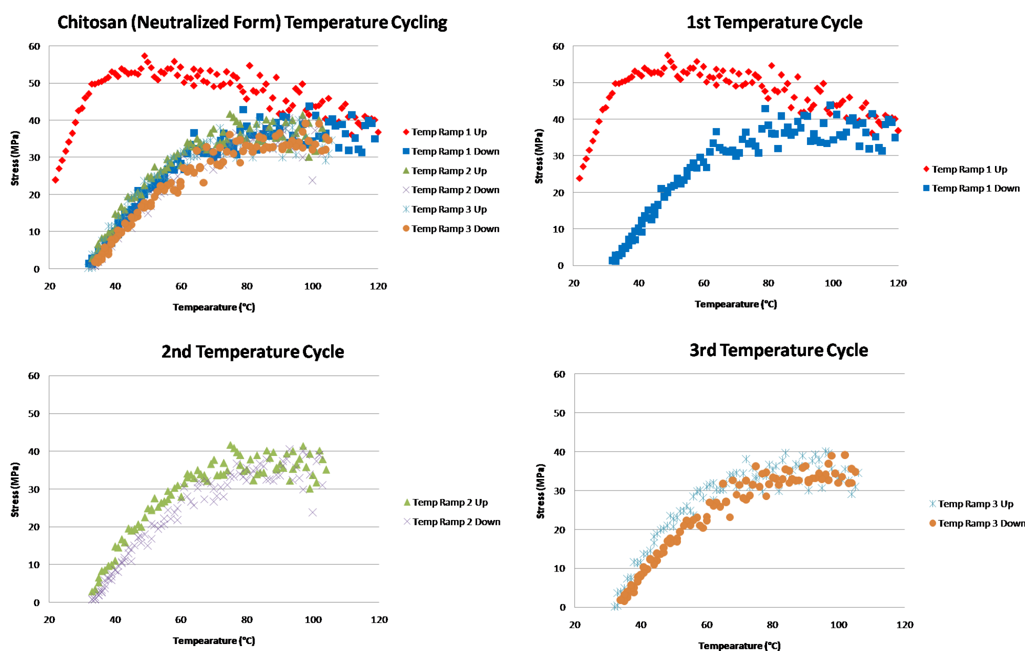

Figure 3.7: Effect of thermal cycling on chitosan film (neutralized form).

(salt form) film was spin-coated on a wafer and allowed to air dry overnight. Stress-temperature data was collected for three cycles. The first cycle ramped from 20°C to 120°C and back. The second and third cycle ramped from 20°C to 160°C. Due to limitations of the temperature control in the laser profilometry system, actual temperature achieved is approximately 140°C. After completion of the measurement, the wafer was stored in a wafer box for more than 12 hours and the experiment was repeated with two temperature cycles. Results are shown in Figure 3.8.

Incomplete drying was one possible explanation for the hysteresis observed in cycle 1 of the stress-temperature profile. However, once eliminated, this large hys-

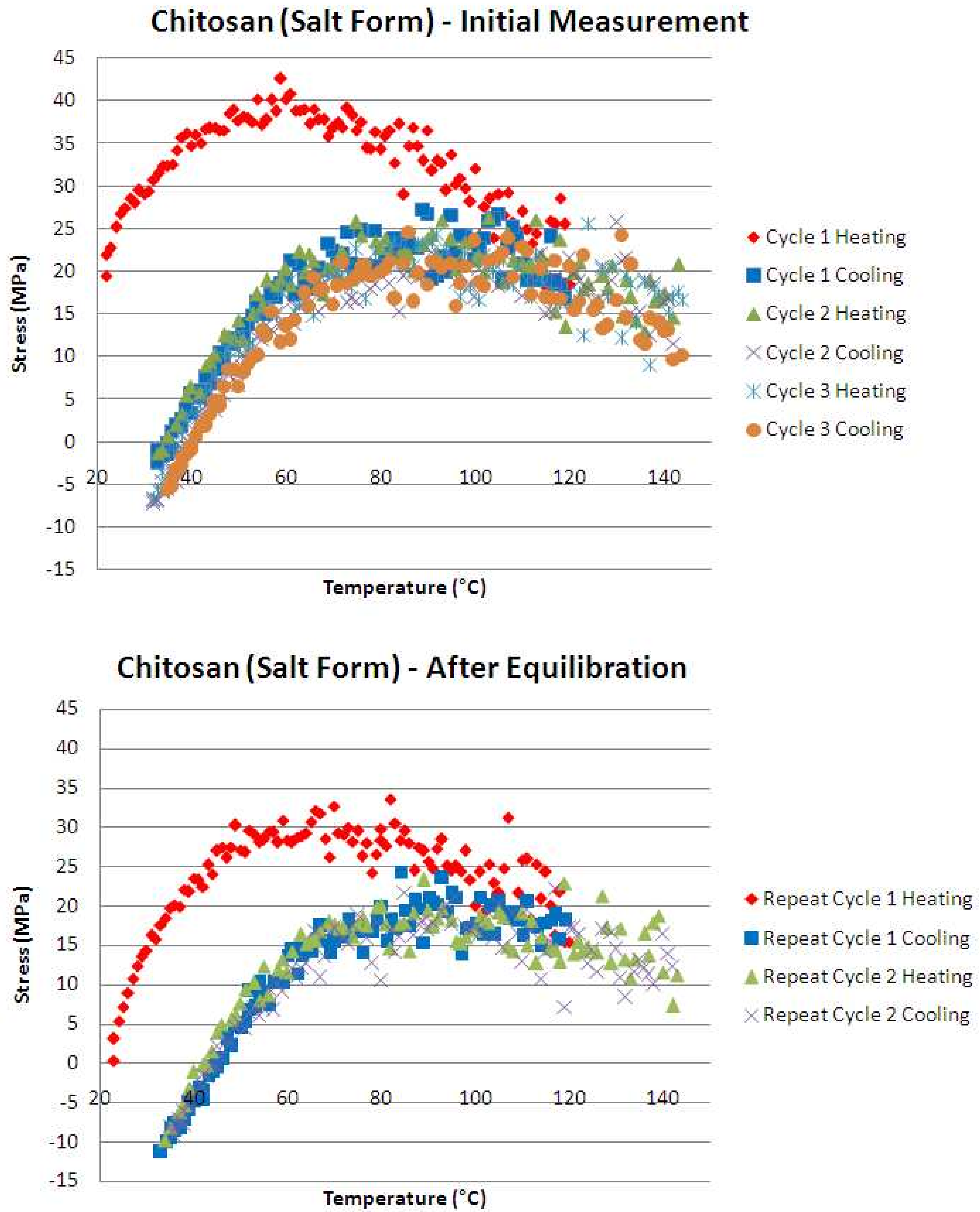

Figure 3.8: Incomplete drying not responsible for cycle 1 stress-temperature hysteresis.

teresis should not reappear if it is caused by incomplete drying of the film following deposition. The multiple heating cycles that take place during the measurement process function as a drying process and also removes moisture from the chitosan film. In cycle 3 the stress-temperature profile is largely eliminated due to the high temperature (approaching the glass transition temperature of chitosan) of the measurement process. After completing the stress-temperature profile measurement, the wafer was placed in a storage box and allowed to equilibrate to ambient conditions for more than 12 hours. The stress-temperature profile measurement was then repeated and the hysteresis in cycle 1 was found to reoccur. This indicates that incomplete drying is not responsible for the stress-temperature hysteresis and this may be due to the effect of moisture on the chitosan (salt form) film. Therefore it is important to control the moisture in chitosan-based devices where stress is involved in the sensing process. This may be accomplished by vacuum packaging or encapsulation in a nitrogen or argon atmosphere.

Similar results were obtained for chitin, as shown in Figure 3.9. Although heating appears to eliminate bound water from chitin more readily than for chitosan, there is clearly a moisture effect as seen in the first cycle even after equilibration. Therefore, it is important to consider the effect of fluctuations in the relative humidity on the stress in the films.

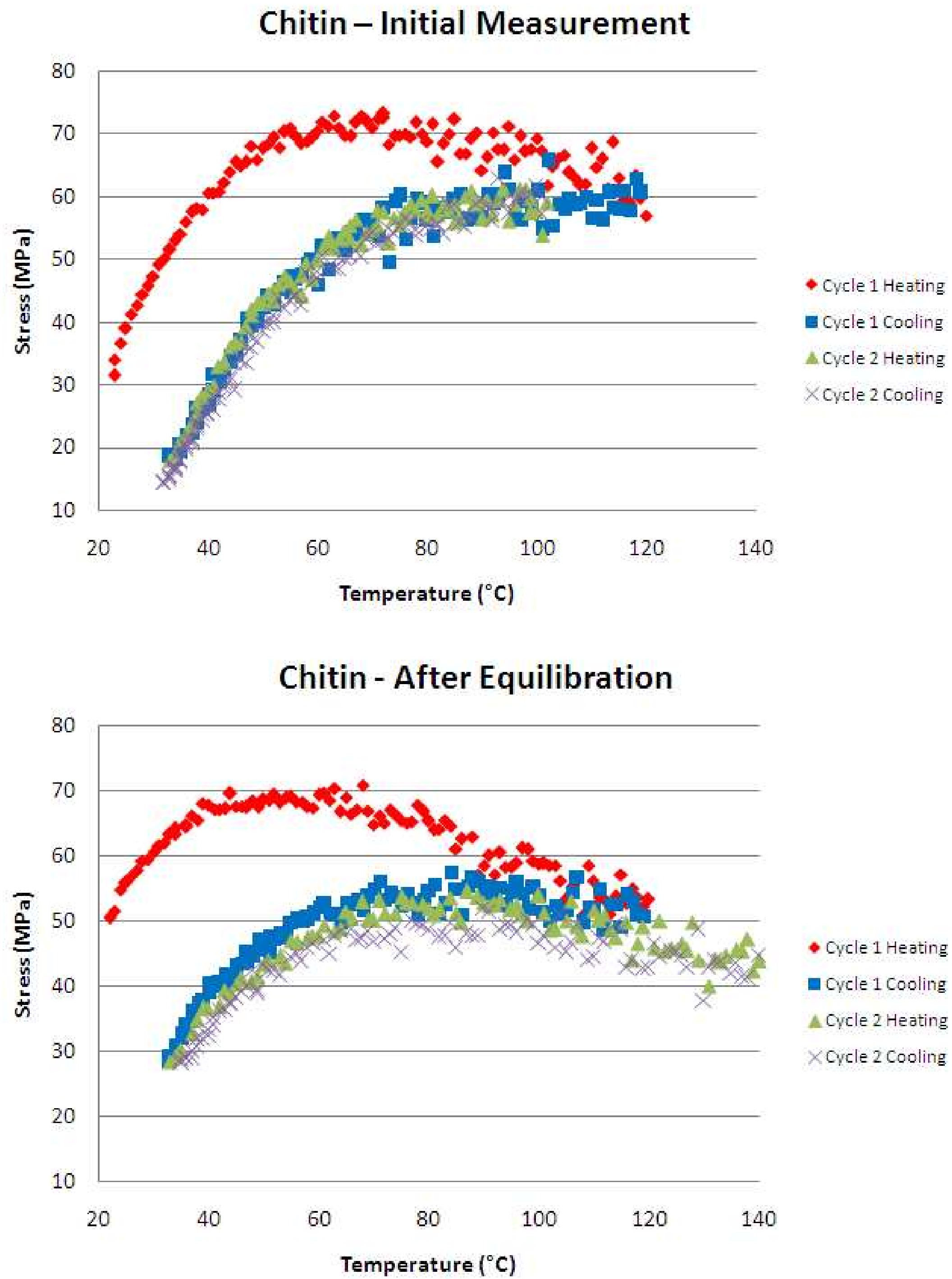

Figure 3.9: Chitin shows moisture absorption after equilibration.

The stress vs. temperature profile is the result of two opposing effects, thermal expansion and removal of moisture from the film. At high temperature, all moisture has been removed from the film and the change in stress that occurs is due purely to thermal expansion. Because the film is constrained onto the silicon substrate, thermal expansion produces a compressive stress in the film that opposes the thermal expansion. Thermal expansion has a linear effect on the stress. The stress vs. temperature profile can be considered a superposition of these thermal expansion and moisture effects. These can be modeled independently.

3.9 Thermal effect on bonding and crystallinity

Little change was observed in the FTIR spectrum between a film with no annealing and a film annealed for 24 hours at 120°C. Observed differences in the FTIR spectra for films with various lengths of annealing may be attributed to random variations typical for measurements using the machine and do not imply that any change in bonding is taking place.

Chitosan films of the salt form were found to be amorphous both as deposited and following thermal annealing [Breiby and Aasmundtveit, personal communication]. Acetate salts of chitosan were observed to be amorphous by Nunthanid et al. [43]. The observation that heating the film does not have a significant effect

on bonding or crystallinity gives further support to moisture being the dominant effect responsible for the observed hysteresis.

3.10 Coefficient of thermal expansion

The coefficient of thermal expansion represents the amount of mechanical deformation that results in a material due to a change in temperature. It may be defined as:

$$\alpha = \frac{\Delta L}{L \Delta T} \tag{3.3}$$

The coefficient of thermal expansion of polymers is generally high, making them strong candidates for use as materials in high CTE-mismatch cantilever bimorphs for infrared detection. The coefficient of thermal expansion may be measured experimentally using the stress-temperature profile obtained through laser profilometry using two different substrates. The CTE is related to the slope of the stress-temperature profile according to the relationship:

$$\frac{d\sigma}{dT} = \frac{E}{1-\nu}(\alpha_s - \alpha_f) \tag{3.4}$$

where α_s is the coefficient of thermal expansion of the substrate and α_f is the coefficient of thermal expansion of the film.

For example, the CTE of a polymer film may be determined by depositing the polymer on both silicon and quartz substrates and measuring the stress-temperature profile. The results are then used to simultaneously solve the equations for the biaxial modulus and for the coefficient of thermal expansion.

$$\frac{d\sigma}{dT}_{silicon} = \frac{E}{1-\nu}(\alpha_{silicon} - \alpha_f) \tag{3.5}$$

$$\frac{d\sigma}{dT}_{quartz} = \frac{E}{1-\nu}(\alpha_{quartz} - \alpha_f) \tag{3.6}$$

However, when applied to chitin and chitosan thin films, this technique fails due to the non-linearity of the stress-temperature profile. The removal of moisture from the film with heating confounds the results and acts to oppose the thermal expansion of the film.

The stress-temperature profile of chitin/chitosan thin films was compared with that obtained from OCG 825 G-line, positive photoresist. Stress-temperature data for OCG 825 positive resist coated on silicon and quartz wafers is shown in Figure 3.10. The thermal expansion coefficient of the photoresist was computed over the highly linear temperature region from 45°- 95°C. The determination of the

coefficient of thermal expansion is highly sensitive to the chosen values for the thermal expansion coefficient of silicon and quartz, and can vary from 50×10^{-6} to 300×10^{-6} due to this uncertainty. This range of values is consistent with the high thermal expansion coefficients typical of polymer materials.

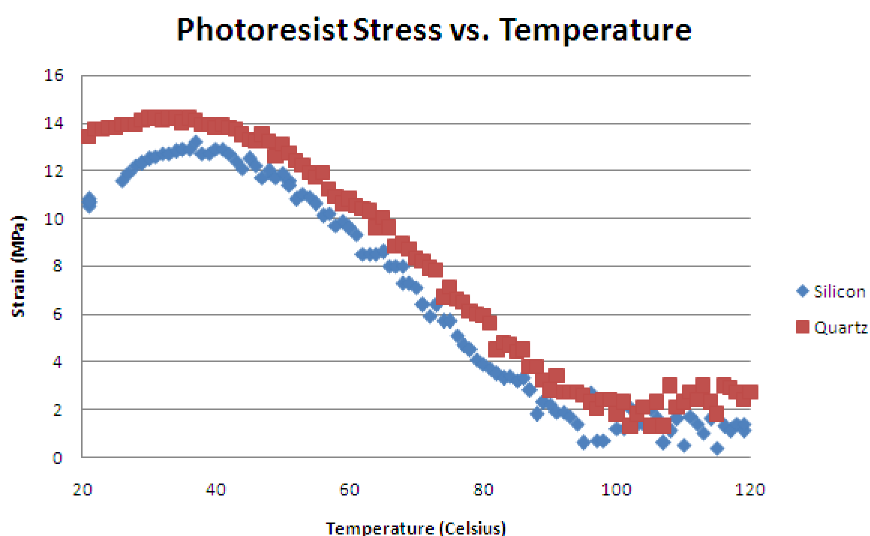

Figure 3.10: Stress-temperature profile of OCG 825 photoresist on silicon and quartz substrates.

A thermal cycle consisting of heating the resist to 120°C and then cooling demonstrated that photoresist does not have the stress-temperature hysteresis that is characteristic of chitosan, as shown in Figure 3.11. The lack of hysteresis in the film demonstrates that photoresist has a reduced sensitivity to changes in humidity or moisture as compared to chitosan. The response in photoresist is seen to be highly linear over a wide temperature range with no dependence on

the direction of heat flow, and the stress-temperature profile is primarily due to thermal expansion.

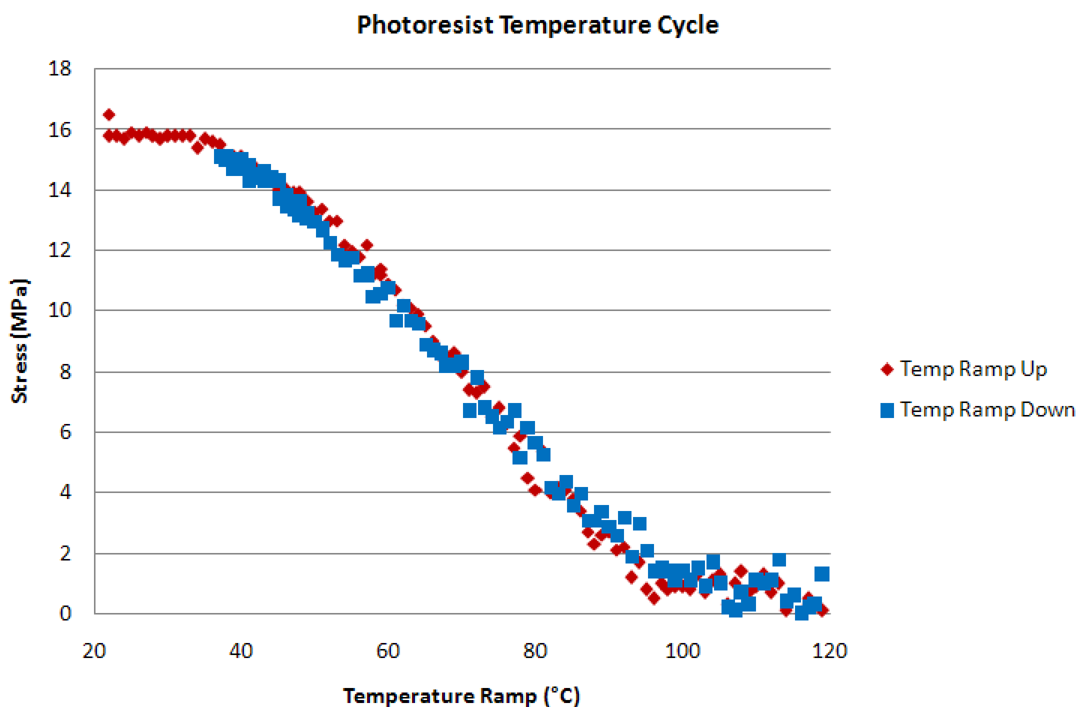

Figure 3.11: No difference is the stress-temperature profile of OCG 825 photoresist is observed between a heating cycle and a cooling cycle.

3.11 Contact angle

The contact angle is an interface measurement technique for determining the wettability and relative degree of hydrophilicity or hydrophobicity of a surface. Contact angle measurements were used to observe differences in surface wetting

and to compare the surface properties of chitosan and chitin. Contact angle measurement is a simple method for observing changes in the surface and material properties caused by chemical modification such as NaOH neutralization or reacetylation - processes where little change in the film may be observed visually. A Kruss contact angle measurement system using DI water was used for these measurements.

3.11.1 Chitosan contact angle

The contact angle for a chitosan thin film (salt form) that had been dry for several days was found to be $59 \pm 3.9°$. This represents a somewhat hydrophobic surface. The chitosan surface following film neutralization using 0.1 M NaOH for 5 minutes was found to be significantly more hydrophilic.

Chitosan contact angles after NaOH neutralization for two different wafers were found to be $45 \pm 3.4°$ (versus 98° before NaOH neutralization) and $25 \pm 2.2°$ (versus 98° before NaOH neutralization). The variability between wafers following the NaOH treatment may be attributed to differences in rinsing technique (rinsed with DI water in the former case and submerged in DI water for 5 minutes in the latter) and length of exposure to the NaOH.

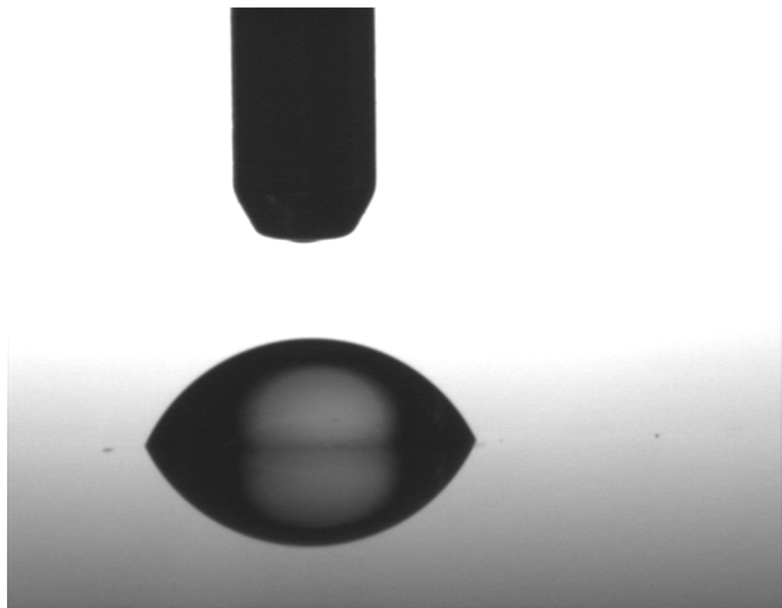

Figure 3.12: Contact angle measurement for chitosan thin film (salt form).

3.11.2 Chitin contact angle

Contact angle measurements were performed for chitin films obtained following reacetylation of spin-coated chitosan. The contact angle for a chitin thin film was found to range between 42-45°. These measurements are unexpectedly similar to those obtained for chitosan films that were neutralized with NaOH and rinsed with DI water. Pure chitin is highly hydrophobic, which accounts for its insolubility in water [22]. Therefore, it would be expected that the chitin thin film would have a larger contact angle. The contact angle is clearly sensitive to the processing conditions, and also appears to change over time.

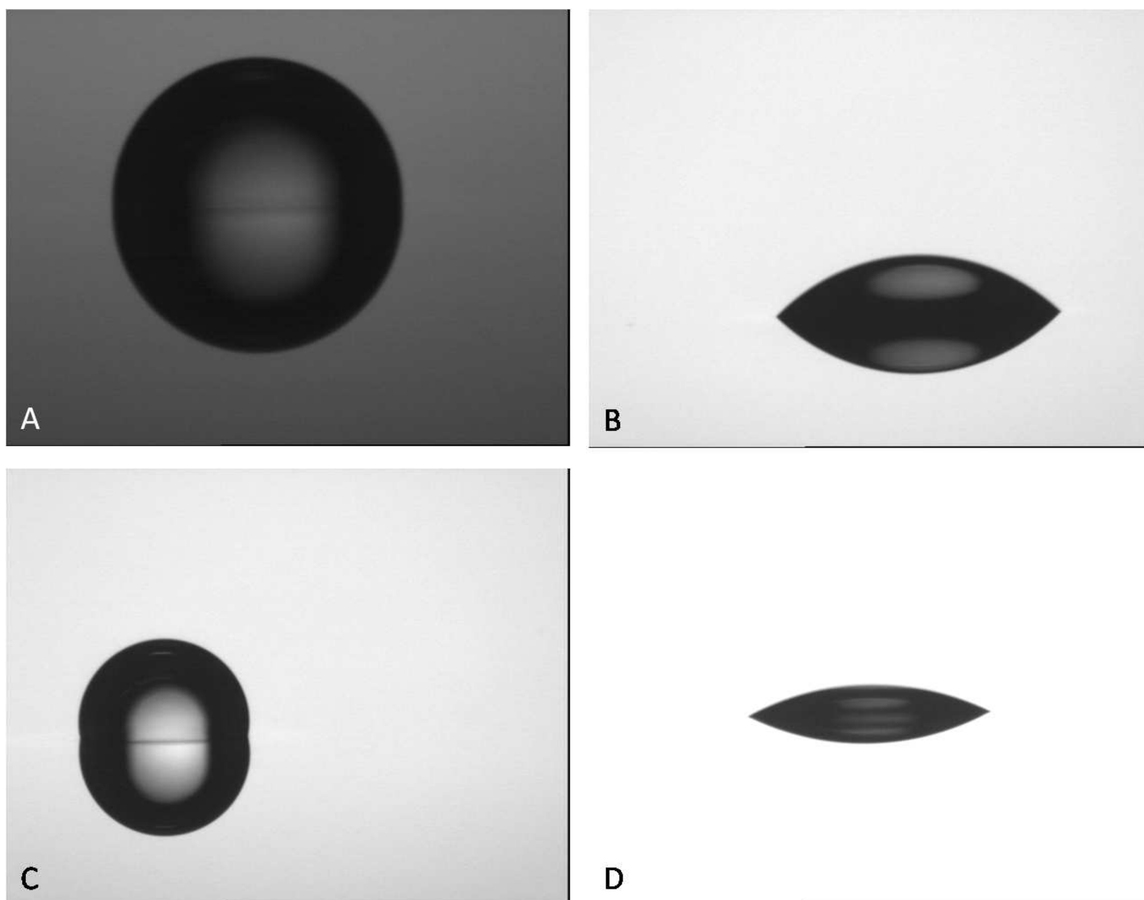

Figure 3.13: Contact angle measurement for chitosan thin film before and after NaOH neutralization treatment: a) Chitosan (salt form) as deposited b) Chitosan following 5 minute neutralization in 0.1 M NaOH and DI water rinse c) Chitosan (salt form) as deposited d) Chitosan following 5 minute neutralization in 0.1 M NaOH and 5 minute DI water soak.

The contact angle at the surface will affect the adhesion of the film, which is particularly important in photolithography processes. Hydrophobic-hydrophilic interfaces between two surfaces must be avoided in order to promote adhesion. The contact angle of chitosan and chitin thin films should be monitored after any

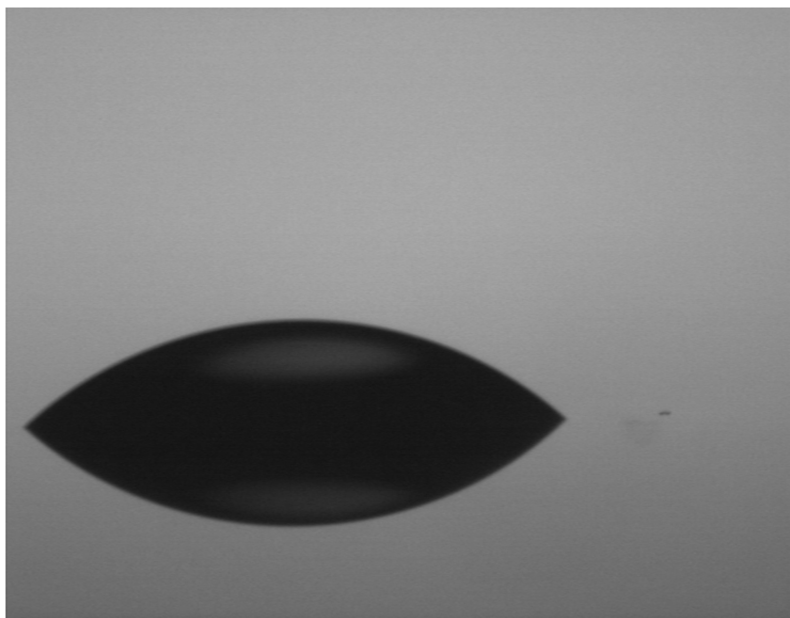

Figure 3.14: Contact angle measurement for chitin thin film.

change in processing conditions and as films age in order to identify shifts that could affect the film adhesion in microprocessing.

3.12 Summary

The primary advantage of chitin over chitosan is its resistance to changes in the environment. The higher degree of acetylation increases chemical stability and makes the film resistant to acids. Due to its ability to withstand harsh environments, such as salt water, it is chitin rather than chitosan that is used as the exoskeletal material in nature.

Properties of chitin and chitosan, such as the degree of acetylation and the contact angle, may be chemically modified. This versatility allows the properties of the films to be tailored to specific applications. Furthermore, the primary amine group present in chitosan enables a variety of surface functionalizations which provides great flexibility for biological and chemical sensing applications.

Although the stress-temperature hysteresis is more readily eliminated in chitin, both materials exhibit a sensitivity to moisture. The moisture sensitivity produces an effective negative coefficient of thermal expansion. Vacuum packaging or hermetic sealing in a nitrogen or argon environment can be used to minimize the effect of the film's sensitivity to changes in humidity. Alternatively, this effect may be exploited to develop MEMS-based hygrometers using chitosan thin films.

Chapter 4

Infrared Sensitive Cantilever Bimorph Design

4.1 Background

Microcantilever bimorphs have found application in a variety of mechanical, chemical, biological, thermal, and infrared/optical tranducers. Typically these bimorphs are formed of a structural layer and a transduction layer. When stimulated with energy, a bending moment is produced due to the coefficient of thermal expansion mismatch between the tranduction layer and the structural layer. This bending moment causes an out-of-plane deflection. Sensitivity is dependent on the absorption of energy and the conversion of that energy to mechanical deflection. Analytical models are used to predict the deflection of the beam when the total deflection is a small fraction of the beam thickness. Mechanical deflection is dependent on geometry and material properties of the thin film layers. Length of the

cantilever beam and thickness of the thin films are the most important geometrical aspects of cantilever deflection. Young's modulus, Poisson's ratio, and coefficient of thermal expansion are the most important material properties. Several models have ignored Poisson's ratio, introducing a 20-60% error in predicted deflection. In addition, residual stress from thin film deposition must be considered.

A thermally actuated cantilever bimorph composed of a high CTE (coefficient of thermal expansion) polymer absorbing layer and a low CTE structural layer was designed, simulated, fabricated, and tested. The bimorph was formed of photoresist as the absorbing layer and polycrystalline silicon as the structural layer. Finite element modeling of the bimorph demonstrated significant out-of-plane deflection for input levels of thermal energy. In addition, finite element modeling revealed deficiencies in a common analytical model and revealed the importance of Poisson's ratio for accurately predicting beam bending. Based upon improved models, an optimal design was identified. This work is relevant to applications in passive infrared detection, thermally-driven actuators and microscale mechanical switches.

4.2 Basic Device Concept

The basic device concept is shown in Figure 4.1. A bimorph is formed between two different materials with CTE mismatch. An air gap is formed by partially etching a sacrificial oxide spacer, and this allows free movement of the beam.

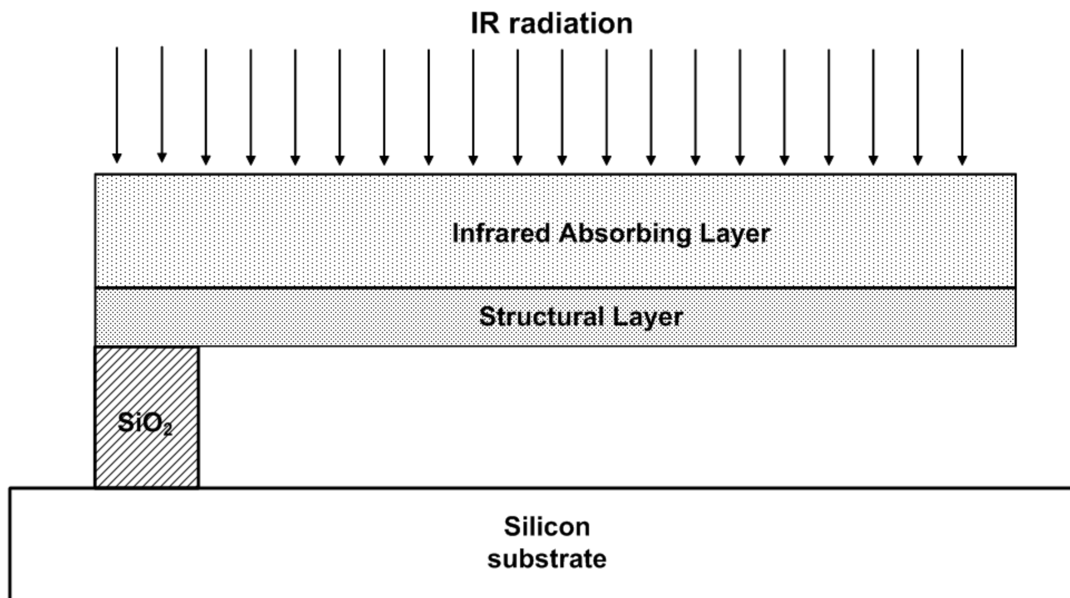

Figure 4.1: Cantilever basic concept.

This basic device concept can be modified in a number of ways. For example, the device may be coated with metal for use as an infrared reflector that will increase sensitivity by improving absorption. For a sputtered or evaporated metal over a released beam structure, the device would be back-illuminated.

4.3 Design Considerations

As a class of materials, polymers have the highest coefficients of thermal expansion, while semiconductors and ceramics have the lowest. In microfabrication, photoresists are the most commonly used polymers, making them a natural choice for highly mismatched cantilever bimorphs both in terms of mechanical functionality and ease of fabrication. SU-8, a negative resist, has a CTE of approximately 52×10^{-6} / °C [44]. Recent work has explored using polymers with microfabricated structures to achieve strong actuation and highly sensitive cantilever bimorphs, particularly for infrared thermal detection applications. LeMieux *et al.* coated silicon microcantilever AFM probes with a 20-200 nm thick PECVD polystyrene to achieve a temperature resolution of 0.2 mK and thermal sensitivity of 2 nm/mK [45].

Deflection of the cantilever is a function of material properties and mechanical dimensions. The relevant material properties are the coefficient of thermal expansion, the Young's modulus and the Poisson ratio. The length of the cantilever and the thicknesses of the top and bottom bimorph layers are parameters that may be adjusted by the designer once the material set has been determined. The out-of-plane deflection is driven by a change in temperature and is caused by the differential expansion between the top and bottom bimorph layers. As the

bimorph is heated, a bending moment is produced due to the difference in the coefficient of thermal expansion of the materials. For transduction applications, such as for thermal infrared sensors, material properties such as thermal conductivity, heat capacity and specific heat must be considered to maximize the change in temperature for a given amount of input energy. To maximize CTE mismatch while using conventional microfabrication materials, the cantilever bimorphs were designed to be made of a polysilicon structural layer with a photoresist coating. Polysilicon has several advantages for use in highly mismatched bimorphs; it has a low coefficient of thermal expansion (among common microfabrication materials, only silicon carbide and diamond have lower values) and it has found widespread use as a structural material in MEMS. Cantilevers 100, 200, and 300 μm in length, with widths of 5, 10, and 20 μm, were drawn and used to fabricate the infrared-sensitive device.

4.3.1 Choice of Materials

A variety of parameters are involved in the selection of materials. All material selections must keep in mind the realities of available manufacturing equipment and available processing techniques. For infrared detection, the optical properties of the absorbing layer are of foremost importance. The ideal material will have very strong absorption at the target wavelength of interest and very low absorption

outside of the target band. In addition to the optical properties of the absorbing layer, the thermal properties of all device components must be considered in order to maximize the sensitivity of the device. Thermal expansion mismatch should be maximized. Polymers as a class have high coefficients of thermal expansion, making them strong candidates for use in microcantilever-based infrared sensors. In general, a material with a low degree of cross-linking will have a higher CTE than the same material with a high degree of cross-linking [15]. The anchor should be thermally insulating to minimize thermal noise coming into the beam through the anchor, while also minimizing the thermal time constant. The polymer layer should have a low heat capacity such that a small amount of absorbed infrared energy produces a large temperature change. Because the heat capacity is defined as the product of the thermal mass and the specific heat of the material, a low heat capacity is achieved by selecting materials with a low specific heat and by making devices very small. Here, microelectromechanical systems processing techniques are leveraged to achieve low heat capacity and therefore attain high performance while also benefiting from increased integration density, low power, and low cost.

4.3.2 Infrared Absorption

As shown in the FTIR spectra of Chapter 1, polymers have infrared absorption spectra that are specific to their organic bonds. Infrared absorption is due to

vibrational resonance modes of the organic bonds which fall in the teraHertz range. By selection of a polymer with bonds that absorb at the target wavelength, the temperature change caused by IR may be maximized.

The FTIR absorption spectrograph provides insight into the spectral sensitivity of each material. The material itself provides a natural filter that effectively modulates the optical power at a surface - absorbing at some wavelengths and transmitting at others. Therefore, the FTIR absorption spectrum provides information analogous to the spectral irradiance, which is defined as the amount of energy of a specific wavelength present at a surface. Therefore, it is convenient to model the spectral absorption of the material as observed using FTIR spectroscopy as a spectral irradiance transfer function. The "'irradiance"' due to the optical absorption properties of the material may be defined as the area under the spectral irradiance-wavelength curve, defined by the integral:

$$E = \int E_\lambda(\lambda)\, d\lambda \tag{4.1}$$

where $E_\lambda(\lambda)$ has the units of Wm^{-3} and E has the units of Wm^{-2}. The total energy under the curve is a power density, or intensity. The total radiant energy at the surface is defined as the radiant energy Q and may be defined as:

$$\frac{dQ}{dt} = EA \tag{4.2}$$

where Q in in Joules. The time rate of change in the radiant energy is the radiant flux:

$$\Phi(t) = \frac{dQ}{dt} \tag{4.3}$$

and has the unit of Watts.

Conversion of infrared energy into heat in the detector is described by the thermal exchange equation, which is defined by the differential equation [46]:

$$c\frac{d(\Delta T)}{dt} + G_{th}\Delta T = \alpha\Phi_s \tag{4.4}$$

where c is the heat capacity, and G_{th} is the thermal conductance, α is the spectral absorptance, and Φ_s is the radiative flux.

The thermal conductance is defined as [47]:

$$G_{th} = k\frac{A}{l} \tag{4.5}$$

where k is the thermal conductivity of the material, A is the cross-sectional area and l is the length of the heat channel.

4.3.3 Thermal mismatch

The thermal expansion mismatch between the two layers of the cantilever bimorph is responsible for the out-of-plane bending that occurs when the structure is heated. Ceramics and highly crystalline materials such as silicon have very low coefficients of thermal expansion, metals have intermediate values, and polymers achieve the highest values. To maximize thermal expansion mismatch of the device, a high CTE polymer should be selected for the infrared absorbing layer and a low CTE semiconductor or ceramic should be chosen for the structural layer.

4.3.4 Thermal losses

Thermal losses occur due to conductive, convective, and radiative processes. Heat loss to convection is small in comparison to heat loss through the anchor, and

is therefore neglected in the design process. Thermal conduction to the air must be considered in addition to thermal conduction through the anchor. The thermal conductivity of the air at atmospheric temperature and pressure is $2.4 \times 10^{-}2$ $Wm^{-1}K^{-1}$ [48]. In comparison, the thermal conductivity of the silicon dioxide anchor is approximately 1.4 $Wm^{-1}K^{-1}$. Although these thermal conductivities are roughly two orders of magnitude apart, the area of contact with the air will be significantly greater than the area of contact with the anchor. Therefore, the primary mechanism which dissipates thermal energy in the structure will be highly dependent on geometry. The anchor is the primary design point in the cantilever structure for modifying the thermal time constant. Vacuum packaging will modify the thermal time constant by largely eliminating conduction to the air.

4.3.5 Geometry

Besides material selection, geometry is the only other element the designer has control over. The pixel size must be designed to capture a sufficient amount of incident infrared energy. The gap between the cantilever beam and the substrate must be chosen to prevent contact between the two which could result in stiction. Moreover, this gap can be further engineered to create a resonant cavity to increase absorption near a particular wavelength. Finally, the layer thicknesses must be selected to maximize the thermomechanical response of the device.

Pixel size

While the desire to increase transistor density has driven the integrated circuit industry to smaller and smaller minimum feature sizes (currently at 65 nm, transitioning to a 45 nm node), shrinking the device size of infrared transducers has only a limited effect. Because the wavelengths characteristic of the infrared portion of the electromagnetic spectrum are long relative to those in the visible, ultraviolet, or x-ray regions, the size of diffraction-limited optical spots are fairly large [49]. Mathematically, the diameter of the diffraction-limited Airy disk is defined by:

$$d = 2.44\lambda f_{\#} \tag{4.6}$$

where λ is the wavelength and $f_{\#}$ is the f-number of the optics.

For example, for a 3 μm wavelength and f/1 optics, the optical spot size is 7.32 μm. Longer wavelengths will have even larger diffraction-limited optical spot sizes. Such minimum feature sizes are readily achieved using today's lithography. Shrinking device sizes below the diffraction limit allows for oversampling, and is also readily achievable using current lithography equipment [49].

Resonant cavity absorber

A $\lambda/4$ resonant cavity may be produced between the beam and the substrate to increase the absorption at a particular wavelength. However, forming this resonant cavity to increase the infrared absorption at a particular frequency has consequences in capacitive devices formed between the bimorph and the substrate by constraining the size of the air gap. Furthermore, depending on the wavelength the cavity is being optimized for, it may result in a gap between the beam and the substrate which is too narrow and could result in the beam coming into contact with and sticking to the substrate. Due to these disadvantages as well as the ability to tune the absorption by selecting polymers with natural absorbance at the infrared wavelengths of interest, a resonant cavity absorber was not integrated into this design.

Due to the presence of the sacrificial oxide spacer which leaves an air gap, the possibility exists for the creation of a "parasitic" resonant cavity absorber which could increase the absorption of an unwanted wavelength of infrared radiation. However, by selecting a sacrificial oxide thickness ranging from 1.25 μm to 2 μm, the "parasitic" quarter-wavelength resonant cavity can be made nonfunctional due to the strong atmospheric absorption which exists in the 5-8 μm wavelength range, which prevents wavelengths in this range from reaching the detector.

Thickness ratio

Once a mask set is produced, the thicknesses of the absorbing layer and the structural layer are the only remaining parameters that may be adjusted to tune device performance. Layer thickness is determined by the process deposition conditions and deposition time. For example, the thickness of a polysilicon structural layer is determined by the deposition time and the pressure used in the low pressure chemical vapor deposition. The thickness of materials deposited by spin-coating such as photoresist depend on the solution viscosity and the spin-speed of the coater. The analytical models described next will show the importance of selecting the proper thicknesses to achieve maximal beam deflection. However, there are additional benefits to selecting thin layers in addition to maximizing the out-of-plane deflection. For example, Lee *et al.* identified a lower risk of delamination failure due to interfacial residual stress when using a thinner layer [50].

4.4 Thermomechanical analytical solutions

A simplified analytical model for predicting out-of-plane deflection in a cantilever bimorph due to a temperature change was proposed by Hunter *et al.* [51, 52, 53]:

$$y = \frac{3L^2}{8t_{bi}}(\alpha_{bi} - \alpha_{subs})(T - T_o)K \tag{4.7}$$

where:

$$K = \frac{8(1+x)}{4 + 6x + 4x^2 + nx^3 + \frac{1}{nx}} \tag{4.8}$$

$$n = \frac{E_2}{E_1} \tag{4.9}$$

$$x = \frac{t_2}{t_1} \tag{4.10}$$

The Hunter model is dependent upon length of the bimorph, coefficient of thermal expansion mismatch, and the thickness and Young's modulus of each layer.

The Gehring model [54] offers an improvement over the Hunter model by incorporating the Poisson ratio effect. The Gehring model replaces the Young's modulus in the Hunter model with the biaxial modulus:

$$y = \frac{3L^2(\alpha_{bi} - \alpha_{subs})(T - T_o)(t_a + t_b)K}{t_a t_b} \tag{4.11}$$

$$K = \left(\left(\frac{t_a}{t_b}\right)^2 \frac{Y_b(1-\nu_a)}{Y_a(1-\nu_b)} + 4\frac{t_b}{t_a} + 6 + 4\frac{t_a}{t_b} + \left(\frac{t_a}{t_b}\right)^2 \frac{Y_a(1-\nu_b)}{Y_b(1-\nu_a)} \right)^{-1} \tag{4.12}$$

Another limitation of the Hunter model is that it assumes that the top layer thickness >> bottom layer thickness. While the Hunter model failed to agree with the results of finite element simulation, the Gehring model was found to match well. In addition, the Gehring model is superior for predicting the deflection of microfabricated bimorphs where the ratio of the thicknesses is generally < 10:1.

Recently, Djurić *et al.* modeled the bimaterial cantilever as a mechanical oscillator [55]. Their model investigated the influence of the surrounding air on the sensitivity, specific detectivity, and time constant of the detector. They found that as the pressure decreases, the Q-factor, the sensitivity, the specific detectivity D^*, and the thermal time constant all increase. When adjusting the pressure, there is a trade-off between the detectivity and the response time. High vacuum and

low conduction losses were found necessary to reach the near-background limited detectivity limit of $1.81 \cdot 10^{10} cm\sqrt{Hz}/W$.

4.5 Finite Element Model - 2D

2D finite element models were constructed assuming a unit width. The models were found to be inadequate because they failed to take into account the Poisson ratio, which affects the biaxial modulus. This is inherently a three-dimensional effect and therefore it was determined that only a 3D finite element simulation could produce results with sufficient accuracy for design purposes.

4.6 Finite Element Model - 3D

To account for the influence of Poisson's ratio, 3D finite element simulations of cantilever bimorph deflection were performed for beams made of a variety of materials. Because of the difficulty in modeling the absorption of infrared radiation by each polymer material due to the wavelength-dependence of that absorption, finite element models simulated how heat translated into mechanical deflection in the structure. Heat flux rather than absorbance or reflectance was therefore used in the boundary conditions. Finite element simulations were compared to results obtained from the Hunter analytical model. Results were found to agree

only for cases where the Poisson's ratio was 0 (no transverse contraction for an axial strain). This mismatch implied that the Hunter analytical model is an over-simplification that ignores the influence of the three-dimensional geometry and specifically neglects the change in layer thickness that results from the Poisson effect.

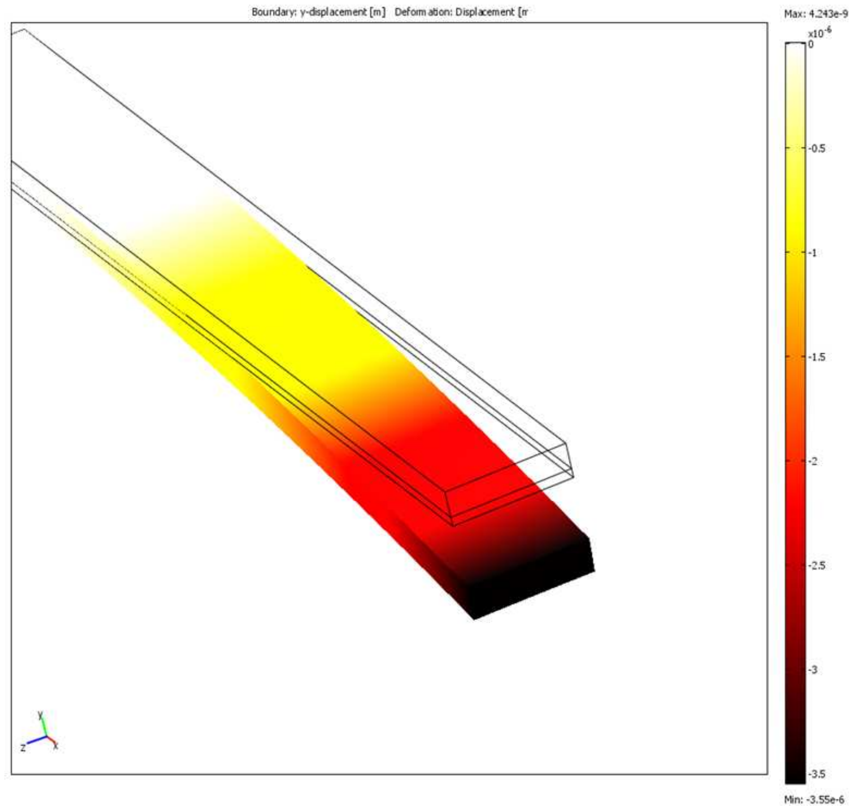

Figure 4.2: 3D finite element model showing a 1 μm PMMA layer on 700 nm of polysilicon. For a 5 mW/cm2 radiant flux which causes a temperature change of 25 K in the structure, the deflection is 3.55 μm for a sensitivity of 11 nm/K.

Significant out-of-plane deflection was observed for 5 mW/cm^2 levels on incident heat flux over the entire top surface of the cantilever beam.

4.7 Validity of Models

It is important to verify the analytical and finite element models if they are to serve as predictors of performance and be utilized to produce an optimized design.

First, it is important to verify that the 3D finite element model and the analytical model agree with one another. Table 4.1 shows the predicted performance using both the Gehring analytical model and the 3D finite element model. The error is well below 5% for these models and the models include differences in thickness ratio and substrate material.

	Gehring Model	Finite Element Model	% Error
1 μm PMMA on 700 nm polySi	3.5413 μm	3.559 μm	0.50%
2 μm photoresist on 700 nm polySi	3.5028 μm	3.55 μm	1.35%
700 nm PMMA on 300 nm polySi	9.7393 μm	10.02 μm	2.88%
1 μm PMMA on 700 nm SiO_2	5.5278 μm	5.604 μm	1.38%
700 nm PMMA on 300 nm SiO_2	12.127 μm	12.51 μm	3.16%

Table 4.1: Comparison of analytical and finite element models.

Next, it is important to identify areas where the model is inadequate, including assumptions that may be oversimplifications. Both of these models assume a perfectly flat beam at steady-state, and therefore fail to take into account the

presence of residual stress due to strain gradients in the film. Strain gradients are difficult to measure, are dependent on deposition and processing conditions, and are therefore difficult to model. Noise is another aspect which is not accounted for in the finite element simulation. While one design objective is to maximize the amount of deflection obtained for a given amount of absorbed infrared energy (sensitivity), another design objective is to minimize susceptibility of the system to noise (increase resolution). The former relates to D^*, while the latter relates to NETD. Both of these models assume a noise free environment. In reality, noise in the environment will produce some deflection and/or vibration in the beam when no infrared energy is present.

4.8 Optimal Design

The Gehring analytical model may serve as the basis for determining an optimal design for a material subset. For example, for a given bimorph material set, the deflection may be plotted as a function of the thickness of the absorbing layer and the structural layer to determine the optimal deflection for the beam. A three-dimensional plot is shown in Figure 4.3. The range of thicknesses over which such a plot is generated should be restricted to dimensions which are manufacturable, and in general no layer should be greater than 10x thicker than the other

layer. Lai *et al.* investigated the optimal design of bimorph microcantilevers using similar equations [56]. Their paper focused on metal-semiconductor bimorphs and examined the performance of silicon nitride, silicon, aluminum and gold as bimorph materials [56].

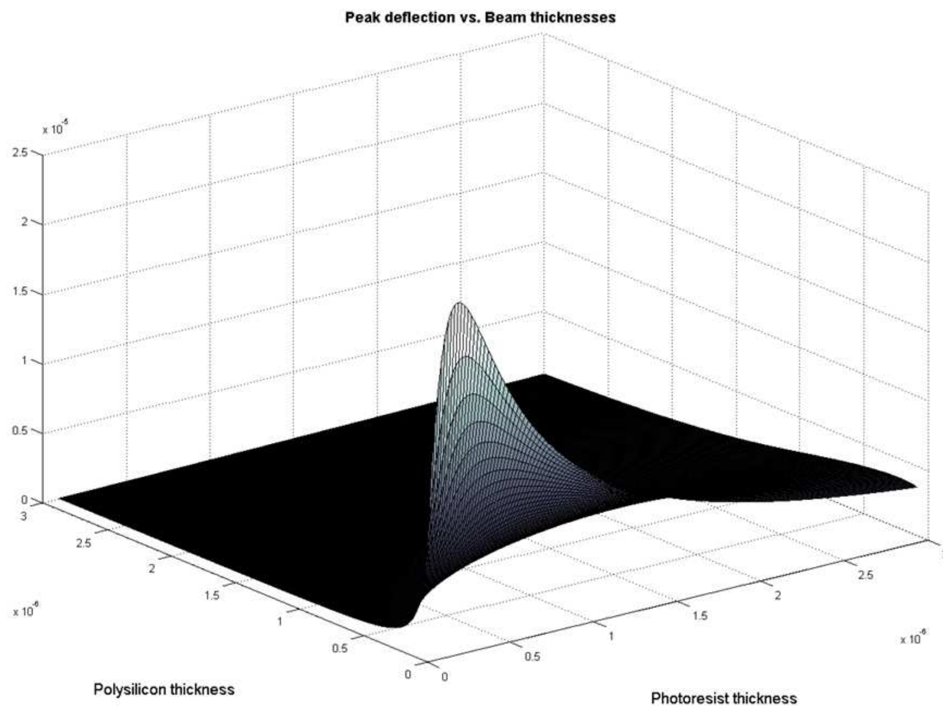

Figure 4.3: Optimal thickness dimensions for bimorph.

To determine the influence of the structural layer on the mechanical performance of the structure, finite element modeling was used to compare a polysilicon structural layer with a silicon dioxide structural layer. A bulk micromachining process could be employed to create a bimorph using silicon dioxide as the struc-

tural layer. Results shown in Table 4.2 that replacing polysilicon with a silicon dioxide structural layer can increase deflection by 20-50%. This is possibly due to the reduced thermal conductivity of silicon dioxide compared with polycrystalline silicon.

	"X"=Polysilicon	"X"=Oxide	% Improvement
1 μm PMMA on 700 nm "X"	3.559 μm	5.604 μm	57.46%
2 μm photoresist on 700 nm "X"	3.55 μm	4.345 μm	22.39%
700 nm PMMA on 300 nm "X"	10.02 μm	12.51 μm	24.84%

Table 4.2: Effect of structural layer

However, this model does not take into account the effect of the anchor which may greatly influence the heat transfer in the structure. A bimorph with a structural layer of silicon dioxide would most likely not have a silicon dioxide anchor. Therefore, these performance estimates are likely an overestimation of what could realistically be achieved in practice.

4.9 Responsivity

The responsivity of the cantilever-based infrared detector is the ratio of the output signal to the input stimulus. Responsivity may be measured at various

stages of the transduction process and can serve as a figure of merit for detector performance. For the optical device prototype, it may be defined generally as the amount of deflection achieved for a given amount of incident optical power:

$$S = \frac{\Delta y}{P_{optical}} \tag{4.13}$$

For the cantilever device, this may be defined in units of nm/W or μm/W, and will have a spectral sensitivity due to the varying degree of absorption by the polymer material. Material properties such as heat capacity and spectral absorbance affect the responsivity by determining how efficiently heat is absorbed into the structure and how well the structure produces a temperature change for a given amount of energy.

Because all thermal detectors first convert absorbed infrared radiation to heat, optical power and heat may be decoupled. The thermal responsivity can be defined as the amount of deflection obtained for a given temperature change. Thermal responsivity can be represented mathematically as:

$$S = \frac{\Delta y}{\Delta T} \tag{4.14}$$

where Δy is the deflection in microns and ΔT is the change in temperature in Kelvin. Substituting Δy from the Gehring model, one may obtain:

$$S = \frac{3L^2(\alpha_{bi} - \alpha_{subs})(t_a + t_b)K}{t_a t_b} \tag{4.15}$$

where K is shown in equation 4.12. The change in temperature falls out of the equation for the thermal responsivity.

The responsivity can further be refined to account for the presence of an electronic readout. For the capacitive-readout prototype, it may be defined generally as:

$$S = \frac{\Delta V}{P_{optical}} \tag{4.16}$$

where the change in voltage, for example, may be caused by a changing capacitance and is defined in a transfer function that is dependent on the specifics of the electronic readout circuitry.

4.10 Noise

For optical readouts, it is the thermal vibrational noise that dominates other noise sources [56]. Electronic readouts, such as a capacitive approach, introduce

additional noise sources. Johnson noise, which is a significant noise source in resistive microbolometers, is negligible in cantilever-based infrared detectors [7].

Ambient temperature fluctuation is also an important noise source for microcantilever-based infrared sensors. Corbeil *et al.* [57] developed a cantilever geometry that will largely cancel out ambient temperature fluctuation noise. Their device used thermally-actuated microcantilevers to cause the deflection of an absorbing plate. The plate serves as a large infrared absorbing area. An inner bimaterial cantilever and an outer bimaterial cantilever are connected by a thermal isolation region. Infrared energy absorbed in the plate will flow into the bimorph cantilever actuator and deflect the plate. Ambient temperature fluctuations will occur equally between the bimorph cantilever actuator and the opposing bimorph cantilever separated by the thermal isolation region (which is not actuated by infrared energy due to the presence of the thermal isolation region).

Thermal vibrational noise at off-resonance can be described by [56]:

$$y_{th} = \sqrt{\frac{4k_B T B}{k \omega_o Q}} \tag{4.17}$$

where B is the bandwidth, k is the spring constant, ω_o is the resonant frequency. and Q is the quality factor. Therefore, it is important to maximze the resonant frequency in order to minimize the thermal vibrational noise.

4.11 Resonant frequency

The resonant frequency ω_o of a lumped element system can be defined by:

$$\omega_o = \sqrt{\frac{k}{m}} \tag{4.18}$$

where k is the spring constant and m is the effective mass.

The spring constant of a rectangular cantilever beam is defined by:

$$k = \frac{Et^3w}{4L^3} \tag{4.19}$$

where L is the length of the beam, w is the width, and t is the thickness.

The bimorph is composed of two different springs sandwiched in parallel. As a result, the net spring constant may be defined as the sum of the individual spring constants:

$$k_{eff} = k_1 + k_2 \tag{4.20}$$

For a rectangular cantilever bimorph, the spring constant becomes [56]:

$$k_{eff} = (\frac{w}{4L^3}) \left[E_1 t_1^3 + E_2 t_2^3\right] \tag{4.21}$$

and the effective mass is:

$$m = 0.48wL(\rho_1 t_1 + \rho_2 t_2) \tag{4.22}$$

Substituting the spring constant and effective mass back into Equation 4.18, the resonant frequency becomes:

$$\omega_o = \sqrt{\frac{E_1 t_1^3 + E_2 t_2^3}{1.92L^4(\rho_1 t_1 + \rho_2 t_2)}} \tag{4.23}$$

$$f = \frac{1}{2\pi}\sqrt{\frac{E_1 t_1^3 + E_2 t_2^3}{1.92L^4(\rho_1 t_1 + \rho_2 t_2)}} \tag{4.24}$$

Like the deflection equation, the width of the beam has no impact on the resonant frequency, and therefore should not influence the sensitivity of the structure to thermal or mechanical noise. However, the width of the beam will affect the capacitance between the beam and the substrate and therefore is an important design consideration for capacitive readout.

4.12 Packaging

Dies may be packaged using wire-bonding to DIP enclosures and using an IR-transparent window such as germanium to protect the die from surface con-

tamination. Alternatively, dies can be mounted using flip-chip where the device is illuminated through the backside, as silicon is an IR-transparent material.

4.13 Methods of Increasing Performance

4.13.1 Metal reflectors

Metals not only reflect light in the visible range but they also reflect infrared radiation. Therefore, a very thin layer of metal may be coated over the polymer-based cantilever bimorph to increase the amount of radiant energy absorbed in the polymer. The most direct method for adding a metal reflector to the cantilever bimorph is to evaporate or sputter a metal such as aluminum over the released structure. This results in a back-illuminated device (illuminated through the silicon substrate and polysilicon beam, both transparent to IR). An analogous method has been utilized by nature in the cat's tapetum to increase the sensitivity of the visual system, an adaptation to a nocturnal lifestyle [58].

4.13.2 Vacuum packaging

Vacuum packaging may be used to increase the sensitivity of the device. Vacuum packaging reduces sensitivity to noise, as conduction between the air and the cantilever is eliminated. For chitosan and chitin as the infrared absorbing

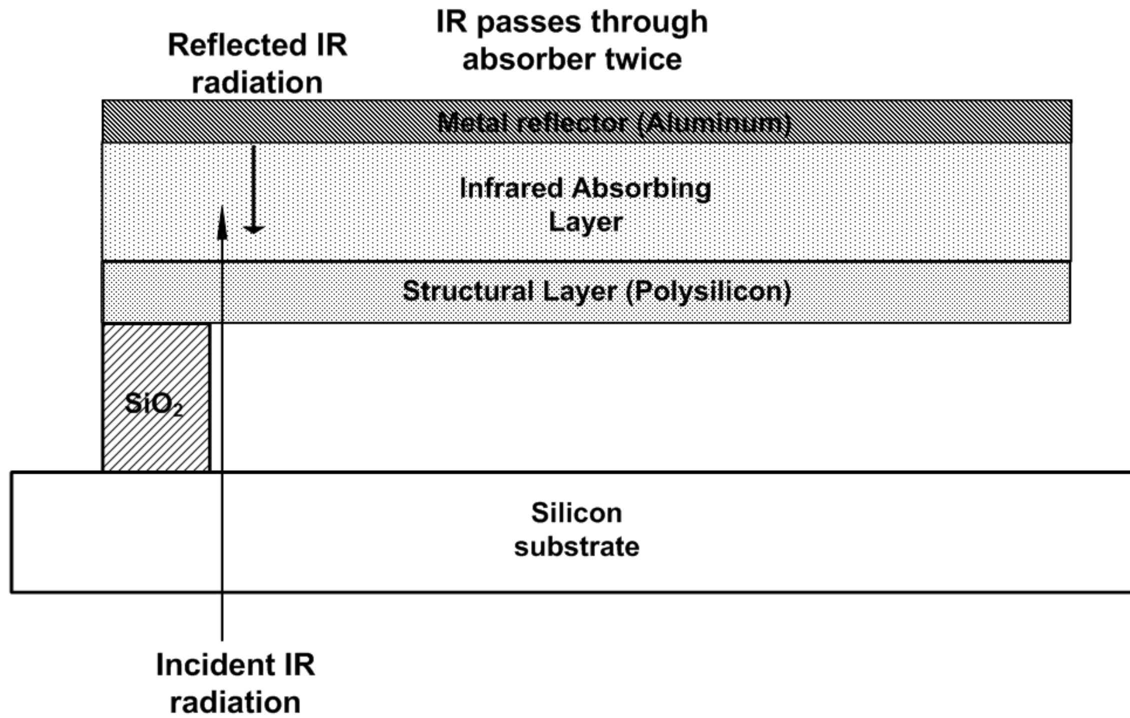

Figure 4.4: Cantilever metal reflector.

layer, vacuum packaging can eliminate the sensitivity to moisture which affects the stress in the thin film. Theoretical modeling performed by Djurić *et al.* [55] demonstrated that vacuum packaging can produce an order of magnitude improvement in D^*, but at the expense of the thermal time constant.

4.14 Device Fabrication

4.14.1 Optical Readout Prototype

From a fabrication perspective, optical readout is ideal for measuring cantilever deflection as it requires no readout circuitry to be fabricated on-chip. However, such external readout methodology is generally large, not portable, and expensive. Optical readout is ideally suited for a research environment and prototype testing.

Highly mismatched cantilever microstructures were batch fabricated on a 4” silicon substrate using photolithography and a single mask. In Figure 4.5 is shown the process sequence from starting wafer to final die.

A clean, bare <100> Si wafer was coated with a silicon dioxide film for use as a sacrificial layer. Silicon dioxide was deposited at 450°C using low pressure chemical vapor deposition (LPCVD). Next, a polycrystalline silicon structural layer was deposited by LPCVD at 615°C. Third, an OCG 825 G-line positive photoresist is spin-coated, UV-exposed, and developed. The photoresist was soft baked at 90°C for 60 seconds following spin-coating and hard baked after development at 120°C for 180 seconds using a Fusion M150PC photostabilizer system.

Polysilicon was dry etched using Cl_2 gas in a Lam poly-silicon rainbow etcher. This completes fabrication at the wafer scale. A final coat of photoresist is necessary as a protective layer prior to wafer dicing. Photoresist was spin-coated and

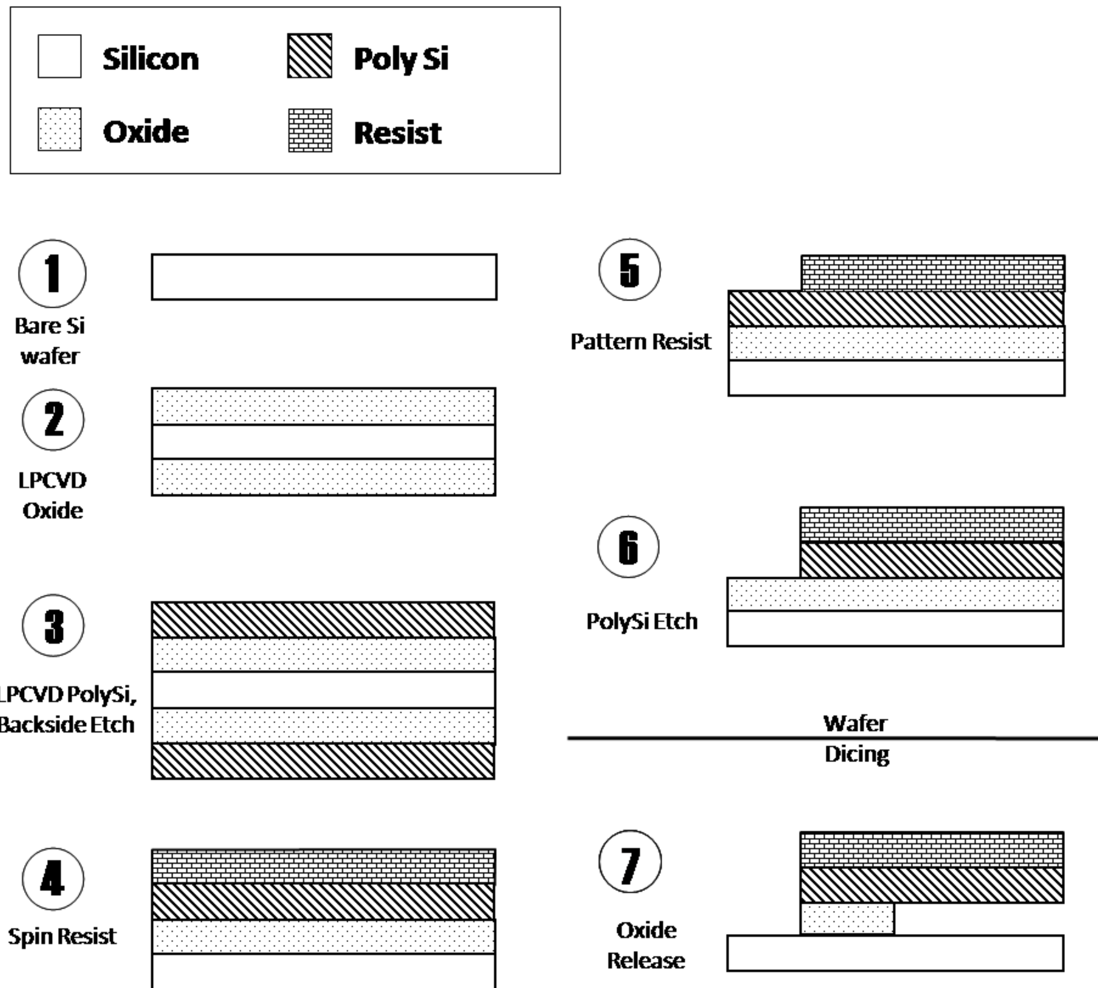

Figure 4.5: Optical prototype fabrication process flow.

soft baked at 90°C for 60 seconds, but was not hard baked. The wafer was diced using a disco automatic dicing saw. Following dicing, the protective photoresist was removed by dipping each die into PRS-3000 for 1 minute. Because of the different baking times, the protective resist is removed while the patterned, bimorph resist remains intact. Last, each die was released by performing an isotropic etch

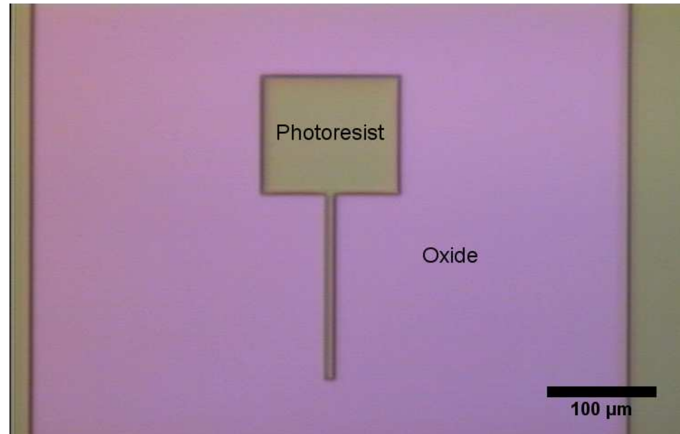

(a) After polysilicon etching.

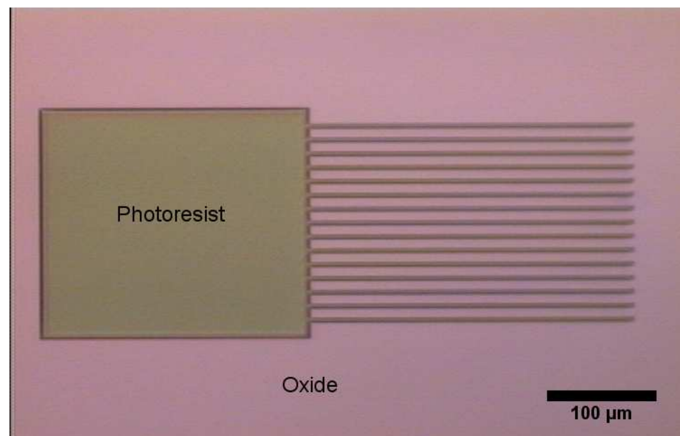

(b) After wafer dicing and removal of protective resist.

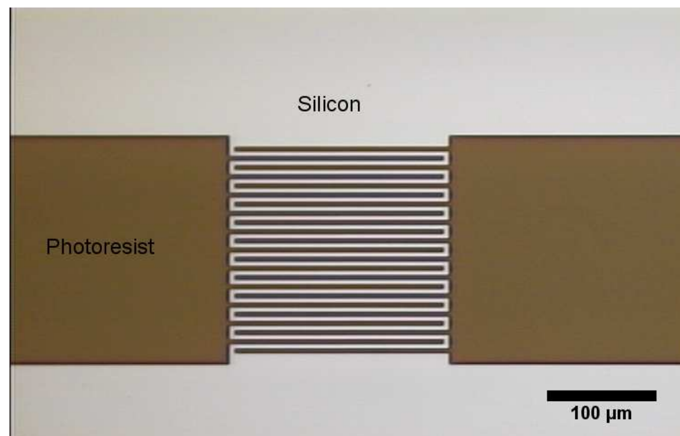

(c) After oxide release.

Figure 4.6: Micrographs of optical prototype cantilever beams during various stages of fabrication.

of the sacrificial oxide with HF vapor. Figure 4.6 shows the cantilever bimorph structure following polysilicon etching, removal of the protective photoresist, and oxide release.

4.14.2 Capacitive Readout Prototype

Capacitive readout is favored over optical methods for commercial and military applications because of its ability to be integrated into the sensor chip itself and its scalability for forming focal plane arrays. However, the fabrication is more complex and the interfacing off chip is nontrivial. Furthermore, cantilever readouts that measure capacitive changes between the beam and the substrate are particularly sensitive to residual stress as it increases the distance between beam and substrate which has a nonlinear effect on the capacitance.

Numerous geometrical arrangements can be formed to form the two plates making up a capacitor. For example, the silicon substrate may act as the bottom plate. Alternatively, another cantilever may form the opposite plate. In all devices, the IR-sensitive cantilever bimorph forms one side of a variable plate capacitor. The capacitor can take on several geometries depending on whether a differential effect is desired. A differential beam configuration would consist of one cantilever that is a bimorph, and one that is not, such that IR absorption causes deflection of the bimorph while not affecting the single-layer cantilever

beam. A schematic of this concept is shown in Figure 4.8. In all cases for the released beams, an air or vacuum gap is used as the dielectric. In our design of the capacitive-readout IR-sensitive cantilever bimorph, a simple parallel plate model has been assumed. To improve the capacitance model, the effect of fringing fields should be taken into account.

Fabrication of the capacitive readout prototype is a two-mask process with the first mask defining the area for wire-bonding and the second mask defining the structure of the sensor itself. The process sequence for the fabrication of the two-mask capacitive readout prototype is shown in Figure 4.7.

4.14.3 Wafer Dicing Process

The wafer dicing step becomes more critical for structures that employ photoresist in the device because of the need to employ a protective coating during the dicing process. Traditionally a photoresist layer is applied prior to dicing, the wafer is diced, and the protective resist is removed using a photoresist stripper that has no effect on device layers such as polysilicon or silicon dioxide. However, in this device, where photoresist remains intact as part of the device structure, the use of a photoresist stripper is potentially problematic. However, because of differences in the baking time of the device resist and the protective resist, the photoresist stripper may still be used so long as the resist strip time is carefully

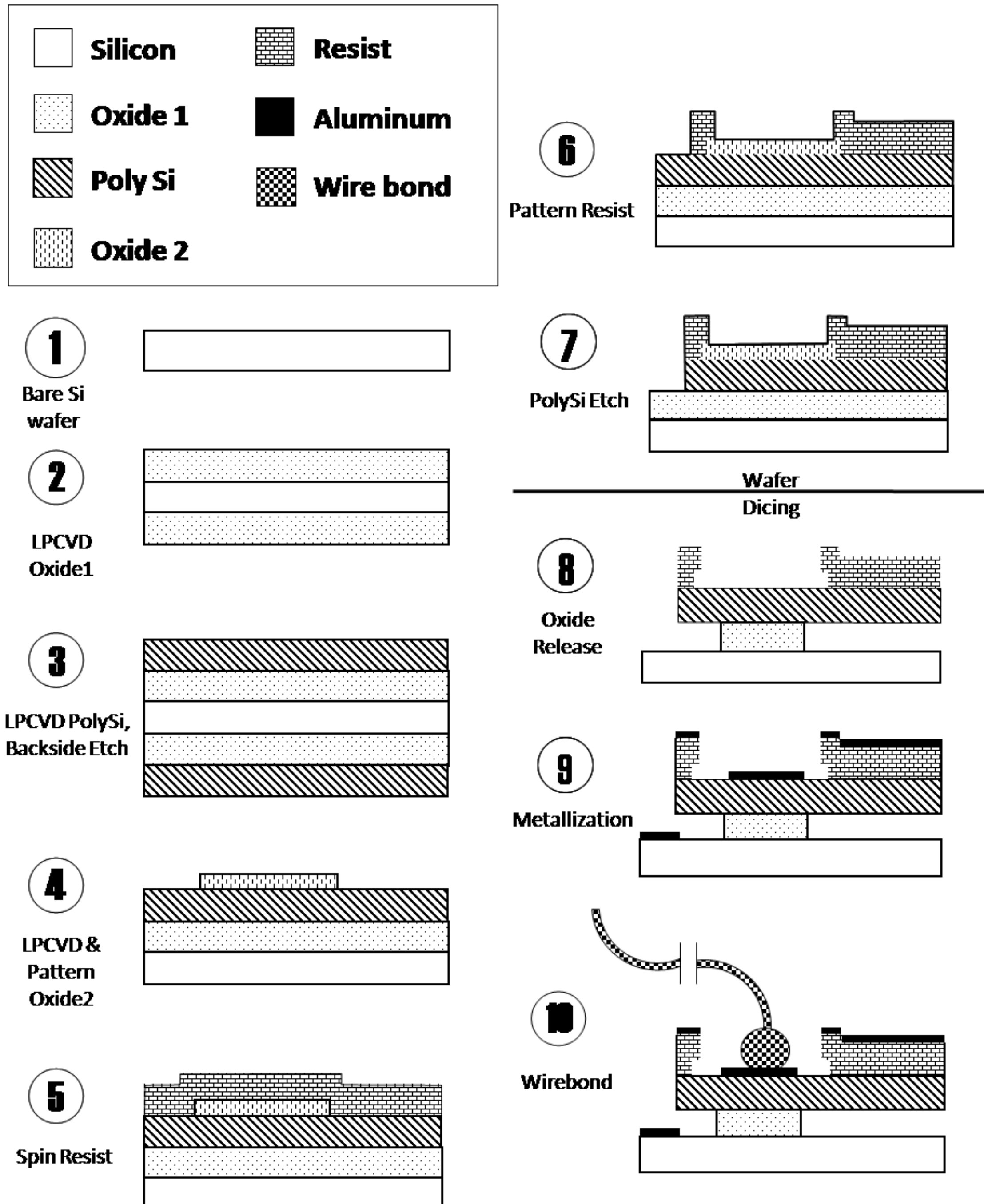

Figure 4.7: Two-mask process sequence for fabricating capacitive-readout IR sensor.

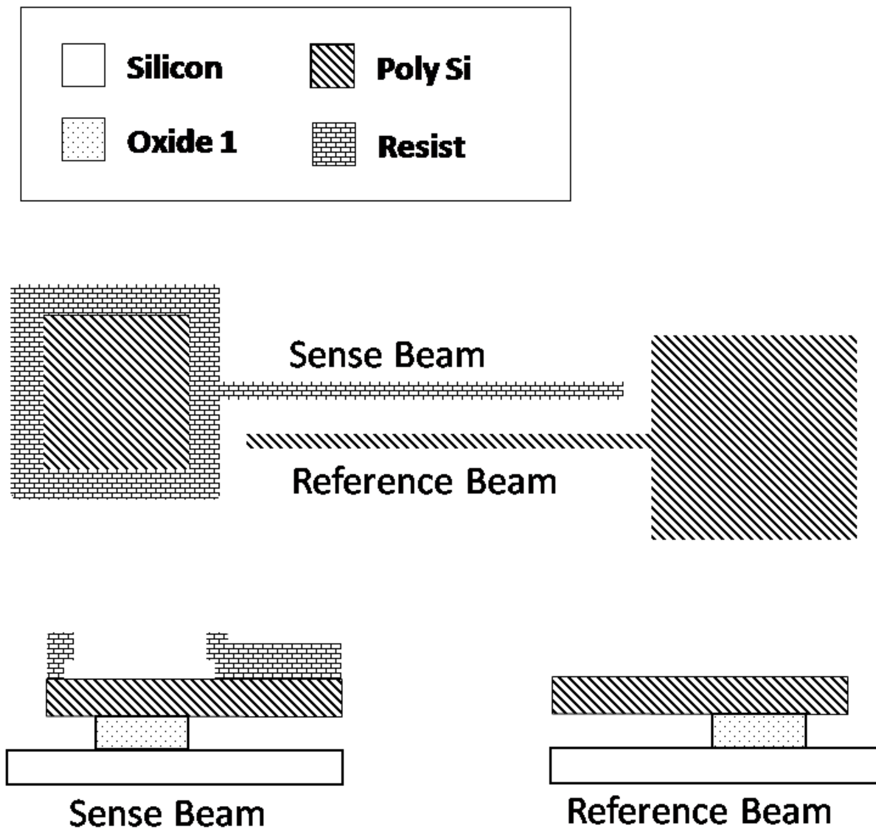

Figure 4.8: Differential measurement beam concept.

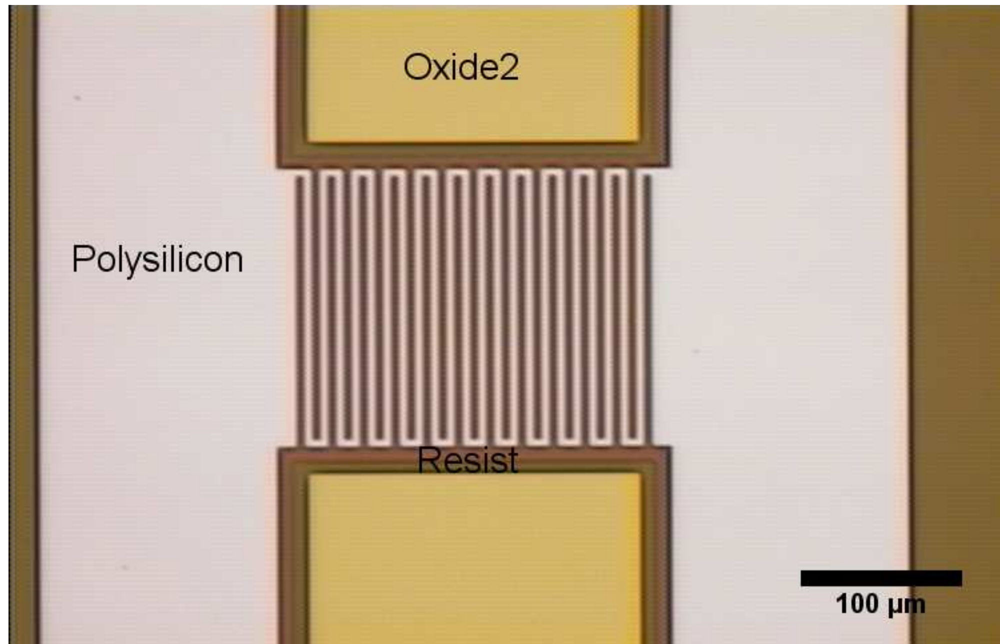

Figure 4.9: Cantilever following patterning of second photoresist layer.

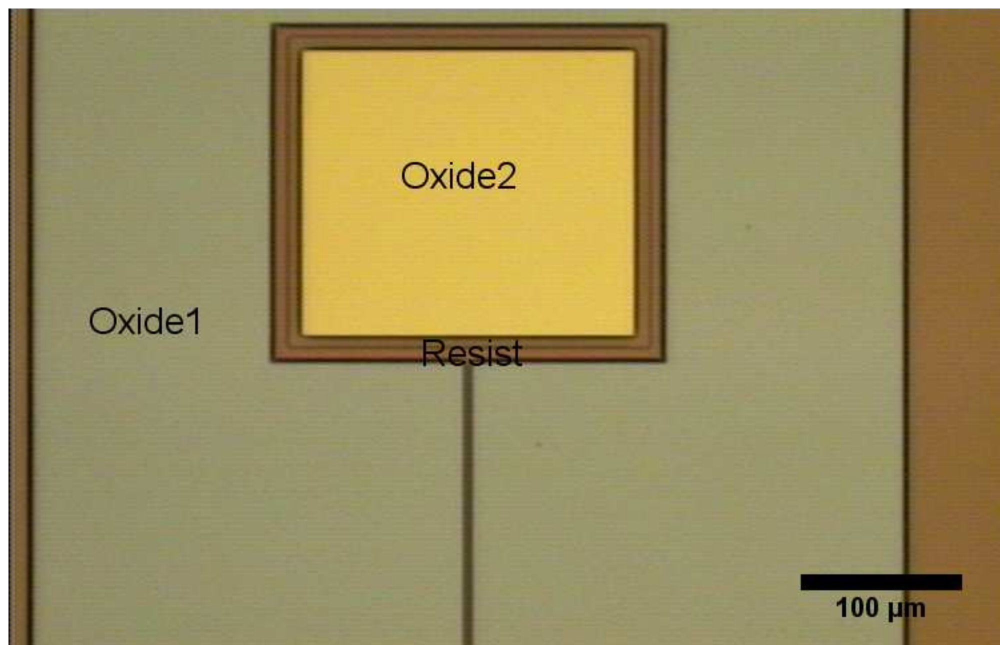

Figure 4.10: Cantilever following etching of polysilicon and prior to oxide release.

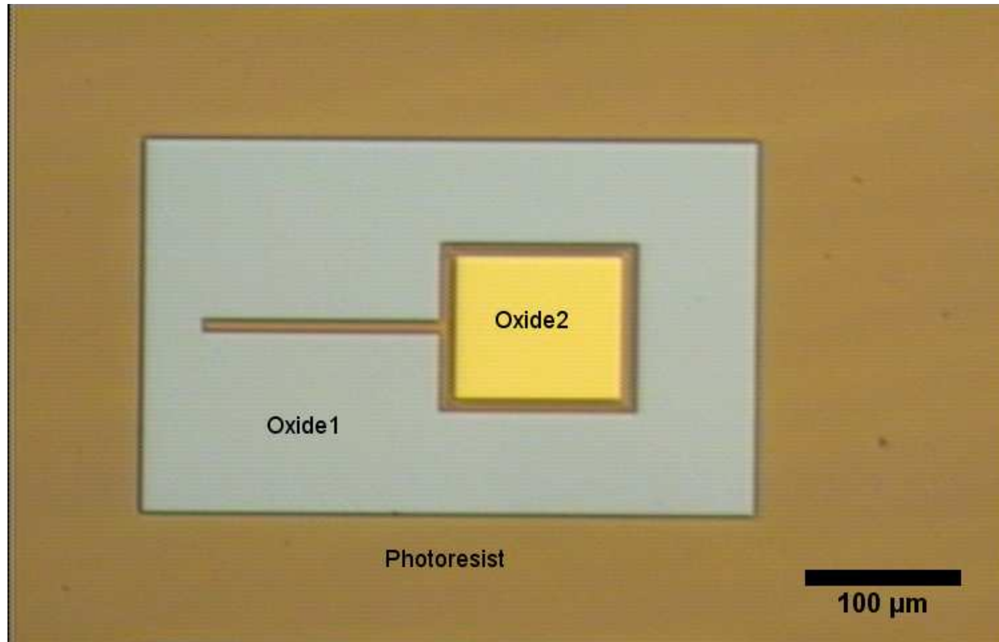

Figure 4.11: Feature after wafer dicing and removal of protective resist.

controlled. Figure 4.11 shows a cantilever feature on a die following wafer dicing and removal of the protective resist which maintains the device resist intact. The color of this image is virtually identical to that obtained on the wafer prior to dicing and following polysilicon etching, as seen in Figure 4.10.

As an alternative to the the protective photoresist, the wafer may be covered with a protective low tack tape. This eliminates the need to use a photoresist stripper that could potentially damage the device photoresist. However, the disadvantage is that the low tack tape must be removed manually from each chip following dicing using a razor blade (which can mar the die surface).

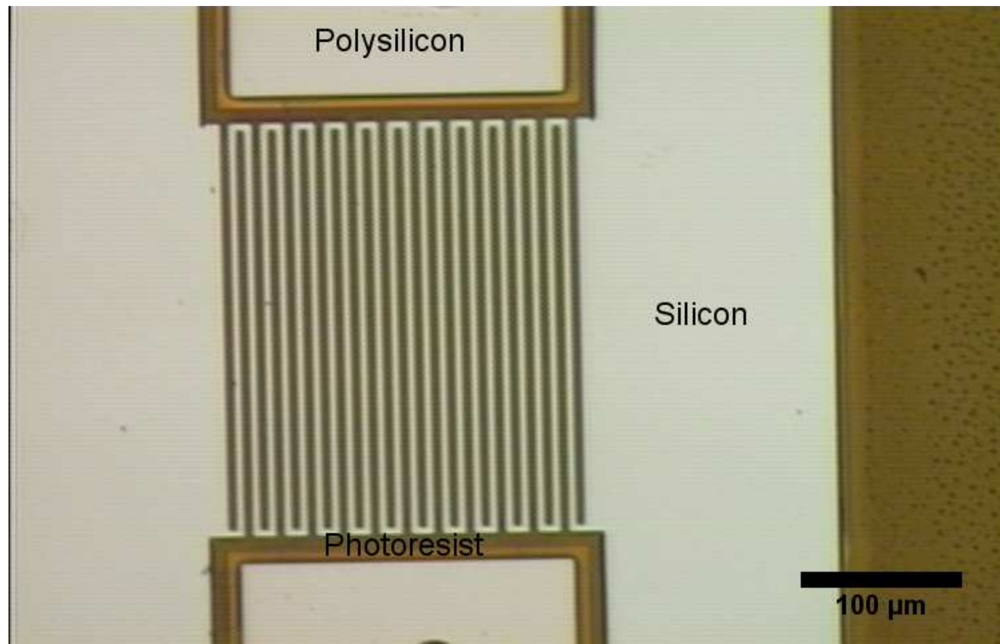

Figure 4.12: Released cantilever following removal of oxide with HF vapor.

To achieve a differential measurement, the capacitance may be measured between a bimorph cantilever and a polysilicon cantilever with no other layers. The fabrication of such a structure using known microfabrication processes is non-trivial because of the need to selectively remove the resist off of one beam while leaving it on the other. However, a simple process has been identified that appears promising for the construction of such a structure.

Fabrication of the differential bimorph involves adjusting the length of the photoresist strip step which is used to remove the protective photoresist following wafer dicing. When the die is placed in the PRS-3000 for 2 minutes, the PRS-3000 removes not only the protective resist but also some of the hard baked resist

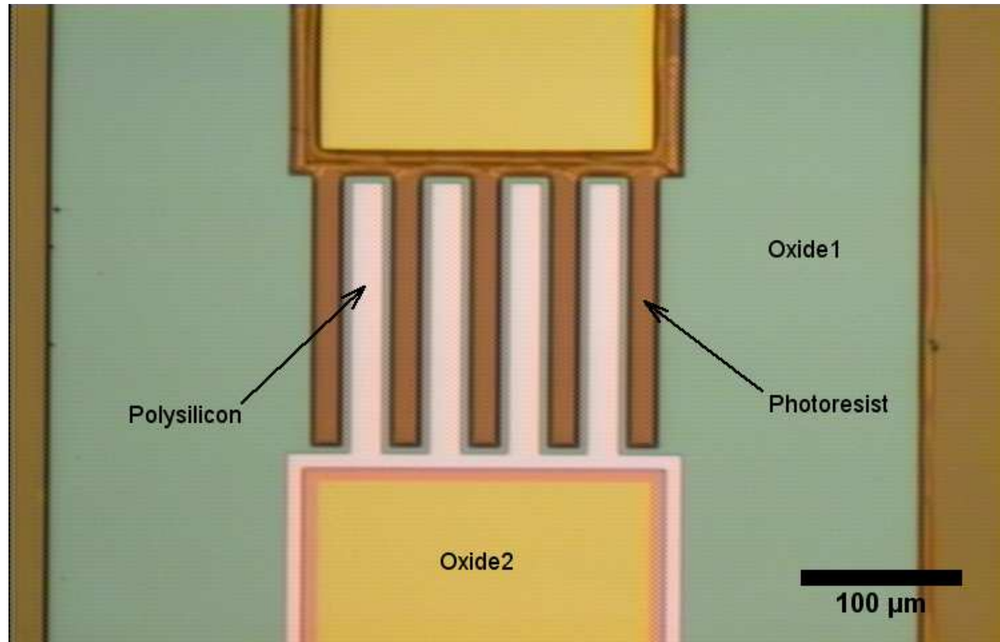

Figure 4.13: Fabrication of capacitive-readout bimorphs for differential readout (unreleased).

used in the device. Normally 1 minute in PRS-3000 is sufficient to remove the unbaked protective photoresist. Interestingly, for interdigitated comb structures, photoresist removal is observed to be preferential to one side, which allows the creation of a cantilever bimorph adjacent to a non-bimorph cantilever for use in differential measurement. An example of this feature is shown in Figure 4.13. The process is repeatable and has been observed on multiple dies.

4.14.4 Residual Stress

The dissertation by Zhao [59] noted that polymers would make even better CTE-mismatched bimorphs than materials such as aluminum but that their deposition induces a large residual stress that causes the beam to curl upon release. Indeed, residual stress is a significant problem for highly mismatched cantilever bimorphs even at relatively low processing temperatures. Residual stress will cause released structures to curl, which can be particularly problematic for capacitive sensors where the position of the capacitive plate can have a nonlinear effect on the output. Residual stress results from the deposition process - for example, during the low pressure chemical vapor deposition for polysilicon or during the spin-coating and hard bake for photoresist.

The photoresist hard bake may introduce a significant amount of residual stress into the polymer film. For example, the Fusion M150PC Photostabilizer System, which may be used to improve resist selectivity, operates at temperatures up to 240°C. The hard bake exposes the patterned resist to temperatures as high as 240°C before the release. After the release, the beams are at room temperature and the stress is released by curling, due to the 215°C variation in temperature that occurs during polymer processing. The Gehring analytical model can be used to predict the effect of residual stress on the curvature of a released cantilever beam. The Gehring analytical model predicts a deflection of 157 μm for a 200

μm long cantilever beam. 300 μm long released cantilever bimorphs were found to have out-of-plane deflections ranging from 122 μm - 137 μm as observed with an optical microscope. Measurements were made by focusing on the anchor and the cantilever tip and measuring the z-axis distance, as shown in the beams of Figures 4.14 and 4.15.

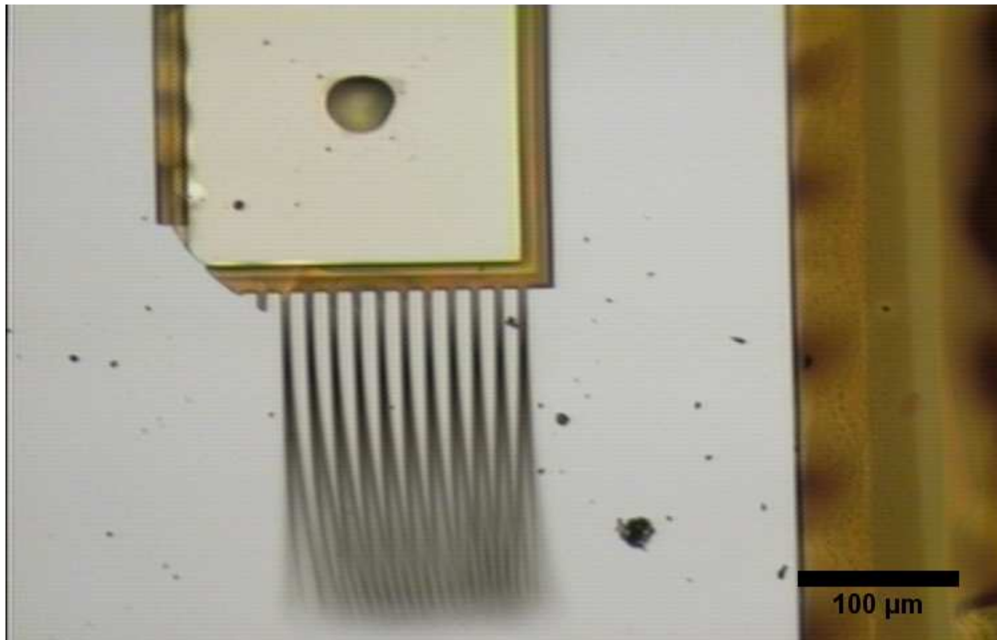

Figure 4.14: Released cantilever showing residual stress (focus on anchor).

Residual strains may be modified by thermal annealing [60]. Modification of beam curvature through post-processing has been described by Huang *et al.* [61, 60]. In this work, argon ion beam machining and rapid thermal annealing is used to reduce the curvature and flatten the released beams [61]. Their bimorph is composed of 200 nm thick PECVD-deposited SiN_x on 200 nm of evaporated

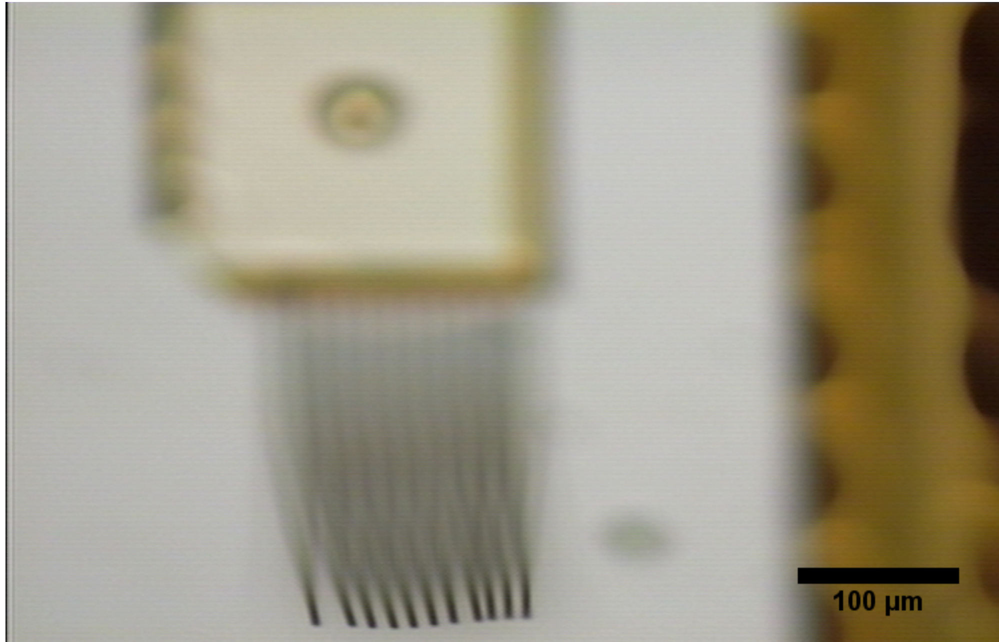

Figure 4.15: Released cantilever(300 μm long) showing residual stress (focus on tip).

aluminum. Rapid thermal annealing took place at 375°C for 5 minutes. However, this high temperature processing step is prohibitive for annealing photoresist as it is above its thermal degradation temperature.

To reduce the residual stress of the polymer-based infrared sensitive cantilevers, the fabrication process may be modified to anneal the polysilicon film following deposition. The hard bake of the photoresist may be modified to lower its temperature from 240°C to 120°C. Lastly, the released die may be annealed at 150°C.

In work by Lai *et al.* on metal-semiconductor cantilever bimorphs, bending of the cantilevers upon cooling was found to occur if a small temperature rise occurred during the metal film deposition (E-beam or thermal evaporation) [56]. To produce unbent beams, the metal deposition process was broken down into twenty steps to reduce the temperature rise during deposition [56].

In the fabrication process described here, the temperature of the photoresist hard bake may be reduced to decrease the amount of stress in the deposited film. The ultraviolet / hard bake step used for the cantilever fabrication process described in this dissertation used a program with a temperature profile of 120°C for 23 seconds (during which UV light was flashed), 240°C for 120 seconds (with no UV light), and 240°C for 120 seconds with low UV light level. A photoresist film deposited by spin-coating and hard baked under these conditions was found to have a stress of 23.1 MPa (tensile). These results were compared with the stress obtained using a different hard bake program. Using a different recipe at 120°C for a total of 190 seconds, the stress in the deposited film was found to be 9.9 MPa. A hard bake performed at 120°C for 30 minutes in a VWR oven resulted in a photoresist film stress of 9.4 MPa (tensile). By reducing the temperature used during polymer processing, the amount of stress in the film (and thus the amount of curling observed upon release) may be substantially reduced, as shown in Figure 4.16.

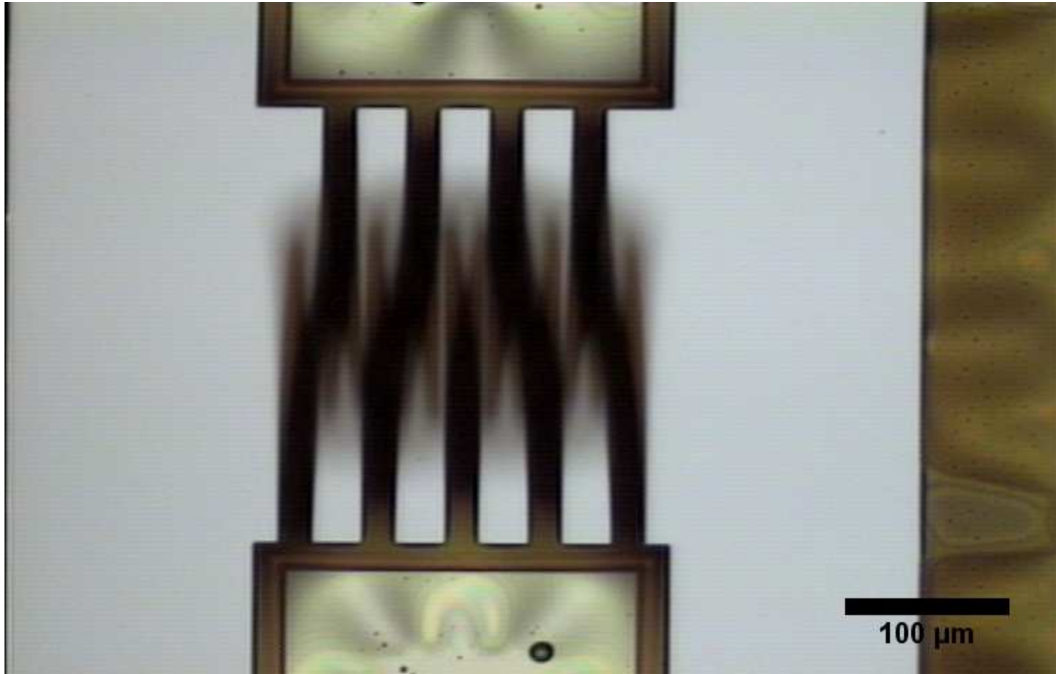

(a) Significant curvature seen for 240°C UV/hardbake processing.

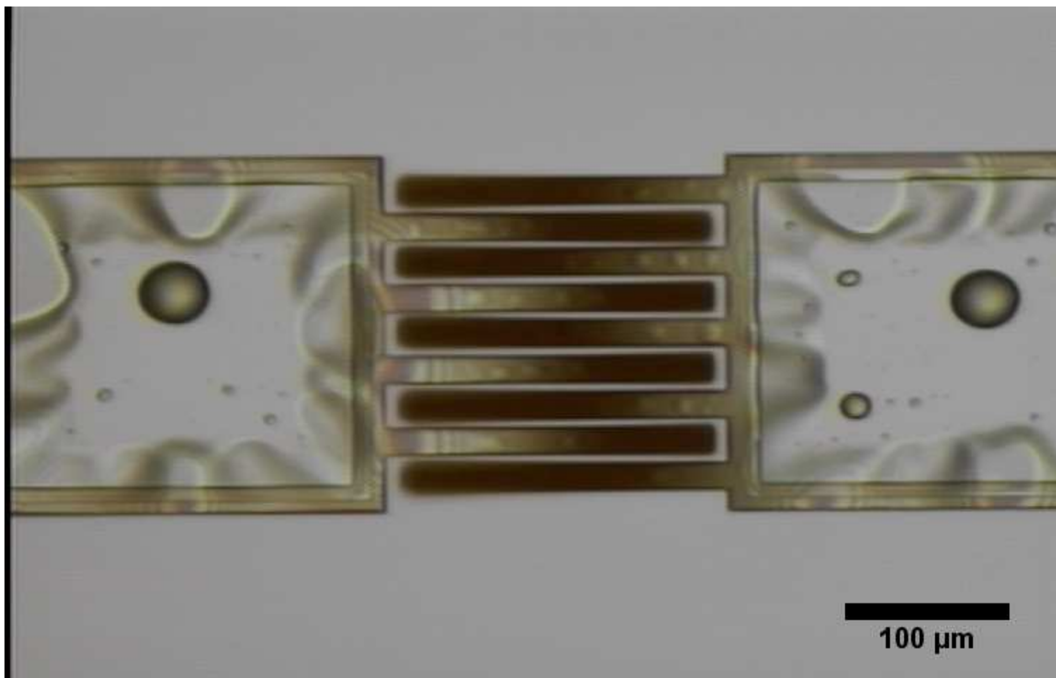

(b) Reduced curvature observed using 120°C hard bake

Figure 4.16: Residual stress is greatly affected by polymer processing temperature. Residual stress may be minimized by lowering the temperature of polymer processing.

Replacing the 240°C UV/bake step with a 120°C hard bake for 30 minutes in a VWR oven was not found to fully eliminate the residual stress. A starting point for further work in this area would include modeling the residual stress to have a linear dependence on the thickness and to perform etching experiments to determine how the curvature in the beam changes as the thickness of the layer decreases. This line of investigation has been clearly described in [60].

Chapter 5

Testing and Evaluation

5.1 Overview

Photoresist-polysilicon cantilever bimorphs were tested using thermal actuation and by stimulation using infrared radiation. A variety of techniques were explored for characterizing and testing released structures, including commercially-available equipment for white light interferometry and laser Doppler vibrometry (LDV), and custom microscope and electronic test setups.

Optical test results demonstrate that the presence of a human finger in the vicinity of the detector was sufficient to cause deflection of the cantilever beam. At a temperature of approximately 37°C, the human body emits a peak wavelength at approximately 9.3 μm. Surface temperature of the body is approximately 33°C which emits a peak wavelength near 9.5 μm [62]. Heating causes the beam to curl downward while cooling causes the beam to curl upward. A temperature change

of less than one degree was sufficient to cause a clearly observable out-of-plane deflection. Rapidly changing the polarity of a thermoelectric to switch between heating and cooling (with ΔT approximately 0.5 K) demonstrated a fast response time that was within the millisecond time range typical of thermal detectors.

Electronic testing involved the read-out of a capacitive signal caused by modulating the cantilever beams with electromagnetic radiation. Capacitive readout was readily achieved without external gain with an output signal that followed the optical signal produced by a chopper wheel. An interdigitated cantilever array that was optically interrogated and used a capacitive electronic readout was found to be highly sensitive, with a dynamic range $> 500:1$, a peak spectral sensitivity from 600 nm to 1.2 μm, and a threshold sensitivity of 2 μW/cm^2. Thermal and optical testing demonstrates the feasibility of high-CTE mismatched cantilever bimorphs for infrared detection applications. These devices could be integrated into systems to allow seeker functionality or into a focal plane array for 2D imaging applications.

5.2 Temperature testing

Due to its nature as an infrared thermal sensor, testing of the polymer-coated cantilever bimorph can be broken down into temperature testing and optical test-

ing. Because absorbed infrared energy is first converted to heat, temperature testing may be used to examine the thermomechanical performance of the sensor design. Optical testing allows the examination of how various wavelengths of light affect the cantilever structure as well as how well the optical energy is converted to heat in the structure.

Temperature testing involves the direct input of heat into the cantilever structure. Temperature testing allows the determination of the direction and magnitude of the cantilever deflection for a given amount of input heat flux. It is also one of the most readily accessible means of determining whether a beam is fully released or still tied to the substrate.

A Peltier element was used to control the input of heat into the cantilever device. The die is placed directly onto the Peltier and the Peltier is used to heat the entire silicon substrate. A schematic diagram of the the temperature testing setup is shown in Figure 5.1. It is important to note that the silicon dioxide anchor acts as a thermal insulator. In order to drive the cantilever using the Peltier element, significantly greater power is needed compared with what would be needed if the polymer-polysilicon beam were directly stimulated. As a result, any sensitivity measurements made using this method will likely significantly underestimate the actual performance from direct heating of the beam.

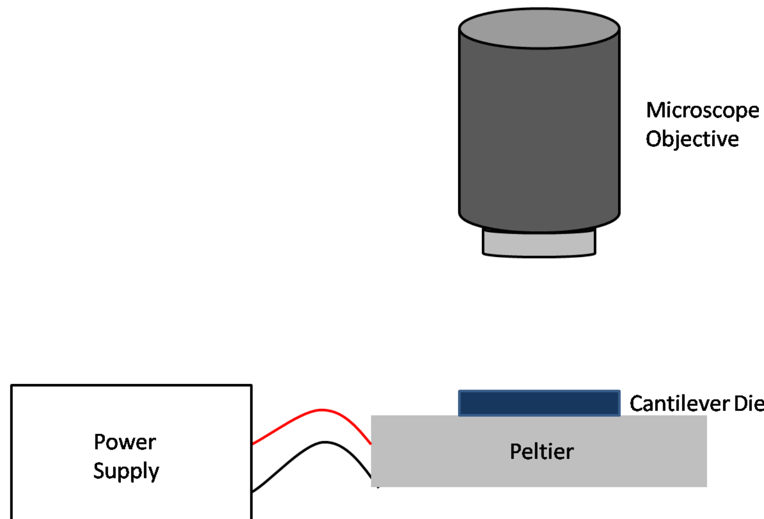

Figure 5.1: Temperature testing apparatus. A Peltier device is used to control the temperature at the surface of the die.

The photoresist-polysilicon beam was found to curl toward the substrate when heated. When the voltage driving the Peltier was removed, the beam returned to its resting state. Driving the Peltier with a negative bias causes the surface to cool; subsequently, the cantilever beam was found to curl away from the substrate. Significant out-of-plane deflections were observed using this testing approach.

Initial temperature testing, which took place in a cleanroom, applied a heat source to the substrate to actuate the beam but did not monitor the temperature at the surface of the Peltier effect device. Frames from a video showing the a cantilever being heated and bending downward are shown in Figure 5.2. Frames showing a cantilever being cooled and bending away from the substrate are shown

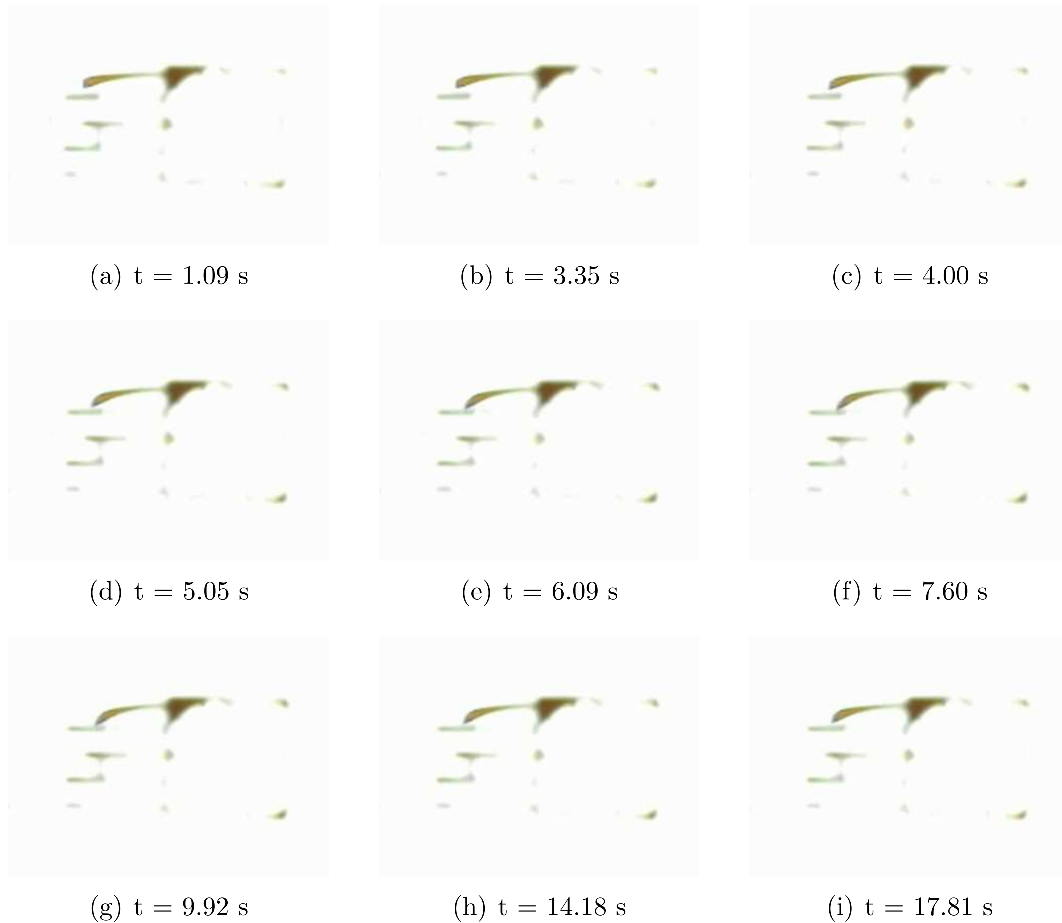

(a) t = 1.09 s (b) t = 3.35 s (c) t = 4.00 s

(d) t = 5.05 s (e) t = 6.09 s (f) t = 7.60 s

(g) t = 9.92 s (h) t = 14.18 s (i) t = 17.81 s

Figure 5.2: Cantilever bending downward due to heating. Beam is able to deflect out of plane a significant fraction of its length, indicating the potential dynamic range of the device. Significant deflection is seen in 5.2(g) compared to 5.2(a). When power to Peltier device is removed, beam returns toward its resting position. as is evident from the difference between 5.2(i) and 5.2(g).

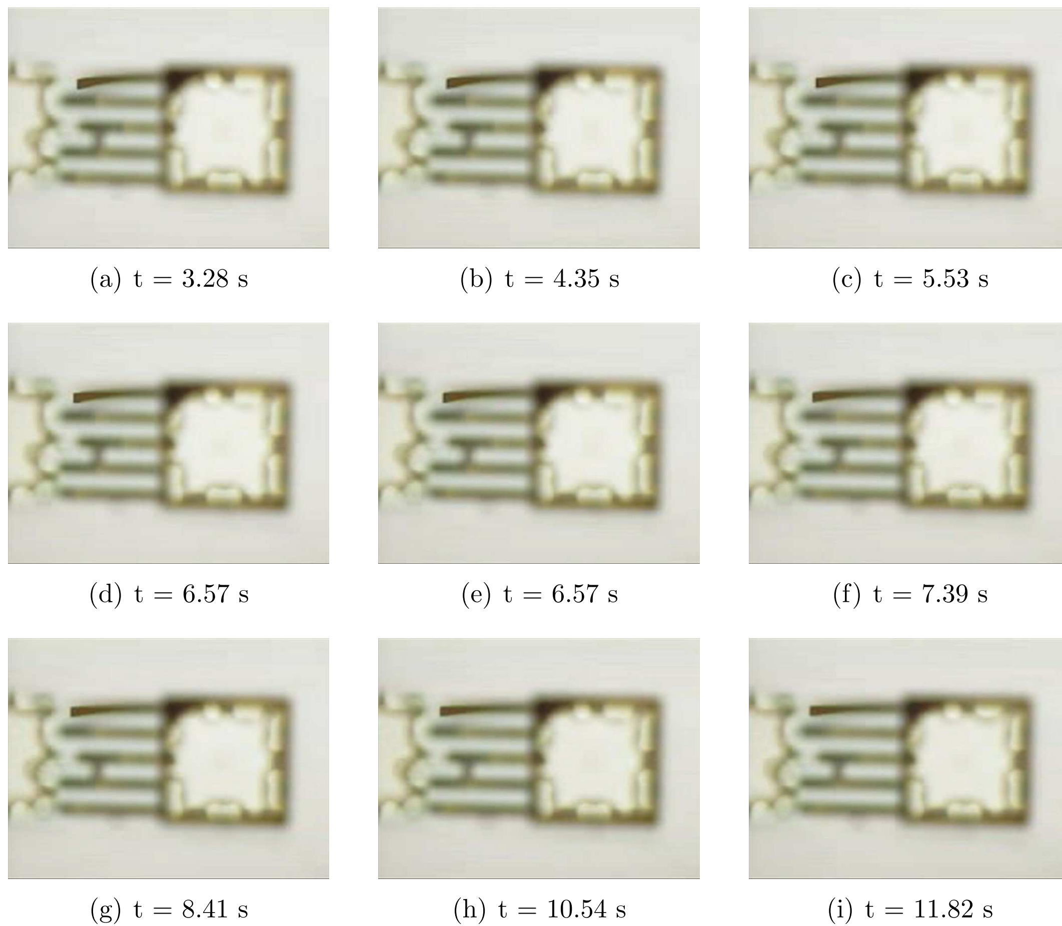

(a) t = 3.28 s

(b) t = 4.35 s

(c) t = 5.53 s

(d) t = 6.57 s

(e) t = 6.57 s

(f) t = 7.39 s

(g) t = 8.41 s

(h) t = 10.54 s

(i) t = 11.82 s

Figure 5.3: Cantilever bending upward due to cooling. Only the beam at the top of each image was released for this particular device.

in Figure 5.3. Mechanical motion is clearly evident when driving the beams with thermal energy.

A thermocouple was used to measure the temperature of the Peltier device in later testing (which took place outside a cleanroom). A cantilever die was set on a thermoelectric which was affixed to a microscope stage, in a setup analogous to that shown in Figure 5.1. The thermocouple was affixed to the surface of the thermoelectric adjacent to the die to allow the determination of the surface temperature. The thermocouple had a resolution of 0.1°C. A light source was focused over the test setup to provide illumination of the stage. A green laser that did not produce a measurable temperature change was focused on the sample. Particulate contamination that lodged onto the device outside the cleanroom produced a fluorescent speckle when illuminated with a green laser. This speckle was clearly visible even under low magnification using an optical microscope, and allowed small displacements in the beam to be readily observed. The thermoelectric was connected to the power supply through a single pole, double throw switch which provided the ability to rapidly switch the bias polarity to change between heating and cooling cycles.

The frames shown in Figure 5.4 shows movement of the beams due to an approximately 0.5 K change in temperature occurring at 1 Hz. Variations in the frames are subtle but are clearly shown in the original video and may also

be observed by carefully observing differences in the fluorescent patterns, such as between the large fluorescent regions in Figure 5.4(c) and Figure 5.4(e). For example, a dark line is visible near the bottom of the large fluorescent spot in Figure 5.4(c) but is not visible in Figure 5.4(e).

5.3 White light interferometry

Due to the fragility of released MEMS structures, it is important to not make physical contact with the structure during device characterization. Therefore, a white light interferometer was used to measure the device profile using optical interrogation, in order to avoid the stylus used in surface profilometers. A Wyko NT3300 interferometry was used for all profilometry measurements of released structures. Measurements were taken using light centered around a wavelength of 600 nm. Measurements were performed in the vertical scanning interference mode, which can measure step heights of up to 5 mm. A 2D and 3D white light interferogram obtained for an interdigitated optical prototype are shown in Figure 5.5.

Although the white light interferogram is able to discriminate the boundary characteristics of the cantilever features, it is not an ideal measurement tool because the structures consist of more than one material and the cantilever beams

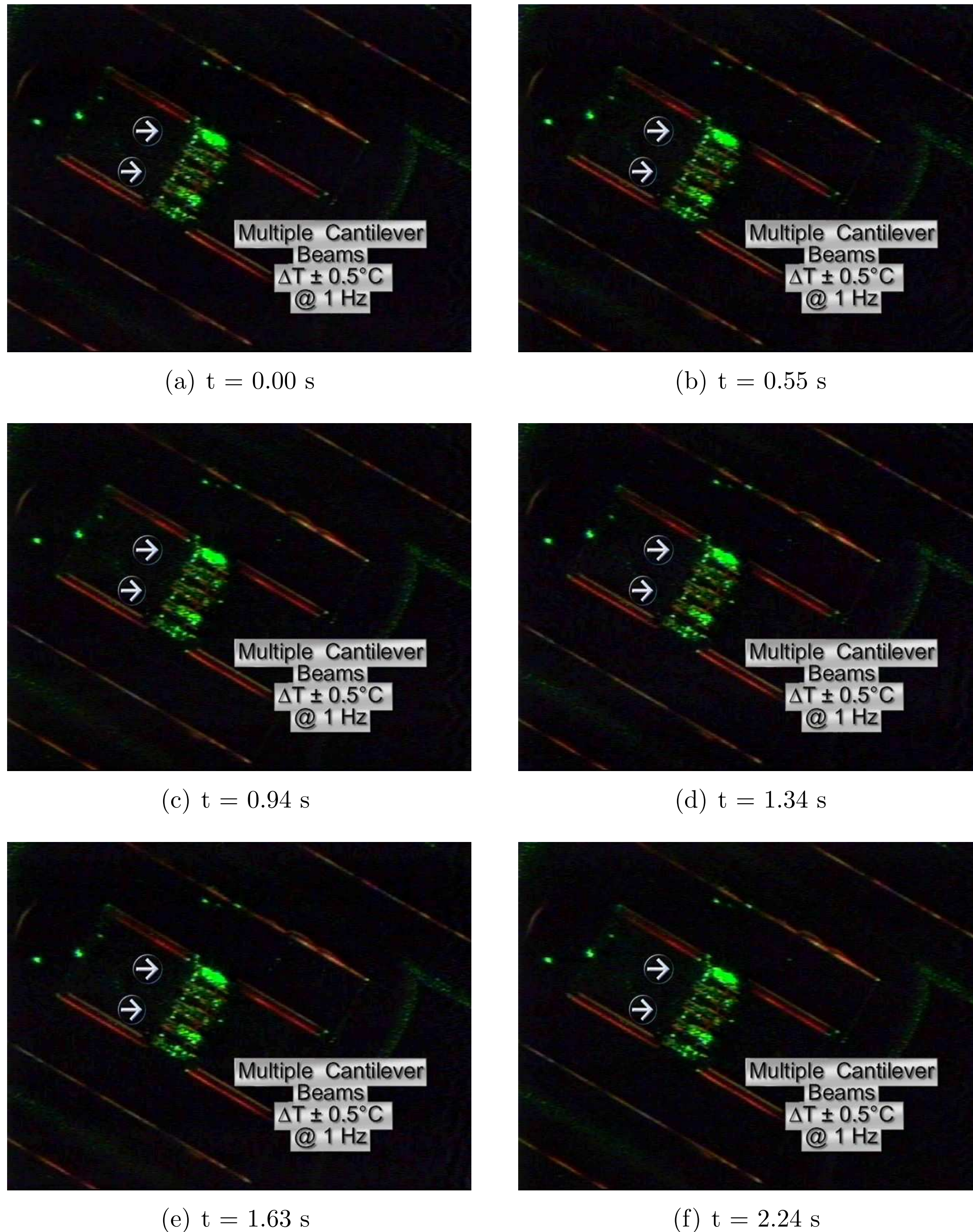

(a) t = 0.00 s

(b) t = 0.55 s

(c) t = 0.94 s

(d) t = 1.34 s

(e) t = 1.63 s

(f) t = 2.24 s

Figure 5.4: A thermoelectric heater allowed heating and cooling of the die. A green laser illuminated surface contamination which autofluoresces and allows movement in the beam to be readily seen under a microscope. Switching between heating and cooling takes place at approximately 1 Hz which produces a change in temperature of approximately 0.5°C.

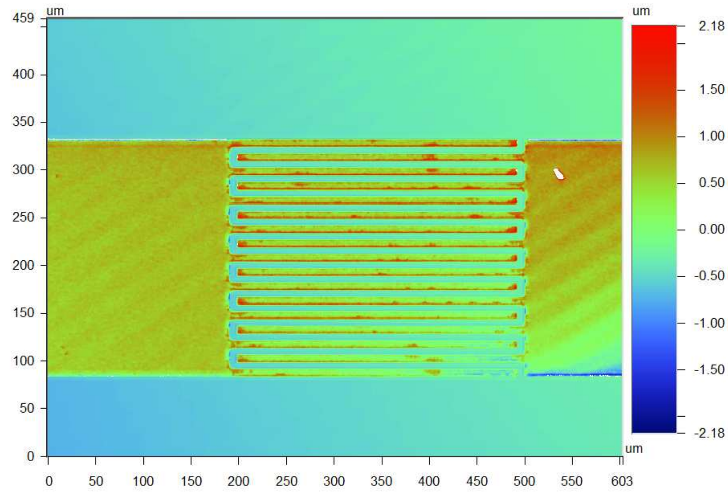

(a) 2D white light interferogram.

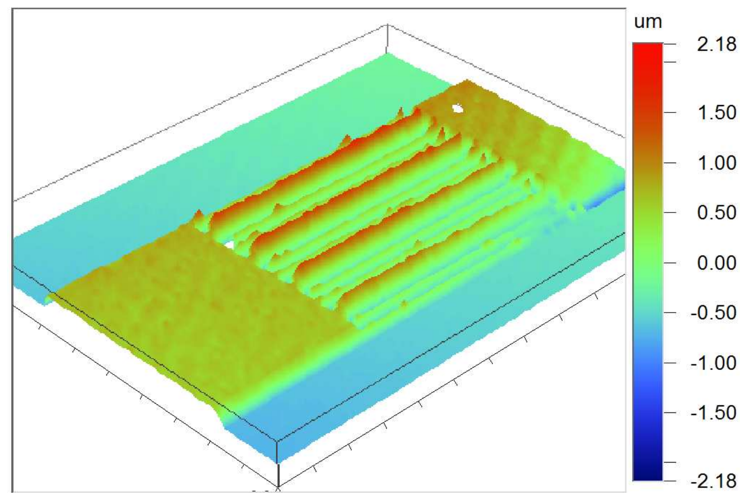

(b) 3D white light interferogram.

Figure 5.5: White light interferogram for interdigitated cantilever optical prototype.

will respond to the light used during the measurement. Time lapse images cannot be made as light (whether internal or external to the machine) is used to

stimulate the cantilever device. Due to these disadvantages, a capacitive readout system that measures the deflection of the beam electronically was investigated for further device characterization.

5.4 Electronic Readout

In nearly all end-user applications, an electronic readout is desirable for its ease of integration into larger subsystems and ability to be digitally processed. Because the bulky setup required for optical readout techniques is prohibitive for real-world applications, a capacitive readout method was investigated whereby deflection of the beam produces a change in capacitance, and the change in capacitance is converted into a change in voltage. In this setup, infrared radiation is converted to heat, heat produces deflection, deflection modulates capacitance, and the changing capacitance is sensed and converted to a voltage. The capacitive test setup used the highly sensitive MS3110 universal capacitive readout IC from Irvine Sensors. A capacitance change was readily measured between an array of interdigitated cantilever beams that were stimulated with electromagnetic radiation. Furthermore, the output signal was found to have a spectral sensitivity, based on tests using a variety of optical and infrared filters.

5.4.1 Irvine Sensors MS3110

The Irvine Sensors MS3110 capacitive readout chip converts capacitance to voltage according to the transfer function:

$$V_o = Gain * V_{2.25} * 1.14 * \frac{CS2 - CS1}{CF} \tag{5.1}$$

where $CS1$ and $CS2$ are the sense capacitors, and CF is the feedback capacitance around the input trans-impedance amplifier.

The chip features a capacitance resolution of 4.0 $aF/\sqrt{Hz}$ and can operate in single or differential mode.

In the capacitive test setup, two interdigitated cantilever arrays form the plates of a capacitor which are attached to $CS1$ on the MS3110 test board.

This chip is powered with a +5V DC voltage and this limits the output signal between rails of 0 V and 5 V.

5.4.2 Capacitive test board

The capacitive test board contains all of the electronic circuitry necessary to drive the Irvine Sensors MS3110 capacitive readout chip. Power is supplied to the chip through banana plugs which are input into the printed circuit board. The

Functional Block Diagram:

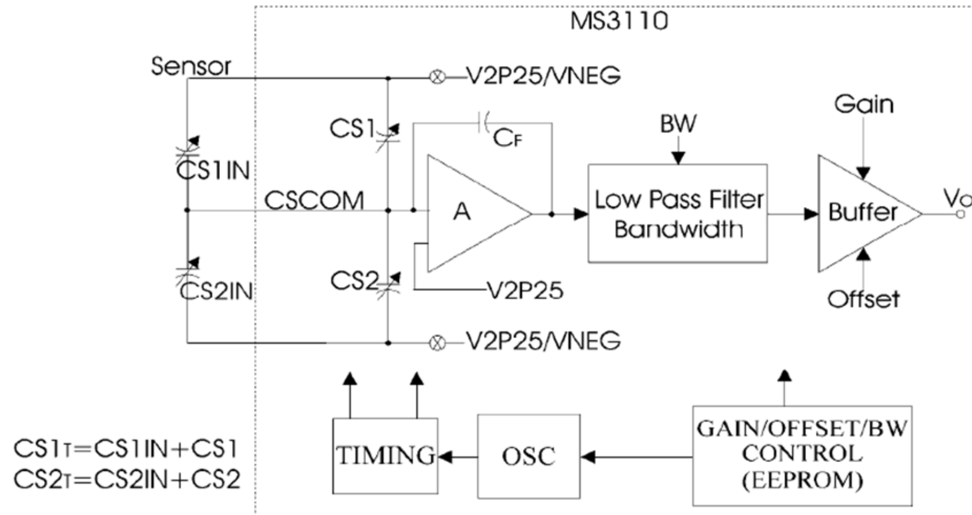

Figure 5.6: Irvine Sensors MS3110 Block Diagram.

output of the chip is fed off-board through a shielded BNC connector. A cutout in the board exists in which to mount the die or to mount a subboard.

The subboard allows the die to be mounted along with a temperature control element (thermoelectric) and heat sink for temperature stabilization and can also be adapted to perform vacuum packaging. A photograph of the subboard containing a die, thermoelectric (not shown), and copper block (not shown) attached to the capacitive readout board is shown in Figure 5.9.

5.4.3 Capacitive test subboard

The capacitive test subboard was developed in order to allow flexibility in testing of individual dies under a variety of conditions. The board was design to

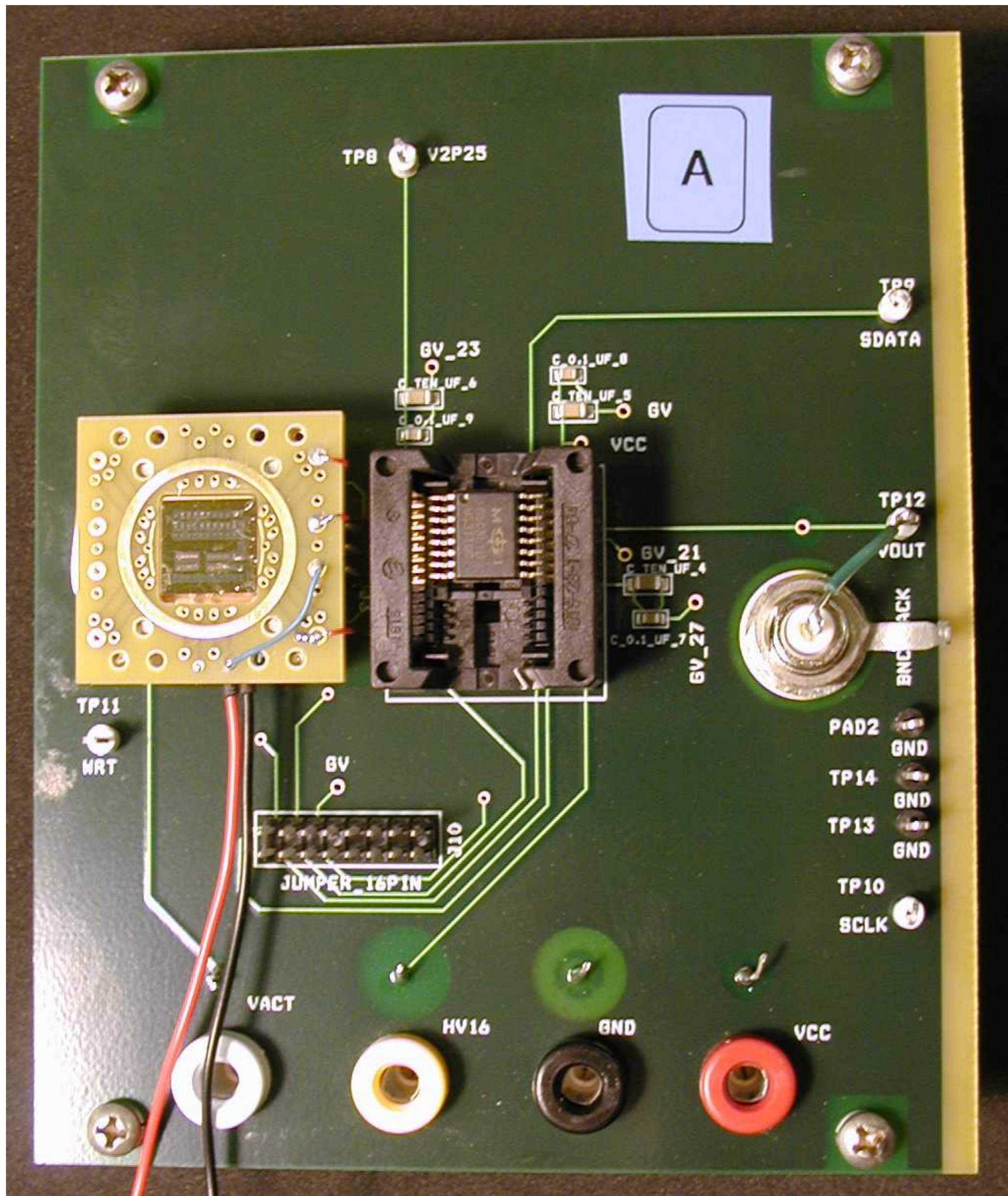

Figure 5.7: Photograph of capacitive test board.

allow the integration of a thermoelectric heater to directly stimulate the device with heat. It was also designed to allow vacuum encapsulation of the device in order to test the effect of reduced pressure on device performance.

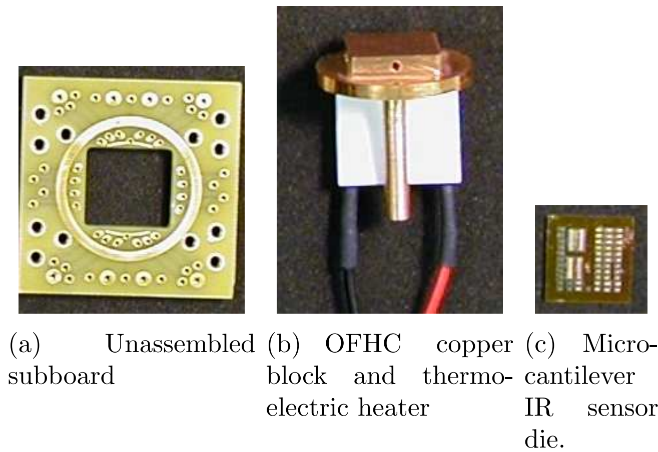

(a) Unassembled subboard (b) OFHC copper block and thermoelectric heater (c) Microcantilever IR sensor die.

Figure 5.8: Capacitive test subboard assembly components.

Die attach was performed using a low outgassing epoxy (Vacseal, SPI Supplies, West Chester, PA). The die was affixed to an oxygen-free high conductivity (OFHC) copper block that was mounted to the subboard using standoffs. Individual dies are wirebonded to the subboard and then the subboard leads are soldered directly to the capacitive readout board. Wire bonds were made using a West Bond 7400B wirebonder with 0.00125" diameter Al-1% Si wire. For all devices measuring capacitance as the output signal, parasitics are of primary concern.

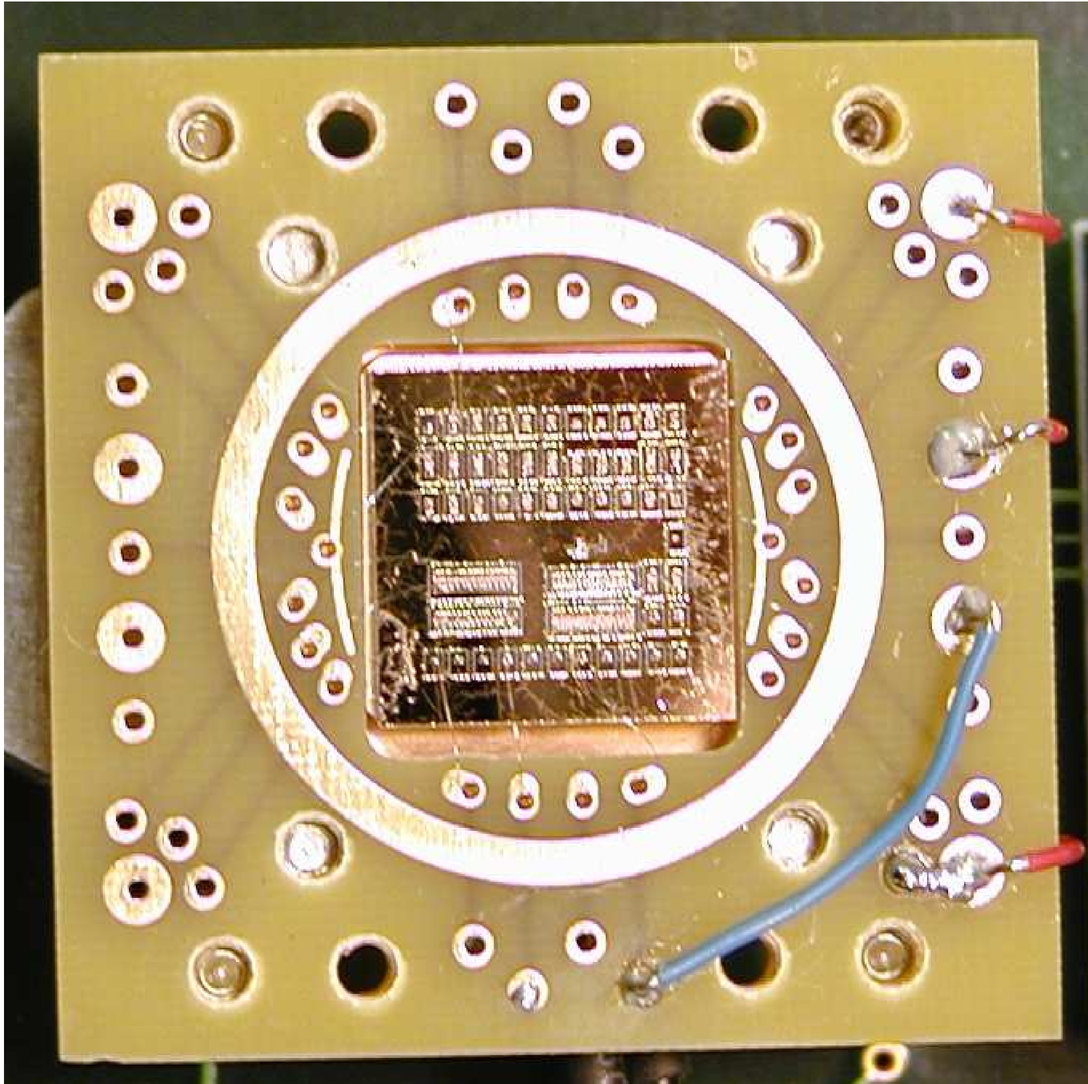

Figure 5.9: Photograph showing cantilever die attached and wirebonded to capacitive subboard.

5.4.4 Capacitive testing setup

A halogen light bulb connected to a Variac power supply was used as the primary illumination source. A chopper wheel operating between 10-40 Hz was used to produce a pulsed optical signal on the detector surface. Data was sampled at 4 kHz and downsampled to 1 kHz using a 4-point moving average. An infrared camera and a visible camera were focused on the die to allow imaging of the device and the monitoring of temperature at the surface throughout the test process. Data was collected using LabVIEW (National Instruments, Austin, TX). A KRS5 lens, which has transmission from 600 nm to 40 μm, was used to focus and filter light in the optical path. A photograph of the capacitive test setup showing the capacitive test board vertically mounted in the path of a halogen light source with visible and infrared cameras focused on the detector is shown in Figure 5.10.
A rear view of the capacitive test board affixed to the aluminum mounting fixture is shown in Figure 5.11. The reflection of the cantilever detector and subboard is clearly visible in the lens of the infrared camera.

5.4.5 Capacitive test results

Measurements of capacitance at the output of the detector demonstrates that the microcantilever detector clearly responds to electromagnetic radiation. Millions of cycles were run indicating the resistance to fatigue and the long-term

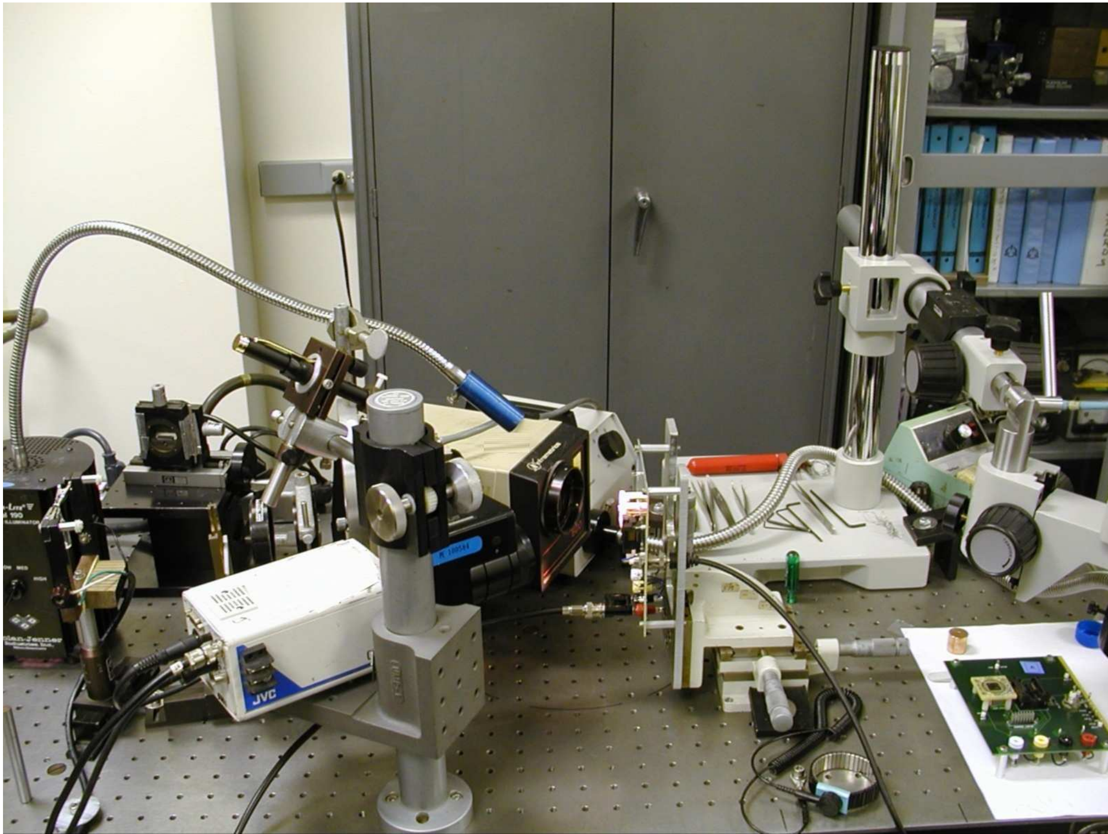

Figure 5.10: Optical bench setup for capacitive testing.

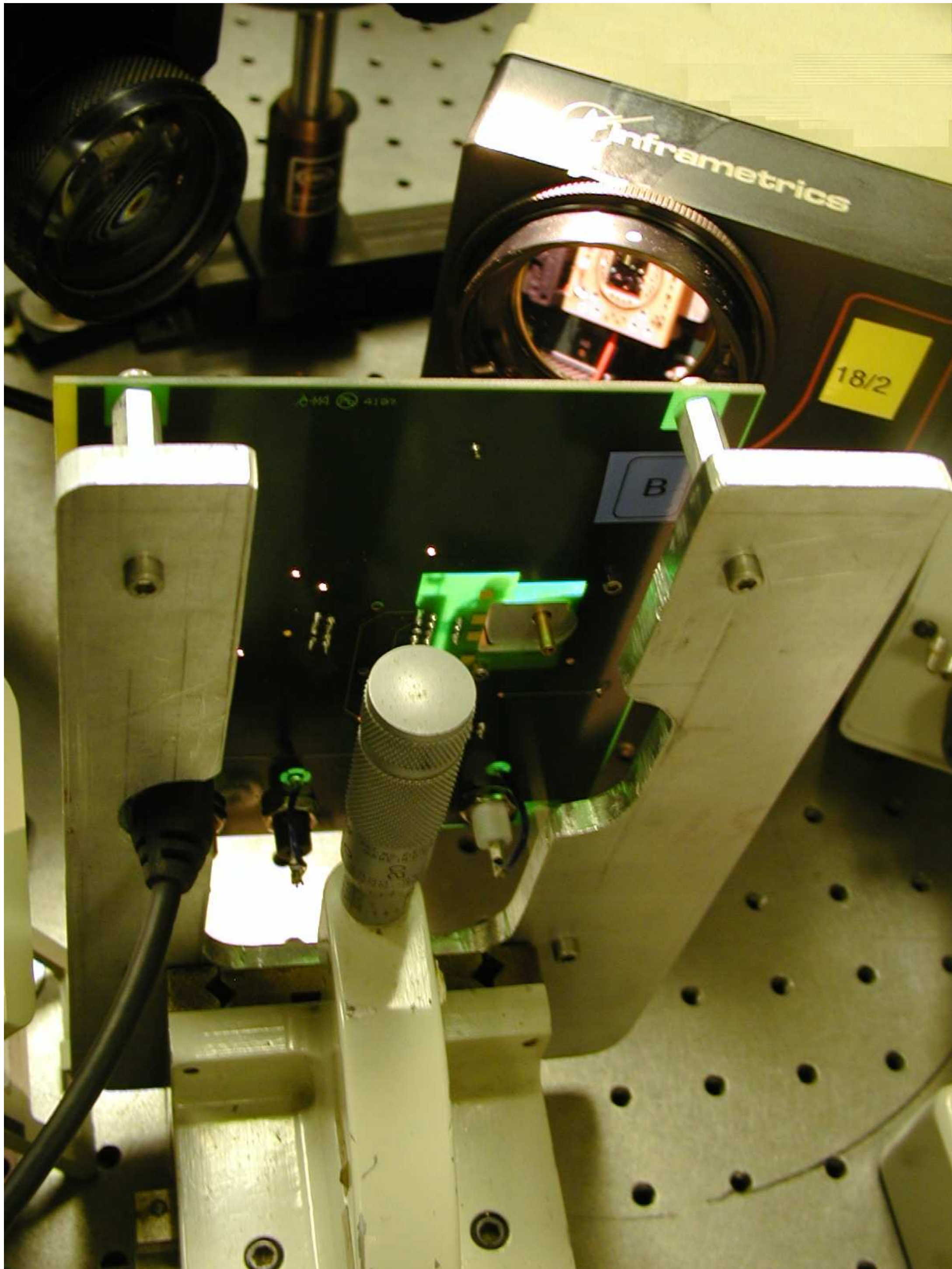

Figure 5.11: Die seen in lens of IR camera.

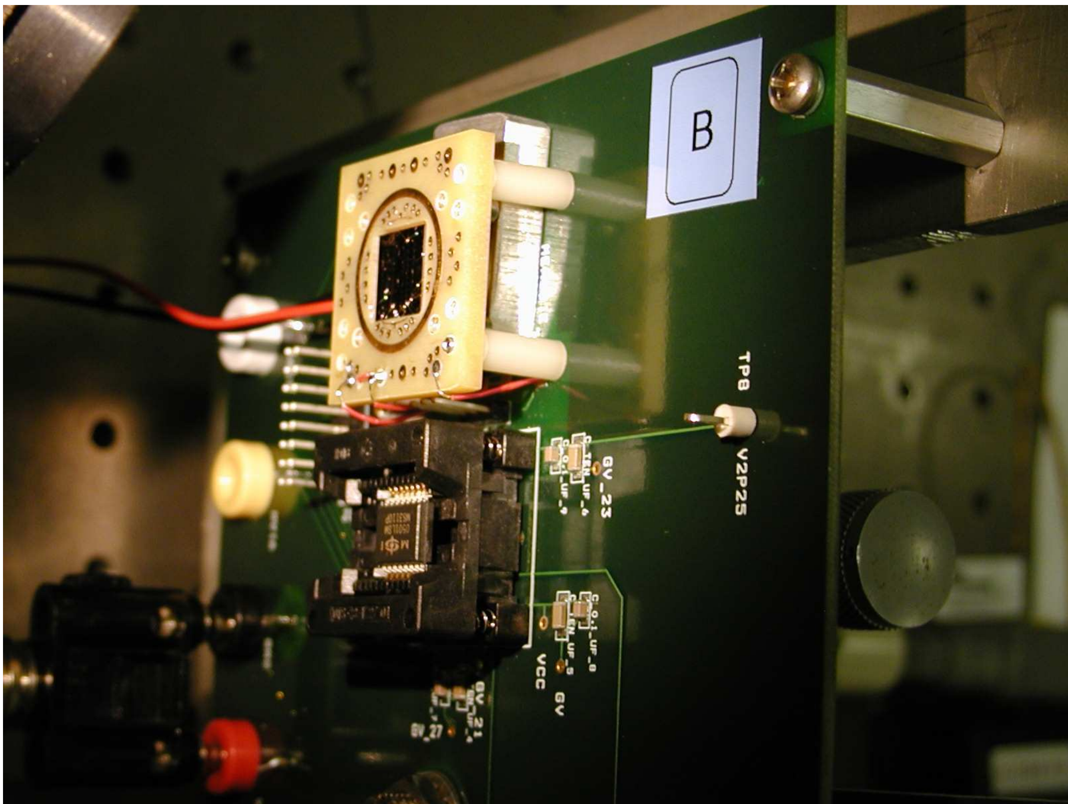

Figure 5.12: Close up of capacitive test board mounted on aluminum test fixture.

viability of the sensor. Focusing the light source on an area of the die away from the wirebonded device produced no output signal, which verified that the observed response was due to the interaction of the stimulus with the wirebonded device.

The capacitive output signal successfully tracked the halogen light when a chopper wheel periodically blocking the optical light path, as shown in Figure 5.13. 60 Hz flicker in the halogen light source, which is not evident to the naked eye, was also seen by the detector. Blocking the light path with a paper card eliminated the signal seen by the detector, as shown in Figure 5.14. The output signal successfully tracked the frequency of the chopper wheel as it was modulated, as is demonstrated in Figure 5.15. Responses in the capacitive detector were observed for chopping frequencies from 0 Hz (DC) to 250 Hz. Higher frequencies were not tested because of the sampling rates used in the data acquisition system (4 kHz downsampled to 1 kHz with a 4-point moving average) in order to prevent aliasing of the output signal.

To investigate the sensitivity and dynamic range of the detector, the power to the Variac was adjusted lower in order to reduce the output voltage of the signal. When the voltage level was sufficiently low (< 0.5 V), an external 10x amplifier could be used to view the signal and clearly discriminate it from the noise. Lowering the output voltage was necessary such that external amplification did not reach the rails of the chip. Repeating this process further allowed the use of an

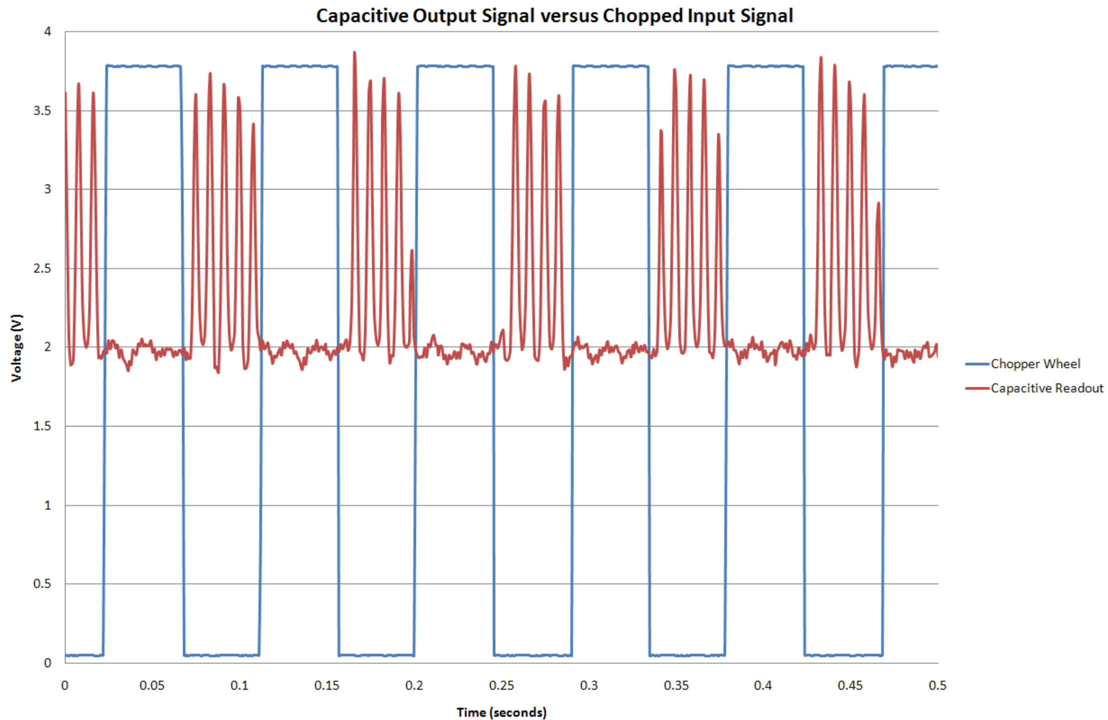

Figure 5.13: Plot of output voltage signal from capacitive readout chip versus chopped input light signal from halogen bulb. Output successfully tracks input. Multiple spikes within signal are indicative of influence of 60 Hz noise on the light source.

external 100x amplifier to view the low signal level and distinguish it from the noise. This allowed the voltage level of the Variac to be reduced from approximately 70 V to less than 10 V, and this reduction greatly diminished the power coming from the halogen lamp. Changing the voltage lowers the temperature of the lamp, which in turn reduces the total energy radiated in proportion to T^4 according to the Stefan-Boltzmann law.

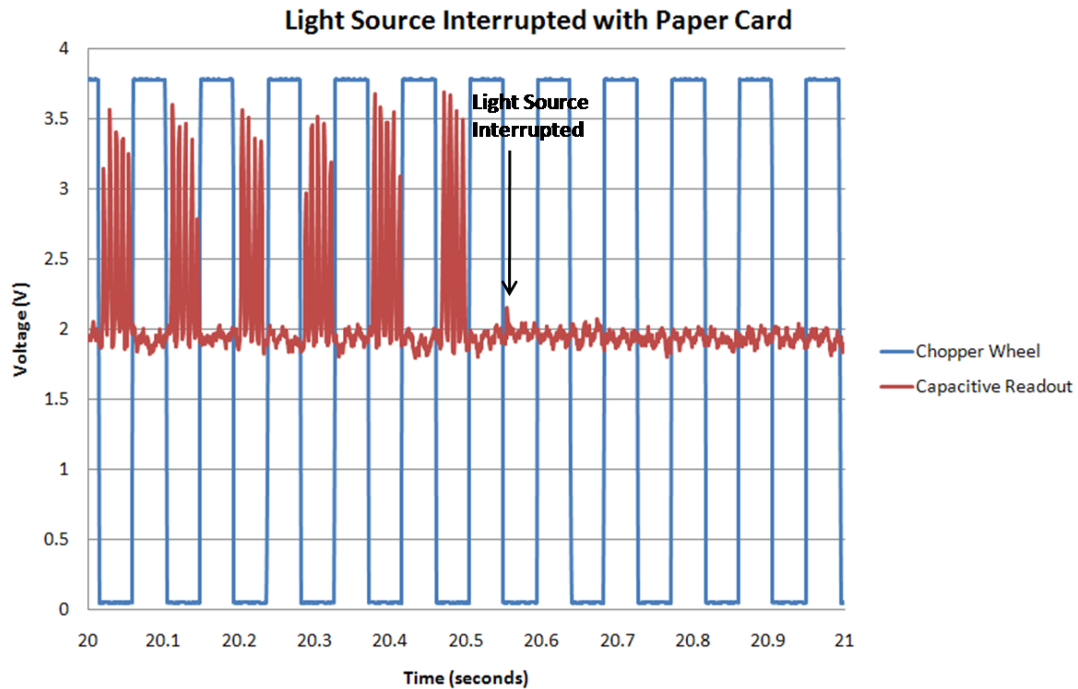

Figure 5.14: Output signal eliminated when light beam is interrupted with a paper card.

At this reduced optical power level, the light emitted from the halogen lamp source could just barely be detected with the human eye and the chopped light incident on the MEMS detector could not be seen by the human eye or by a visible camera focused on the detector. Thus, this process diminished the optical power by many orders of magnitude without eliminating the output signal of the detector. An Inframetrics Model 600L LWIR camera looking in the 8-12 μm band with a resolution of 100 mK could not detect reflected and emitted energy from the surface of the MEMS cantilever die even as the MEMS die was able to detect

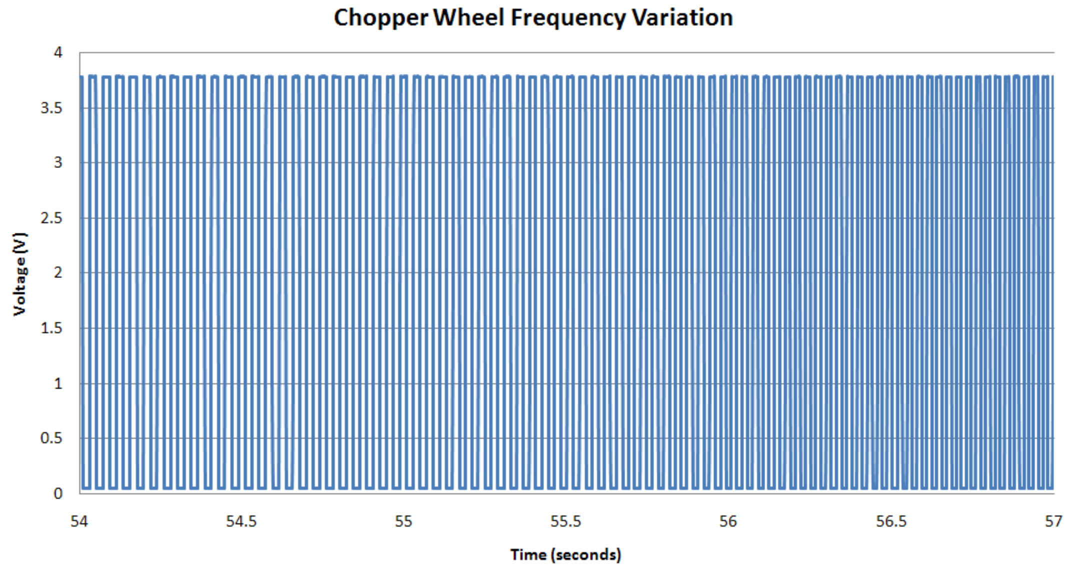

(a) Chopper frequency variation

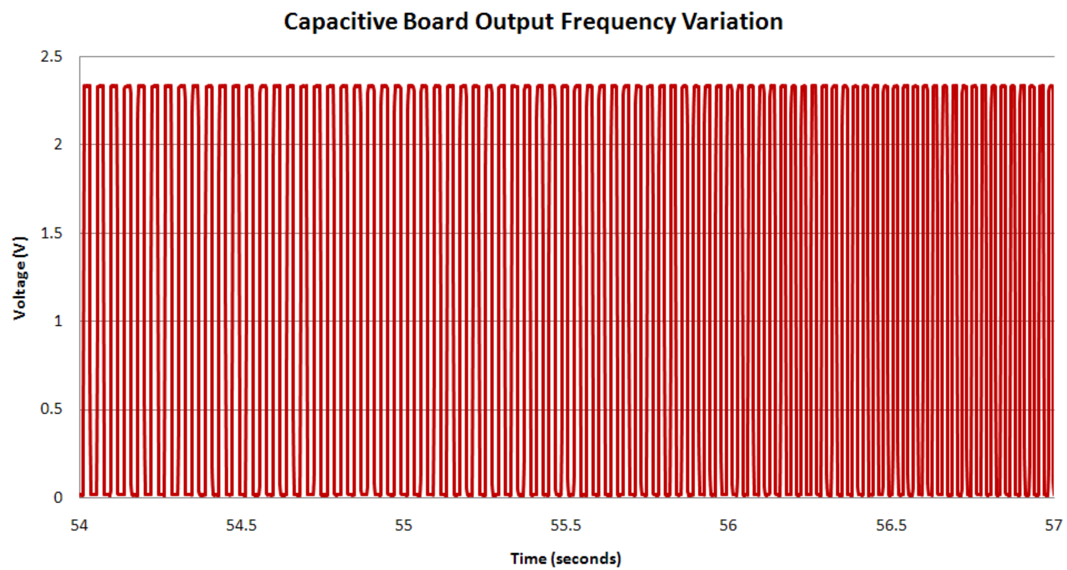

(b) Capacitive board frequency variation

Figure 5.15: The output signal successfully tracks changes in the frequency of the chopper.

a signal from the halogen light source. In addition, with the halogen light source off and the detector signal maximized, switching the fluorescent room lights on and off was enough of a stimulus to be clearly seen in the output signal.

A dynamic range >500:1 was achieved using the capacitive readout test board. Dynamic range is defined as the ratio of the maximum detectable signal to the minimum detectable signal. Dynamic range was measured by adjusting the voltage of a Variac (Powerstat Variable Autotransformer) from a level which made the chip saturate down to a level that could not be distinguished from the noise. At low signal levels, 10x and 100x amplification was used to enhance the signal so that the signal could be seen by the data acquisition card. The high dynamic range of the microcantilever sensor allows for optical power to be detected over many orders of magnitude.

Numerous tests were performed to distinguish whether the response was due to photons incident on the detector or due to the thermal radiation caused by the light sources. Quickly turning off the Variac after having it on for a sustained duration eliminated the presence of photons from the source while still maintaining a warm surface at the bulb. Even in the absence of photons, the detector would respond to the chopped infrared radiation coming from the warm bulb. A frozen aluminum block placed in the vicinity of the detector was observable at the output of the capacitive readout board.

5.4.6 Noise

In the absence of an optical stimulus, the output of the capacitive readout will drift due to thermal fluctuation in the room and noise in the environment. The graph in Figure 5.16 shows the drift over a ten minute time period and it is clearly evident that the drift is less than 0.01 V. The mean of the output signal is 1.3525 volts and the standard deviation is just 198 μvolts. The low noise level allows signals caused by low levels of electromagnetic radiation to be clearly seen at the output of the detector.

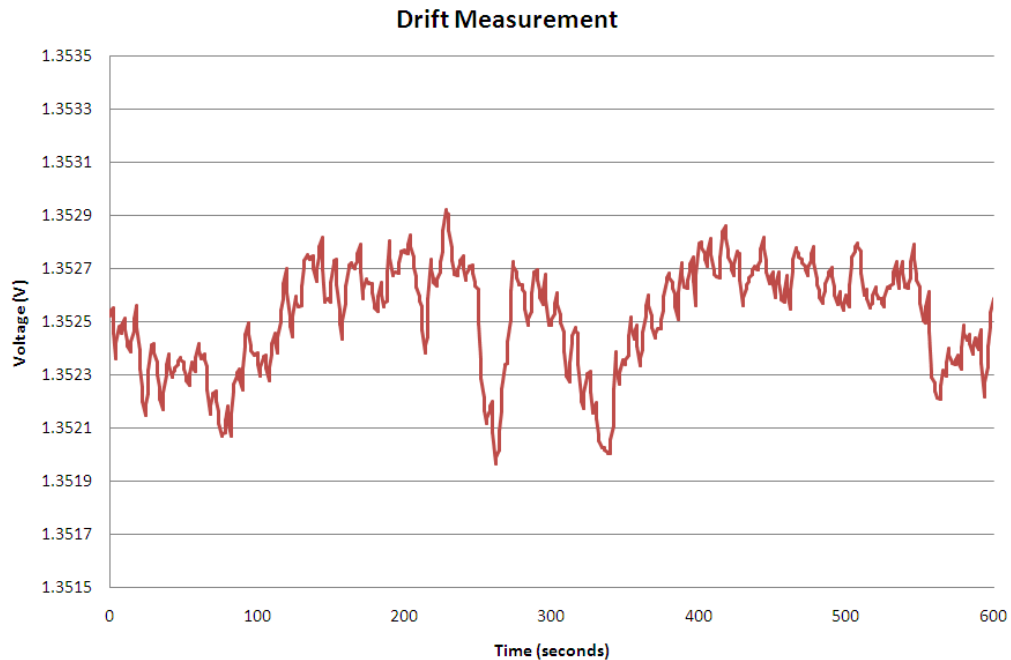

Figure 5.16: Voltage drift in the absence of a stimulus.

5.4.7 Time response

The polymer-based microcantilever infrared sensor was found to have a fast time response, with a rise time < 3 ms and a fall time < 1 ms. Data was collected at 1 kHz and therefore the minimum time change that could be resolved with this data acquisition rate was 1 ms. A graph showing the voltage transition of the chopper wheel signal and the voltage transition of the cantilever output signal is shown in Figure 5.17. Although the voltage output saturates near 5 V, it is clear that the response time is rapid and more than sufficient for infrared imaging which generally takes place at frames rates of 30 Hz.

5.4.8 Capacitive threshold effect

On one of the tested interdigitated cantilevers, a threshold effect was observed whereby no output response was seen until a sufficiently large intensity was input onto the detector. The change between the “off” state and the “tracking state” was abrupt. A voltage of 70 V dialed into a Variac and used to modulate the intensity of a Halogen light source was found to elicit no response on this particular detector whereas a voltage of 73 V was clearly observable at the output of the capacitive readout board. This threshold effect is likely due to the residual stress in the polymer thin film which produces the initial out-of-plane curvature.

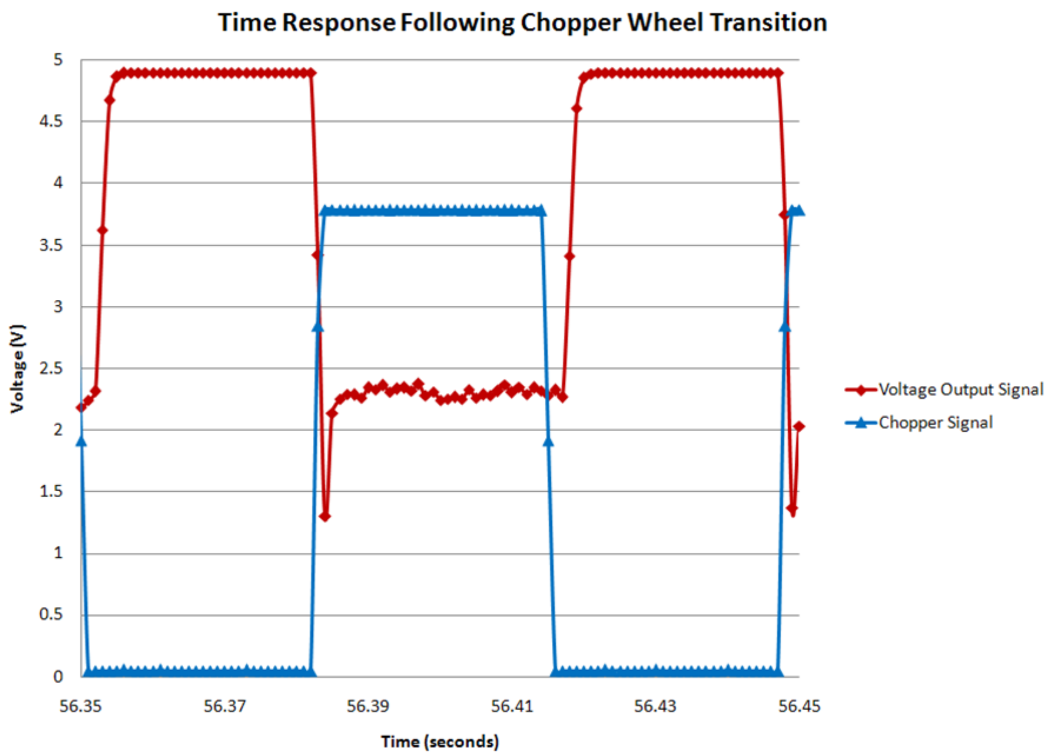

Figure 5.17: Time response following chopper signal transition.

Residual stress causes the beam to initially curl upward which would cause the capacitive gap to increase. If the gap became sufficiently large, the capacitance will diminish to a point where it is unobservable by the capacitive readout chip. This observation is consistent with the parallel-plate model for capacitance where the capacitance is a nonlinear function of the distance between the plates. Similar testing on an identical structure on a different die from a wafer that was processed at a lower temperature was found to not have this thresholding effect, and this may result from the use of a lower polymer-processing temperature to reduce the residual stress, which produce less initial out-of-plane curvature upon release.

5.4.9 Determination of spectral sensitivity

A number of filters were placed in the light path to determine the spectral sensitivity of the detector. The RG-610 (Melles Griot 03 FCG 101) is a near-IR filter that passes wavelengths longer than 610 nm. The Melles Griot 03 SWP 019 interference filter has a passband from 440-650 nm.

The RG-610 filter provided little attenuation in the output voltage signal produced by the detector indicating that the sensor has responsivity at a wavelength longer than 610 nm. When the 03 SWP 019 filter was put in the optical path, the output signal of the detector was lost, indicating that the sensor is not sensitive

to wavelengths between 440-650 nm. Zinc selenide has transmission from 600 nm to 20 μm. Germanium has transmission from 1.8-23 μm.

Based on experiments with numerous filters, it was determined that the detector shows a peak spectral sensitivity in the wavelength band ranging from 600 nm to 1.2 μm. This wavelength range is below that detected by Fourier transform infrared spectroscopy and therefore it would be instructive to perform near-IR spectroscopy on the photoresist to determine its absorption profile over this wavelength range and correlate it to these results.

5.4.10 Determination of threshold sensitivity

Light sources must be calibrated and their intensity computed in order to determine the minimum sensitivity of the detector. A Feit 100 W, 120 V halogen bulb and a Dolan-Jenner Model 190 fiber optic illuminator were used in these experiments. An Optronic 730A Radiometer with Optronic 730-5C UV Enhanced Silicon Detector and Optronic Radiometric Filter were used to measure the intensity of the light sources.

The intensity of the Feit halogen bulb was measured at various voltages up to the limits of the Optronic detector. A plot showing the intensity of the bulb as the voltage to the halogen lamp is varied is shown in Figure 5.19.

(a) Zinc selenide (ZnSe)

(b) Quartz

(c) Germanium (Ge) 5 dB

(d) Neutral density filter 1 dB

(e) RG-610

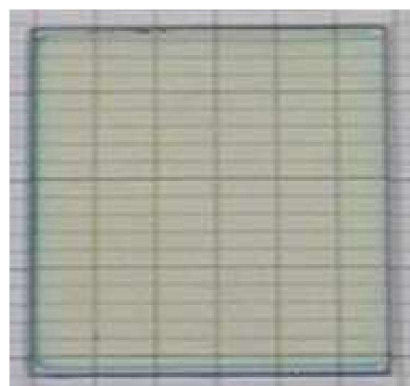

(f) 03 SWP 019

Figure 5.18: Filters used to determine spectral sensitivity.

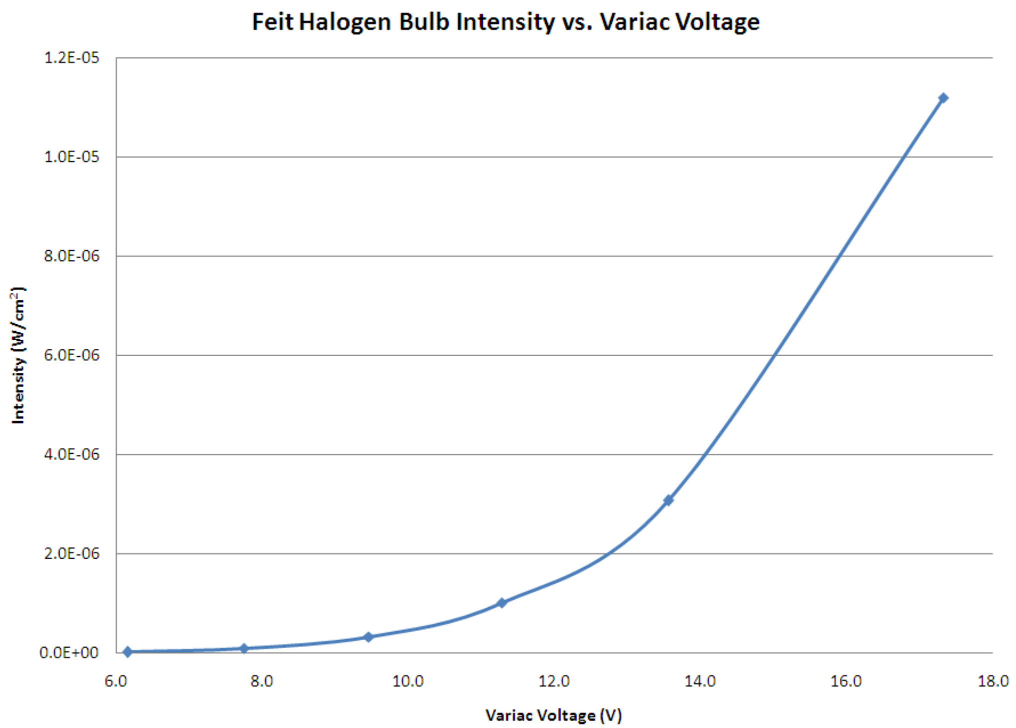

Figure 5.19: Feit halogen bulb intensity versus Variac voltage.

The Dolan-Jenner Industries Fiber-Lite Model 190 Fiber Optic Illuminator was set to medium and placed 550 mm away from the detector. The value of this light source as measured with an Optronic 730A Radiometer/Photometer was 2×10^{-4} W/cm^2 and was readily observed with the cantilever IR detector.

Neutral density filters with NDF ratings of 0.0, 0.1, 0.3, 1.0 and 2.0 were used to determine the effect of optical power density on the IR detector, and compared with their effect on the incident fiber optic light source which is driven by a photodiode. Neutral density filters attenuate the optical signal by a specified power independent of wavelength, and the transmission is defined by:

$$\%transmission = 10^{-NDF} \tag{5.2}$$

where NDF is the neutral density filter rating. An NDF 2.0 neutral density filter that decreases the power of the fiber optic light by a factor of 100 produced an attenuated signal that could still be observed by the IR detector. The attenuated signal corresponds to an intensity of 2×10^{-6} W/cm^2. For this test, the fiber optic light source was blocked until the neutral density filter was inserted into the optical path.

The effect of various neutral density filters inserted into the optical path is shown in the log plot of Figure 5.20. The various power levels resulting from the

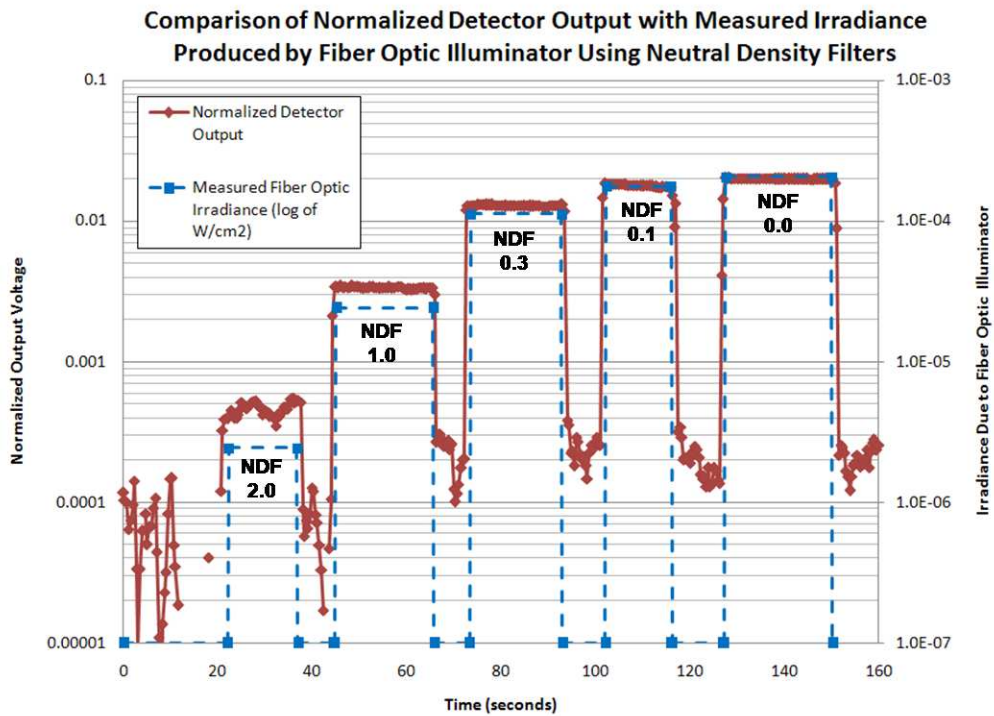

Figure 5.20: Effect of neutral density filters on normalized output voltage. Output voltage has been normalized to the measured irradiance produced by a photodiode in a fiber optic illuminator with no neutral density filter in place (NDF 0.0) to allow direct comparison between measured irradiance and voltage output.

neutral density filters are clearly seen as sustained drops in the capacitive output signal when the filters are inserted into the optical path. The signal from the cantilever detector decreases as the rating of the neutral density filter increases, and follows the irradiance produced by the photodiode in the fiber optic lamp.

The output signal was normalized by defining the noise as 1 and then subtracting out the offset to center the noise at 0. A log plot was then produced and the output voltage scaled such that the output voltage of the detector for the fiber optic illuminator (without an neutral density filter in place) corresponded to the irradiance of the fiber optic illuminator photodiode as measured with the Optronic Radiometer. Normalization allowed direct comparison of the effect of the neutral density filters on the measured irradiance on the detector due to the fiber optic illuminator with the output voltage produced by the detector. Results show a strong correlation between irradiance on the detector and the output voltage of the detector.

Chapter 6

Conclusion

In this dissertation, a design for a novel, polymer-based infrared thermal detector was proposed, developed, fabricated, and tested. With nature as a proof-of-concept, the biomaterial chitin (found in the infrared sensitive organ of the jewel beetle *Melanophila acuminata*) and its deacetylated form chitosan, was investigated as an infrared material. In realizing that the use of such a material would ultimately depend on its compatibility with modern manufacturing technology, significant experimentation was invested in the development of a photolithographic patterning process such that low-cost batch fabrication could be achieved. In addition to its usefulness in the development of polymer-based IR sensors, the photolithographic patterning process may be successfully employed in a broad range of biology-based applications, for example in patterning proteins on a chip or in the development of biosensors using DNA or RNA.

Based on the available literature on the infrared detection mechanism in the jewel beetle *Melanophila acuminata*), a polymer-based optomechanical microcantilever sensor prototype was developed. For the initial prototype fabrication, photoresist was chosen over chitosan primarily for its commercial off-the-shelf status (which significantly improves its consistency run to run) and lack of a stress-temperature hysteresis. Furthermore, photoresist has favorable material properties such as a high coefficient of thermal expansion, making it a good compromise for an initial prototype material. The selection of photoresist also slightly simplified the fabrication process by eliminating a spin-coating, etching and photoresist removal step. Optical testing demonstrated movement of the beams due to direct stimulation by heat using a thermoelectric as well as by the infrared radiation generated from a human finger placed in the vicinity of the detector. Results of capacitive testing for a detector with an electrical readout demonstrate a significant response to electromagnetic radiation with a threshold sensitivity of 2 μW/cm^2, and dynamic range $>$ 500:1.

The topics discussed in this dissertation form an area ripe for further investigation. Recommendations for further topics of investigation include:

- **Reduction of beam curvature upon release**

  To reduce residual stress in the released beam, adjustments may be made to the thermal processing steps. In particular, the temperature and time of

the photoresist hard bake may be reduced and the polysilicon film may be annealed following chemical vapor deposition. Furthermore, once released, beams may be annealed to further reduce stress. Methods for reducing curvature of released beams caused by residual stress gradients, for example, by annealing films (polysilicon), lowering the temperature of polymer processing (decrease temperature in hard bake step. These modifications should generate significantly less out-of-plane deflection upon release.

- **Replace photoresist with alternative polymers**

  Another area to pursue is to replace photoresist as the infrared, polymer absorbing layer with alternative materials for specific wavelength sensitivities. This may be accomplished using the photolithography process described in Chapter 2. Photoresist may be replaced with alternative polymers such as PMMA, polyimide, chitosan and chitin. Polyimide has a high temperature stability which allows the use of rapid thermal annealing to anneal out the stress and reduce the beam curvature following release.

- **Correlation of detector spectral sensitivity to FTIR spectrum**

  Determination of spectral sensitivity using IR filters and correlation to polymer FTIR spectrum.

- **Compare LDV displacement measurements with capacitance measurements**

  Laser Doppler Vibrometry (LDV) is a remote sensing technique used to measure the vibration of a mechanical structure [63]. Laser Doppler Vibrometry uses the Doppler effect to measure vibration. The Doppler effect relates a change in velocity to a change in frequency, and the Laser Doppler Vibrometer measures this change in frequency. The vibrometer may be used to measure the velocity and the displacement of moving MEMS structures. This technique may be combined with the capacitive readout testing in order to directly measure the displacement of the beams and to correlate these displacements to the observed changes in capacitance. One issue in using Laser Doppler Vibrometry to measure MEMS devices is that the laser may cause thermal loading due to the small size and extremely low mass of the measurand [63]. However, the effect of the LDV laser should also appear in the capacitive readout output, and therefore these measurements may be directly compared.

- **Determination of photoresist spectral absorption outside the infrared**

  Near-IR spectroscopy and visible spectroscopy should be performed on ma-

terials to determine their optical sensitivity at these wavelengths and to correlate the spectral absorbance with measurements obtained from capacitive testing using various filter sets.

- **Finite element modeling of capacitive fringing fields**

  Model and optimize the ideal spacing for interdigitated cantilever fingers in order to maximize the fringing fields for capacitive readout. Compare results of finite element modeling to actual, measured capacitive output signal.

- **Determine advantages and disadvantages of using SiO_2 as the structural layer**

  Using bulk micromachining of silicon to release a structure using silicon dioxide as the structural layer should have higher mechanical sensitivity based on finite element modeling. However, the effect of changing the anchor from silicon dioxide to silicon may have unintended consequences such as decreasing thermal isolation and increasing the thermal time constant.

- **Formation of plate-like structure for high fill-factor**

  Use geometry described by Corbeil *et al.* [57] to reduce effects of temperature fluctuation noise.

- **Formation of 4x4 or 8x8 arrays**

  Develop a focal plane array to demonstrate the ability to image a scene using this technology. Single pixel remain useful for heat-seeking applications.

- **Develop CMOS-compatible process**

  Ideally, a readout-circuit would be fabricated on-chip first and the MEMS infrared device would be fabricated on top. Integration would be achieved by using interconnect to connect the cantilever array directly to the readout circuitry on chip. Fabrication of the cantilever device would need to be modified such that all processing steps take place at a temperature less than 450°C.

- **Replacement of protective photoresist**

  Wafer dicing produces particulates that can contaminate the surface of a chip. Because polymers are almost always removed at the end of semiconductor fabrication processes, unbaked photoresist is traditionally used as a protective, sacrificial coating during the wafer dicing process. Because photoresist is an integral part of the final cantilever device in the fabrication process described in Chapter 4, it would be beneficial to change the protective coating to a material other than photoresist to minimize damage to

the structural resist. Potential materials include LOL-2000 or LOL-3000, a polymer traditionally used for lift-off processes.

- **Characterize dynamics of moisture removal from chitosan**

  Because the stress in chitosan films is modified due to both thermal expansion and removal of moisture in the film, it is important to understand the dynamics of moisture removal, that is, how quickly it can occur, and how quickly moisture is absorbed back into the film. Analyzing thermal expansion in a moisture-free environment would also provide useful insight into film properties.

- **Perform stress-temperature measurements in moisture-free environment**

  To determine the effect of moisture and humidity on the stress-temperature response of chitosan films, the response in air could be compared to the response in a nitrogen-filled chamber. This would establish a clear cause-and-effect between the hysteresis seen in the stress-temperature data and the moisture in the air. While such an equipped machine is not currently available in the UC Berkeley Microlab, such equipment is available in the marketplace.

While the author makes no pretenses of explaining the mechanism of IR transduction in *Melanophila acuminata*, it seems plausible based on work described in Chapter 3 that the absorption of infrared radiation in the beetle's sense organ could release bound water from the chitin into the cavity which would increase the cavity pressure. This contribution to pressure change would likely dominate over any change in pressure of any existing sealed air due to heating by conduction or convection. The combined IR-transparency and moisture barrier properties of the wax surrounding the insect pit organ would be consistent with the IR releasing bound water from the chitin. Furthermore, release of water from the chitin lamella would change the dimensions of the film and through Poisson's ratio effect would cause a change in dimension in the transverse direction. This would result in a photo-thermal-mechanical hypothesis similar to that proffered by Hammer *et al.* and Schmitz *et al.* Consistent with their hypothesis, it is important to note the increased density of lamellated structures at the cuticular cap shown in Figure 1.4, which appears to function to maximize the pressure exerted on the cuticular cap according to the basic equation $P = \frac{F}{A}$ (maximal force operating over minimized area). This same observation is noted in the cross-section independently drawn by Evans [16]. In addition, it cannot be ruled out that a hybrid model that would involve a superposition of these effects could explain the transduction sensory mechanism of *Melanophila acuminata*.

Nomenclature

c	Speed of light
c	Heat capacity
d	Diameter of diffraction-limited Airy disk
$f_{\#}$	f-number of the optics
Δf	Frequency
h	Planck's constant
k	Boltzmann constant
k	Spring constant
k	Thermal conductivity
α	Coefficient of thermal expansion
α	Spectral absorbance
ϵ	Emissivity
λ	Wavelength
η	Viscosity
ν	Frequency
ν	Poisson ratio
ρ	Density
σ	Stefan-Boltzmann constant
Φ	Radiant flux
A	Area
CTE	Coefficient of thermal expansion
D*	Detectivity
DA	Degree of acetylation
E	Young's modulus
E	Irradiance
E_g	Bandgap
G	Thermal conductance
I	Intensity

L	Radiance
M	Molecular weight
NETD	Noise equivalent temperature difference
P	Power
P	Pressure
Q	Quality factor
Q	Radiant energy
SNR	Signal-to-noise ratio
T	Temperature
T_g	Glass transition temperature

Bibliography

[1] F. F. Sizov, "Infrared detectors: outlook and means," *Semiconductor Physics, Quantum Electronics & Optoelectronics*, vol. 3, no. 1, pp. 52–58, 2000.

[2] R. D. Hudson, *Infrared System Engineering.* John Wiley & Sons, 1969.

[3] P. L. Richards, "Bolometers for infrared and millimeter waves," *Journal of Applied Physics*, vol. 76, pp. 1–24, 1994.

[4] A. Rogalski, "Infrared detectors: status and trends," *Progress in Quantum Electronics*, vol. 27, pp. 59–210, 2003.

[5] J. Kallhammer, "The road ahead for car night-vision," *Nature Photonics*, vol. Sample issue, pp. 12–13, 2006.

[6] A. Rogalski and K. Chrzanowski, "Infrared devices and techniques," *Opto-electronics Review*, vol. 10, no. 2, pp. 111–136, 2002.

[7] B. Li, "Design and simulation of an uncooled double-cantilever microbolometer with the potential for ∼mK NETD," *Sensors and Actuators A*, vol. 112, pp. 351–359, 2004.

[8] G. R. M. Grant, "The sensory pits of insects considered as dielectric wave guides and resonators to infra-red rays," *Proceedings of the Royal Society of Queensland*, vol. 60, no. 8, pp. 89–98, 1950.

[9] H. Bleckmann, H. Schmitz, and G. von der Emde, "Nature as a model for technical sensors," *Journal of Comparative Physiology A*, vol. 190, pp. 971–981, 2004.

[10] D. X. Hammer, H. Schmitz, A. Schmitz, H. G. R. III, and A. J. Welch, "Sensitivity threshold and response characteristics of infrared detection in the beetle *Melanophila acuminata* (Coleoptera: Buprestidae," *Comparative Biochemistry and Physiology Part A*, no. 128, pp. 805–819, 2001.

[11] A. L. Campbell, R. R. Naik, L. Sowards, and M. O. Stone, "Biological infrared imaging and sensing," *Micron*, vol. 33, pp. 211–225, 2002.

[12] W. G. Evans, "Infra-red receptors in *Melanophila acuminata* DeGeer," *Nature*, no. 4928, p. 211, 1964.

[13] W. G. Evans, "Morphology of the infrared sense organs of *Melanophila acuminata* (Buprestidae: Coleoptera)," *Annals of the Entomological Society of America*, vol. 59, no. 5, pp. 873–877, 1966.

[14] D. X. Hammer, J. Seigert, M. O. Stone, H. G. R. III, and A. Welch, "Infrared spectral sensitivity of *Melanophila acuminata*," *Journal of Insect Physiology*, vol. 47, pp. 1441–1450, 2001.

[15] L. A. Sowards, H. Schmitz, D. W. Tomlin, R. R. Naik, and M. O. Stone, "Characterization of beetle *Melanophila acuminata* (Coleoptera: Buprestidae) infrared pit organs by high-performance liquid chromatogrpahy/mass spectrometry, scanning electron microscope, and Fourier transform-infrared spectroscopy," *Annals of the Entomological Society of America*, vol. 94, no. 5, pp. 686–694, 2001.

[16] W. G. Evans, "Infrared radiation sensors of *Melanophila acuminata* (Coleoptera: Buprestidae): A thermopneumatic model," *Annals of the Entomological Society of America*, vol. 98, no. 5, pp. 738–746, 2005.

[17] T. Vondran, K. H. Apel, and H. Schmitz, "The infrared receptor of *Melanophila acuminata* De Geer (Coleoptera: Buprestidae): ultrastructural study of a unique insect thermoreceptor and its possible descent from a hair mechanoreceptor," *Tissue & Cell*, vol. 27, no. 6, pp. 645–658, 1995.

[18] J. Hazel, N. Fuchigami, V. Gorbunov, H. Schmitz, M. Stone, and V. V. Tsukruk, "Ultramicrostructure and microthermomechanics of biological IR detectors: material properties from a biomimetic perspective," *Biomacromolecules*, vol. 2, pp. 304–312, 2001.

[19] D. X. Hammer, D. Dave, T. E. Milner, B. Choi, H. G. R. III, and A. J. Welch, "Investigation of the transduction mechanism of infrared detection in *Melanophila acuminata*: photo-thermal-mechanical hypothesis," *Comparative Biochemistry and Physiology Part A*, vol. 132, pp. 381–392, 2002.

[20] H. Schmitz, A. Schmitz, and H. Bleckmann, "A new type of infrared organ in the Australian "fire-beetle" *Merimna atrata* (Coleoptera: Buprestidae)," *Naturwissenschaften*, vol. 87, pp. 542–545, 2000.

[21] M. J. Madou, *Fundamentals of Microfabrication*, 2nd ed. CRC Press, 2002.

[22] M. N. V. R. Kumar, "A review of chitin and chitosan applications," *Reactive and Functional Polymers*, vol. 46, no. 1, pp. 1–27, 2000.

[23] G. F. Payne and S. R. Raghavan, "Chitosan: a soft interconnect for hierarchical assembly of nano-scale components," *Soft Matter*, vol. 3, pp. 521–527, 2007.

[24] H. Schmitz and H. Bleckmann, "The photomechanic infrared receptor for the detection of forest fires in the beetle *Melanophila acuminata* (Coleoptera: Buprestidae)," *Journal of Comparative Physiology A*, vol. 182, pp. 647–657, 1998.

[25] K. Kurita, "Controlled functionalization of the polysaccharide chitin," *Prog. Polym. Sci.*, vol. 26, pp. 1921–1971, 2001.

[26] C. A. Murray and J. R. Dutcher, "Effect of changes in relative humidity and temperature on ultrathin chitosan films," *Biomacromolecules*, vol. 7, pp. 3460–3465, 2006.

[27] L. Tan, Y. P. Kong, S. W. Pang, and A. F. Yee, "Imprinting of polymer at low temperature and pressue," *Journal of Vacuum Science and Technology B*, vol. 22, no. 5, pp. 2486–2492, 2004.

[28] P. Sorlier, C. Viton, and A. Domard, "Relation between solution properties and degree of acetylation of chitosan: role of aging," *Biomacromolecules*, vol. 3, pp. 1336–1342, 2002.

[29] H. Kam, E. Khor, and L. Lim, "Storage of partially deacetylated chitosan films," *Journal of Biomedical Materials Research*, vol. 48, no. 6, pp. 881–888, 1999.

[30] L. Wu, A. P. Gadre, H. Yi, M. J. Kastantin, G. W. Rubloff, W. E. Bentley, G. F. Payne, and R. Ghodssi, "Voltage-dependent assembly of the polysaccharide chitosan onto an electrode surface," *Langmuir*, vol. 18, pp. 8620–8625, 2002.

[31] L. Wu, H. Yi, S. Li, G. W. Rubloff, W. E. Bentley, R. Ghodssi, and G. F. Payne, "Spatially selective deposition of a reactive polysaccharide layer onto a patterned template," *Langmuir*, vol. 19, pp. 519–524, 2003.

[32] F. S. Ligler, B. M. Lingerfelt, R. P. Price, and P. E. Schoen, "Development of uniform chitosan thin-film layers on silicon chips," *Langmuir*, vol. 17, pp. 5082–5084, 2001.

[33] H. Jiang, W. Su, S. Caracci, T. J. Bunning, T. Cooper, and W. W. Adams, "Optical waveguiding and morphology of chitosan thin films," *Journal of Applied Polymer Science*, vol. 61, no. 7, pp. 1163–1171, 1996.

[34] C. L. Schauer, M. Chen, M. Chatterley, K. Eisemann, E. R. Welsh, R. R. Price, P. Schoen, and F. Ligler, "Color changes in chitosan and poly(allyl amine) films upon metal binding," *Thin Solid Films*, vol. 434, pp. 250–257, 2003.

[35] O. B. G. Assis and J. H. Hotchkiss, "Surface hydrophobic modification of chitosan thin films by hexamethyldisilazane plasma deposition: effects on

water vapour, CO_2 and O_2 permeabilities," *Packaging Technology and Science*, vol. 20, pp. 293–297, 2007.

[36] M. Lei, Y. Gu, A. Baldi, R. A. Siegel, and B. Ziaie, "High-resolution technique for fabricating environmentally sensitive hydrogel microstructures," *Langmuir*, vol. 20, no. 21, pp. 8947–8951, 2004.

[37] A. Sionkowska, H. Kaczmarek, M. Wisniewski, J. Skopinska, S. Lazare, and V. Tokarev, "The influence of UV irradiation on the surface of chitosan films," *Surface Science*, vol. 600, pp. 3775–3779, 2006.

[38] R. Fernandes, L. Wu, T. Chen, H. Yi, G. W. Rubloff, R. Ghodssi, W. E. Bentley, and G. F. Payne, "Electrochemically induced deposition of a polysaccharide hydrogel onto a patterned surface," *Langmuir*, vol. 19, pp. 4058–4062, 2003.

[39] R. N. Orth, J. Kameoka, W. R. Zipfel, B. Ilic, W. W. Webb, T. G. Clark, and H. G. Craighead, "Creating biological membranes on the micron scale: forming patterned lipid bilayers using a polymer lift-off technique," *Biophysical Journal*, vol. 85, pp. 3066–3073, 2003.

[40] Y. Dong, Y. Ruan, H. Wang, Y. Zhao, and D. Bi, "Studies on glass transition temperature of chitosan with four techniques," *Journal of Applied Polymer Science*, vol. 93, pp. 1553–1558, 2004.

[41] A. Toffey, G. Samaranayake, C. E. Frazier, and W. G. Glasser, "Chitin derivatives. I. Kinetics of the heat-induced conversion of chitosan to chitin," *Journal of Applied Polymer Science*, vol. 60, pp. 75–85, 1996.

[42] Y. Shigemasa, H. Matsuura, H. Sashiwa, and H. Saimoto, "Evaluation of different absorbance ratios from infrared spectroscopy for analyzing the degree of deacetylation in chitin," *International Journal of Biological Macromolecules*, vol. 18, pp. 237–242, 1996.

[43] J. Nunthanid, M. Laungtana-anan, P. Sriamornsak, S. Limmatvapirat, S. Puttipipatkhachorn, L. Y. Lim, and E. Khor, "Characterization of chitosan acetate as a binder for sustained release tablets," *Journal of Controlled Release*, vol. 99, pp. 15–26, 2004.

[44] H. Lorenz, M. Laudon, and P. Renaud, "Mechanical characterization of a new high-aspect-ratio near UV-photoresist," *Microelectronic Engineering*, vol. 41/42, pp. 371–374, 1998.

[45] M. C. LeMieux, M. E. McConney, Y. Lin, S. Singamaneni, H. Jiang, T. J. Bunning, and V. V. Tsukruk, "Polymeric nanolayers as actuators for ultrasensitive thermal bimorphs," *Nano Letters*, vol. 6, no. 4, pp. 730–734, 2006.

[46] J. Caniou, *Passive Infrared Detection.* Kluwer Academic, 1999.

[47] A. Mahmood, D. P. Butler, and Z. Celik-Butler, "A device-level vacuum-packaging scheme for microbolometers on rigid and flexible substrates," *IEEE Sensors Journal*, vol. 7, no. 7, pp. 1012–1019, 2007.

[48] R. G. Driggers, Ed., *Encylopedia of Optical Engineering.* Marcel Dekker, 2003, ch. Detectors - Figures of Merit, pp. 349–357.

[49] P. R. Norton, "Infrared detectors in the next millennium," *SPIE*, vol. 3698, pp. 652–665, 1999.

[50] C. Lee, C. Tsai, L. Chen, L. Fu, and Y. Chen, "Elastic-plastic modeling of heat-treated bimorph micro-cantilevers," *Microsystems Technology*, vol. 12, pp. 979–986, 2006.

[51] S. R. Hunter, R. A. Amantea, L. A. Goodman, D. B. Kharas, S. Gershtein, J. R. Matey, S. N. Perna, Y. Yu, N. Maley, and L. K. White, "High sensitivity uncooled microcantilever infrared imaging arrays," *Infrared Technology and Applications XXIX*, vol. 5074, pp. 469–480, 2003.

[52] S. R. Hunter, G. Maurer, L. Jiang, and G. Simelgor, "High sensitivity uncooled microcantilever infrared imaging arrays," *Infrared Technology and Applications XXXII*, vol. 6206, pp. 1–12, 2006.

[53] S. R. Hunter, G. S. Maurer, G. Simelgor, S. Radhakrishan, and J. Gray, "High sensitivity 25 μm and 50 μm pitch microcantilever IR imaging arrays," *Infrared Technology and Applications XXXIII*, vol. 6542, 2007.

[54] G. A. Gehring, M. D. Cooke, I. S. Gregory, W. J. Karl, and R. Watts, "Cantilever unified theory and optimization for sensors and actuators," *Smart Materials and Structures*, vol. 9, pp. 918–931, 2000.

[55] Z. Djurić, D. Randjelović, I. Jokić, J. Matović, and J. Lamovec, "A new approach to IR bimaterial detectors theory," *Infrared Physics & Technology*, vol. 50, pp. 51–57, 2007.

[56] J. Lai, T. Perazzo, Z. Shi, and A. Majumdar, "Optimization and performance of high-resolution micro-optomechanical thermal sensors," *Sensors and Actuators A*, vol. 58, pp. 113–119, 1997.

[57] J. L. Corbeil, N. V. Lavrik, S. Rajic, and P. G. Datskos, ""Self-leveling" uncooled microcantilever thermal detector," *Applied Physics Letters*, vol. 81, no. 7, pp. 1306–1308, 2002.

[58] R. Gunter, H. G. W. Harding, and W. S. Stiles, "Spectral reflexion factor of the cat's tapetum," *Nature*, vol. 168, no. 4268, pp. 293–294, 1951.

[59] Y. Zhao, "Optomechanical uncooled infrared imaging system," Ph.D. dissertation, University of California, Berkeley, Deparment of Mechanical Engineering, 2002.

[60] S. Huang and X. Zhang, "Study of gradient stress in bimaterial cantilever structures for infrared applications," *Journal of Micromechanics and Microengineering*, vol. 17, pp. 1211–1219, 2007.

[61] S. Huang, B. Li, and X. Zhang, "Elimination of stress-induced curvature in microcantilever infrared focal plane arrays," *Sensors and Actuators A*, vol. 130-131, pp. 331–339, 2006.

[62] E. Friedman and J. L. Miller, *Photonics Rules of Thumb: Optics, Electro-optics, Fiber Optics, and Lasers*, 2nd ed. McGraw Hill, 2003.

[63] P. Castellini, M. Martarelli, and E. P. Tomasini, "Laser Doppler Vibrometry: Development of advanced solutions answering to technology's needs," *Mechanical Systems and Signal Processing*, vol. 20, pp. 1265–1285, 2006.

Publishing Agreement

It is the policy of the University to encourage the distribution of all theses and dissertations. Copies of all UCSF theses and dissertations will be routed to the library via the Graduate Division. The library will make all theses and dissertations accessible to the public and will preserve these to the best of their abilities, in perpetuity.

Please sign the following statement:

I hereby grant permission to the Graduate Division of the University of California, San Francisco to release copies of my thesis or dissertation to the Campus Library to provide access and preservation, in whole or in part, in perpetuity.

Michael T Mueller 12/20/2007

Author Signature Date